Contact mechanics of adhesive beams

A Thesis Submitted
in Partial Fulfillment of the Requirements
for the Degree of
Doctor of Philosophy

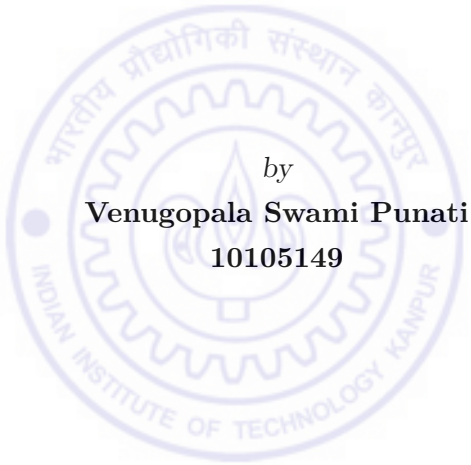

by

Venugopala Swami Punati
10105149

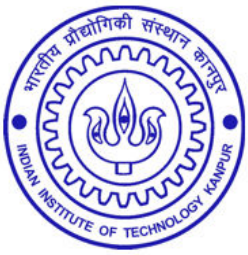

to the

Department of Mechanical Engineering
Indian Institute of Technology, Kanpur

May, 2017

Certificate

This is to certify that the work contained in the thesis entitled "***Contact mechanics of adhesive beams***", by ***Venugopala Swami Punati***, has been carried out under our supervision and that this work has not been submitted elsewhere for a degree.

May, 2017

(Dr. Ishan Sharma and Dr. Pankaj Wahi)
Department of Mechanical Engineering,
Indian Institute of Technology,
Kanpur.

ABSTRACT/SYNOPSIS

Name of Student: Venugopala Swami Punati. Roll No: 10105149.

Degree for which submitted: Ph. D. Department: Mechanical Engineering.

Thesis Title: Contact mechanics of adhesive beams.

Names of Thesis Supervisors:

1. Dr. Ishan Sharma, Department of Mechanical Engineering, IIT Kanpur.
2. Dr. Pankaj Wahi, Department of Mechanical Engineering, IIT Kanpur.

Month and year of thesis submission: May 2017.

Recent developments on adhesives are motivated by biological species, e.g. structured adhesives. Some of these adhesives incorporate beams as basic building blocks. Understanding the response of an adhesive beam to indentation tests will help in creating better adhesives. In this work, we present a formulation to study the contact of an adhesive elastic beam resting on flexible supports with a rigid cylinder. We limit ourselves to two-dimensional plane strain indentation problem. The adhesion between the beam and the punch is modeled through an adhesive zone model, that can be conveniently generalized.

The contact problem is reformulated as a boundary value problem for the unknown pressure field, the adhesive zone's size and the displacement of the beam's bottom surface. This results in two coupled Fredholm integral equations of the first kind, that are solved through Galerkin or collocation methods. When the contact area is not large, the displacement of the bottom surface may be conveniently approximated by that of an Euler-Bernoulli beam's, reducing the problem to one integral equation. However, for greater contact areas the coupled system is solved. We investigate non-adhesive indentation in great detail, comparing our results with finite element simulations and previously published results; a good match is found. Later, we study adhesive beam indentation. We employ both the JKR approximation and adhesive zone models. Finally, we compare our semi-analytical predictions with preliminary experiments and also demonstrate its application to an actual structural adhesive.

Dedicated to my teachers...

Acknowledgments

I sincerely express my gratitude towards my thesis supervisors Prof. Ishan Sharma and Prof. Pankaj Wahi for their guidance and constant support through out my programme. I would also like to thank Prof. Ishan Sharma for providing me time, like anytime walk-in office, particularly during the last two years; and for pestering me, of course this benefited me a lot, to attend conferences and providing financial support for the same. I really enjoyed auditing his courses during the academic and summer sessions, and also reading some of the literature, both academic and non-academic, that he mentioned in his classes. I also acknowledge his financial support during my last two years of stay at IIT Kanpur. I acknowledge Prof. Pankaj Wahi for giving me time, and for the short and brief discussions on thesis where ever we met, either it was in the academic area corridors or outside of it. This helped me to recollect and remember the salient features in my work. Apart from this, I am also thankful for his inputs on numerics.

I thank Dr. T. Bhuvana, Prof. P. Venkitanarayanan and Prof. S. L. Das of the Department of Mechanical Engineering, IIT Kanpur, for help with experiments. I am also grateful to Prof. Akash Anand from the Department of Mathematics and Statistics, IIT Kanpur for useful discussions.

I would like to thank Prof. Anigmanshu Ghatak, Dr. Subrata Mondal and Mr. Pravat Rajbanshi for their help while planning to prepare contact mechanics experimental set-up.

I would like to acknowledge Dr. Ravi Dalmeya, for his help right from the beginning of my Ph. D. admission process. The discussions with him on finite element modelling of contact problems (employing ABAQUS) were very much informative and helpful. I am also grateful for his help during GRC-2013 conference. I thank Dr. Ashish Bhateja for his help, particularly during the last phase of my Ph.D. and during the paper's submission to the Journals. I deeply acknowledge Dr. V. Laxminarasimharao and Mr. Abhinav R. Dehadrai for their help and support during almost my entire doctoral programme. I appreciate the informative and helpful discussions that I had with them. I also acknowledge Mr. Dehadrai for his help during ICCMS-2012, GRC-2013 and ESMC-2015 conferences. I very much appreciate the discussions that I had with Mr. Vineet Nair. I also acknowledge

him for being a constant source to give a glimpse on the recently published literature, and it was very much helpful for me in recovering the lost tracks in other subjects. I acknowledge my other lab-mates Mr. Prasad R. Sonar, Mr. Krishnan S. Iyer, Mr. Deepak Sachan and Mr. Dipayan Mukherjee for their support. Many thanks are due to Mr. Satya Prakash Mishra, Mr. Ram Lakhan and Mr. Amit Kumar for their help in developing the experimental set-up. I would also like to thank Mr. Satya Prakash Mishra for keeping the lab merchandise available all the time and even when notified at the last moment.

I deeply acknowledge Mr. Gunasekhar Burra for his help and support, either it being personal or academic, during my stay at IIT Kanpur. I appreciate his help during my travel to ESMC-2015 conference. I am very thankful for the discussions that I had with him during the initial stages of PDMS sample preparation. I also appreciate the informative discussions that I had with Mr. Narendra Reddy, Mr. Ashok Ummireddy, Mr. Srikanth Dasari and Mr. Prakash. The time that we all spent together is memorable.

I acknowledge the staff from various offices like Department of Mechanical Engineering, Dean of Students Affairs, Dean of Academic Affairs, Dean of Resources and Alumni and Dean of Research and Development of IIT Kanpur for their support during conferences and other administrative tasks.

I express my gratitude towards my mother, father and brother for their support, love and patience. I would like to thank my aunt and uncle, Mrs. Devasena Gutha and Mr. Venkateswara Rao Gutha, for their support and guidance through out my academics. I would like to acknowledge my cousins Mr. Venkata Ramana Punati, Mr. Nagasrinivasarao Katta, Mr. Ramesh Punati and my uncle Mr. Veeranarayana Punati for taking good care of my father's health in my absence. I would like to extend my gratitudes to my mother-in-law and father-in-law, Mrs. Nagaraja Kumari Athota and Mr. Sambasivarao Athota, for their kindness and support. I would also like to thank my brother-in-laws Mr. Venkata Lakshmi Narasimha Prasad Athota and Mr. Sudhakar Nimmagadda for their support in crucial moments. I cherish the moments that I spent with my daughter Sadanjanasai Gahana Punati. Her tireless and enthusiastic attempts to learn new things provoked me to think afresh and inspired me to learn further all the way. Finally, I am deeply thankful to my wife Mrs. Pravallika Bhargavi Punati for being supportive, taking good care of family and sharing several responsibilities on my behalf.

Contents

भारतीय प्रौद्योगिकी संस्थान कानपुर
INDIAN INSTITUTE OF TECHNOLOGY KANPUR

List of Tables

भारतीय प्रौद्योगिकी संस्थान कानपुर
INDIAN INSTITUTE OF TECHNOLOGY KANPUR

List of Figures

भारतीय प्रौद्योगिकी संस्थान कानपुर
INDIAN INSTITUTE OF TECHNOLOGY KANPUR

Chapter 1

Basic contact mechanics theories

In this work, we investigate indentation by a rigid cylindrical punch of an adhesive beam. This work is motivated by ongoing research and development of structural adhesives, many of which incorporate adhesive beams as a core structural element.

In this chapter, we start with a discussion on non-adhesive contact of spheres, often called as Hertzian contact. Later we explain the famous Johnson-Kendall-Roberts (JKR) and Derjaguin-Muller-Toporov (DMT) approximate theories for the adhesive contact of spheres. We then discuss the adhesive zone model proposed by Maugis (1992), which resolved the long standing conflict between the JKR and DMT theories. At the end of this chapter, we provide an outline for the rest of the thesis.

1.1 Non-adhesive ('Hertzian') contact

In 1881, Hertz investigated the indentation of two spheres as shown in Fig. 1.1. The spheres are considered to be elastic and smooth. Adhesion was not considered in the problem.

As shown in Fig. 1.1, the two elastic spheres, with Young's modulus E_1 and E_2, Poisson's ratios ν_1 and ν_2, radii R_1 and R_2, and surface profiles $f_1(r)$ and $f_2(r)$, where $r^2 = x^2 + y^2$, are pressed against each other by a force P. Under the action of this load, the spheres make contact over a circle of radius a and the spheres' centres move a distance δ – called total indentation depth – towards each other. The indentation depths in the spheres are δ_1 and δ_2 and the vertical displacements of the interacting surfaces ($z = 0$) are $\bar{u}_{z_1}$ and

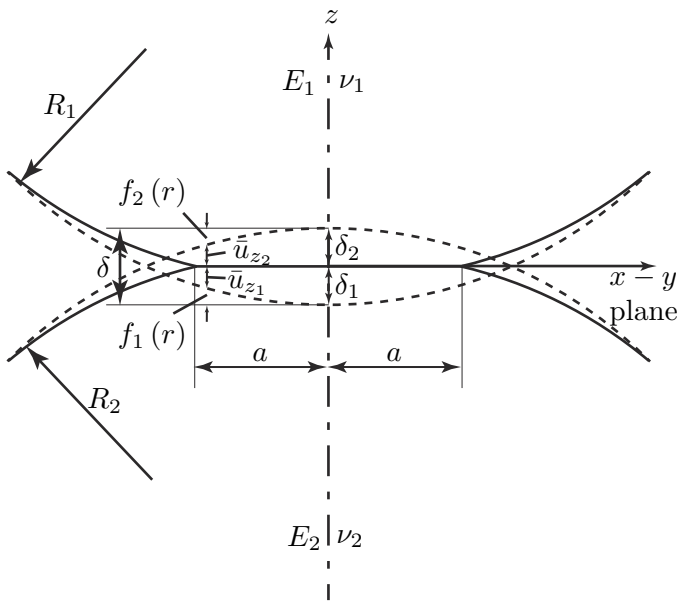

Figure 1.1: Indentation of two non-adhesive spheres. This figure is adapted from Johnson (1985, p. 88).

$\bar{u}_{z_2}$, as shown in Fig. 1.1. In this configuration, a pressure $p(r)$ acts on each sphere within the contact region. It is also assumed that R_1 and R_2 are much large compared to a and δ. Thus, the surface profiles $f_1(r)$ and $f_2(r)$ may, respectively, be approximated by $r^2/2R_1$ and $r^2/2R_2$. Then, employing the theory of elasticity, Hertz obtained the relationship between the contact parameters, i.e. a, δ, P and $p(r)$. In this section, we derive these relationships following Johnson (1985) for completeness.

From Fig. 1.1, we may write the total vertical displacement in the contact region as

$$\bar{u}_{z_1}(r) + \bar{u}_{z_2}(r) = \delta_1 - f_1(r) + \delta_2 - f_2(r) = \delta - \frac{r^2}{2R_c}, \tag{1.1}$$

where

$$\delta = \delta_1 + \delta_2 \quad \text{and} \quad \frac{1}{R_c} = \frac{1}{R_1} + \frac{1}{R_2}. \tag{1.2}$$

Next, because $\delta << R$, each sphere is approximated as an elastic half-space, each of which has a pressure $p(r)$ acting on its surface within the contact region. The vertical displacements $\bar{u}_{z_1}$ and $\bar{u}_{z_2}$ due to the pressure $p(r)$ acting on the bodies may then be found using Boussinesq's solution for a point load acting on the three dimensional elastic half-space surface. Boussinesq solved the problem of a point load acting on the surface

of a three dimensional elastic half-space, whose Young's modulus and Poisson's ratio are E and ν, respectively; see e.g. Johnson (1985, p. 52). The vertical displacement of the surface in Boussinesq's problem is

$$\bar{u}_z^p = \frac{2\,(1-\nu)\,P}{4\pi r G} = \frac{P}{\pi r E^*}, \tag{1.3}$$

where $E^* = E/(1-\nu^2)$.

The axi-symmetric load distribution $p(r)$ acting over a circle of radius a is now expressed as the superposition of infinitely many concentrated point loads. The displacement at any point on the surface of a sphere can then be written in terms of Boussinesq's solution (1.3) through a convolution integral.

First, consider points inside the contact region. For this we choose a point B$(r,0)$ inside the circle of radius a as shown in Fig. 1.2(a). The displacement at this point due to a load element $p\,(t)\,sds\,d\phi$ at the point C(s,ϕ) is $p\,(t)\,ds\,d\phi/\pi E^*$, when the coordinates (s,ϕ) are with respect to point 'B'. Integrating over s and ϕ leads to

$$\bar{u}_z\,(r) = \frac{1}{\pi E^*}\int_0^{2\pi}\int_0^{s_1} p\,(t)\,ds\,d\phi \quad \text{for } r \le a, \tag{1.4}$$

with

$$a^2 - t^2 = \alpha^2 - 2\beta s - s^2, \tag{1.5}$$

where

$$\alpha^2 = a^2 - r^2, \quad \beta = \cos\phi \tag{1.6}$$

and s_1 is the positive solution of $\alpha^2 - 2\beta s - s^2 = 0$. Evaluating the above integral we may obtain vertical displacement of the surface at points in the interior of the contact region.

Similarly, from Fig. 1.2(b), the vertical displacement of the surface for the points outside the contact region is given by

$$\bar{u}_z\,(r) = \frac{1}{\pi E^*}\int_{-\phi_1}^{\phi_1}\int_{s_1}^{s_2} p\,(t)\,ds\,d\phi \quad \text{for } r > a, \tag{1.7}$$

with

$$a^2 - t^2 = \alpha^2 + 2\beta s - s^2, \tag{1.8}$$

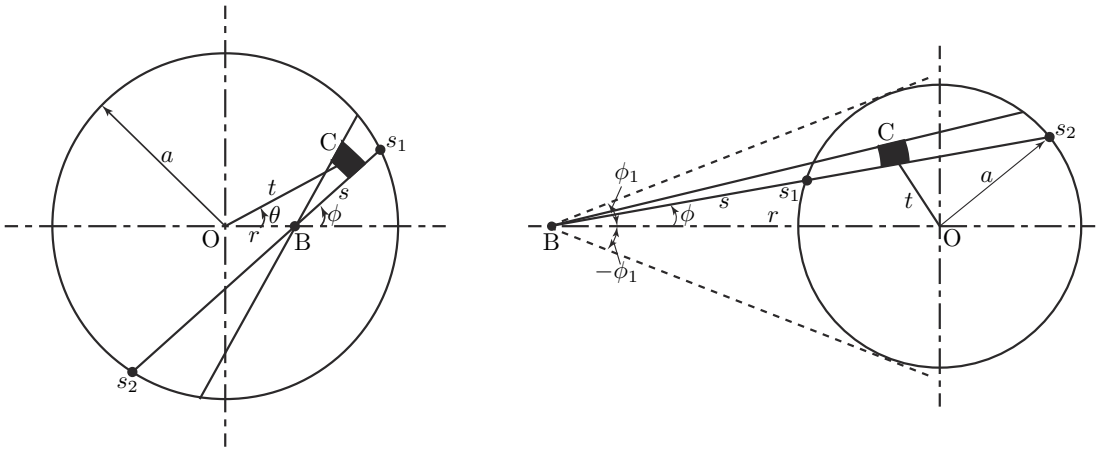

(a) (b)

Figure 1.2: The circular contact region of radius a found during the indentation of two non-adhesive elastic spheres. The displacements (a) inside and (b) outside the contact patch at the point 'B' located at $(r, 0)$ with respect to the center of contact patch 'O', are found. For this we select an element of size $s\,ds\,d\phi$, where the pressure $p(t)$ is acting, at the point 'C' whose coordinates are (s, ϕ) when measured from point 'B'. This figure is adapted from Johnson (1985, p. 57).

$s_{1,2}$ being the two roots of $\alpha^2 + 2\beta s - s^2 = 0$ and $\phi_1 = \sin^{-1}(a/r)$.

Finding $\bar{u}_{z_1}(r)$ and $\bar{u}_{z_2}(r)$ employing (1.4) to spheres 1 and 2 (approximated as half-spaces), and substituting them in (1.1), for points inside the contact region we obtain

$$\delta - \frac{r^2}{2R_c} = \frac{1}{\pi E_c^*} \int_0^{2\pi} \int_0^{s_1} p(t)\, ds\, d\phi \quad \text{for } r \le a, \tag{1.9}$$

where

$$\frac{1}{E_c^*} = \frac{1-\nu_1^2}{E_1} + \frac{1-\nu_2^2}{E_2}. \tag{1.10}$$

We note that for a rigid punch indenting an elastic half-space we set $E_c^* = E^*$ and $R_c = R$ in the above equations. Hence, we continue our subsequent calculations with E^* and R.

Following Johnson (1985), the general pressure distribution that satisfies (1.9) is given by

$$p(r) = p_0 \left(1 - \frac{r^2}{a^2}\right)^{1/2} + p_0' \left(1 - \frac{r^2}{a^2}\right)^{-1/2}, \tag{1.11}$$

where p_0 and p_0' are constants that will now be determined. When $p_0' \neq 0$, the contact pressure $p(r)$ is singular at the contact edges, i.e. at $r = a$. Negative p_0' leads to negative tractions, i.e. tensile forces, at the contact edges, which indicates the presence of adhesive

forces between the spheres. Because Hertz did not consider adhesion between the spheres, p_0' can*not* be negative. A positive p_0' makes the surfaces interact outside of the contact area. In Hertzian contact, departing surfaces do not interact outside the contact area – the two surfaces depart tangentially from the outer edges of the contact – hence, p_0' cannot be positive. Therefore, in Hertzian contact p_0' should be zero. This reduces the contact pressure distribution $p(r)$ in (1.11) to

$$p(r) = p_0 \left(1 - \frac{r^2}{a^2}\right)^{1/2}. \tag{1.12}$$

Employing the above *Hertzian* pressure distribution in (1.9) and evaluating the integral, we obtain the relationships for a and δ in terms of p_0:

$$a = \frac{\pi p_0 R}{2E^*} \quad \text{and} \quad \delta = \frac{\pi a p_0}{2E^*}. \tag{1.13}$$

Finding the total load acting on the bodies by integrating the normal traction $p(r)$, given by (1.12) yields

$$P = \int_0^a 2\pi r p(r)\, dr = \frac{2}{3} p_0 \pi a^2. \tag{1.14}$$

Using (1.14), we may find p_0 in terms of P as

$$p_0 = \frac{3P}{2\pi a^2}. \tag{1.15}$$

Finally, employing (1.15), the relationships (1.13) may be expressed as

$$a^3 = \frac{PR}{K} \quad \text{and} \quad \delta = \frac{a^2}{R}. \tag{1.16}$$

Thus, knowledge of any one of a, δ or P allows the computation of the other two.

In this work we will consider contact in two dimensions. Hence, we indicate how the above process is adapted to the case of contact of two cylinders. When cylinders are pressed against each other they make contact along their longitudinal axis. Then we follow the above procedure with few modifications. These modifications are: (a) First, we replace the Boussinesq's solution with Flamant's solution for a point load acting on two-dimensional elastic half-space (Johnson, 1985, p. 14-17). (b) Then, we integrate the

Flamant's solution over the contact area, which is a line contact of length $2a$ in two-dimensional indentation. Finally, we obtain the relationships for the contact area a and the contact pressure distribution $p(x)$ under the action of the total load P as

$$a^2 = \frac{16}{3}\frac{PR}{\pi K} \quad \text{and} \quad p(x) = p_0 \left(1 - \frac{x^2}{a^2}\right)^{1/2}, \tag{1.17}$$

with $p_0 = 2P/\pi a$; see (Johnson, 1985, p. 99-101). We note that, for two-dimensional Hertzian contact, we can*not* obtain the relationship for the punch displacement δ explicitly, as the far-field displacements are infinity in two-dimensional half-spaces.

1.2 Adhesive contact: JKR approximation

When adhesion is present between the spheres the relationships between a, δ, P and $p(r)$ obtained in Sec. 1.1 are *not* valid any more. We now derive the appropriate relationships.

The effect of adhesion between the elastic spheres was first studied by Derjaguin (1934). To this end, Derjaguin proposed an energy approach. The effect of adhesive forces outside the contact area was ignored. However, the solutions obtained in this paper were found to be unsatisfactory.

Later, the problem of adhesive spheres indentation was studied by Johnson et al. (1971) through an energy approach, similar to the one used in Derjaguin (1934). The former solution is now called the JKR approximation. We follow Johnson (1985) to outline their derivation. For this, we assume two elastic spheres as in Sec. 1.1, with adhesion present between them. When these adhesive spheres are pressed against each other by a force P, they make a contact over a circle of radius a, the spheres' centres move a distance δ towards each other and a pressure $p(r)$ acts on each of these spheres within the contact region, which is now different from what was found in Sec. 1.1; see Fig. 1.3. From our discussion in Sec. 1.1, the vertical displacement of the surfaces in the contact region $r \leq a$ may be written as

$$\delta - \frac{r^2}{2R} = \frac{1}{\pi E^*} \int_0^{2\pi} \int_0^{s_1} p(t)\, ds\, d\phi \quad \text{for } r \leq a. \tag{1.18}$$

It is reminded that we again employ E^* and R for E_c^* and R_c, respectively, in the above

equation. The pressure distribution $p(r)$ satisfying the above equation is

$$p(r) = p_0 \left(1 - \frac{r^2}{a^2}\right)^{1/2} + p_0' \left(1 - \frac{r^2}{a^2}\right)^{-1/2}, \tag{1.19}$$

where p_0 and p_0' are constants that need to be determined. In adhesionless Hertzian contact we argued that p_0' has to be zero. However, in the presence of adhesion, adhesive forces act between the interacting surfaces, so that p_0' may be allowed to be *negative*. We now proceed to find p_0 and p_0'.

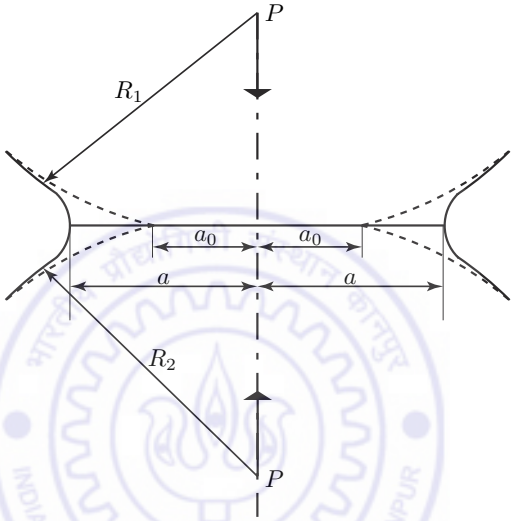

Figure 1.3: Schematic for the indentation of two adhesive elastic spheres. The contact area with $p_0' = 0$, i.e. in the absence of adhesion is indicated by a_0. This figure is adapted from Johnson et al. (1971).

In Johnson et al. (1971) the adhesive contact between spheres is broken up into two steps. First, the contact area a is achieved without adhesion between the spheres. This is represented by the curve O-A in Fig. 1.4. For this curve $p_0' = 0$ and the contact pressure is represented by only the first part of (1.19). Then, by keeping the contact area *constant* at a, the adhesion between the spheres is turned on, which in Fig. 1.4, is represented by the curve A-B. This is equivalent to unloading a flat-ended cylinder of radius a, such that the final load becomes P and the approach between the spheres' centers become δ. The contact pressure during this is given by the second part of (1.19); see Johnson (1958).

From our discussion on Hertzian contact, for curve O-A, we already know that

$$p_0 = 2aE^*/\pi R \quad \text{and} \quad \delta_0 = \frac{\pi a p_0}{2E^*}. \tag{1.20}$$

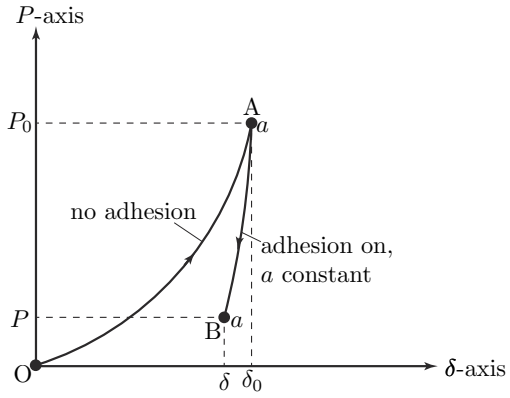

Figure 1.4: A schematic showing how the adhesion is introduced in the JKR approximation. This figure is adapted from Johnson et al. (1971).

We now find the flat-ended cylindrical punch displacement for the curve A-B. From Johnson (1985, p. 60), the total displacement (approach of the indenters) in the contact region due to $p_0' \left(1 - r^2/a^2\right)^{-1/2}$ is

$$\delta_0' = \frac{\pi a p_0'}{E^*}. \tag{1.21}$$

Employing (1.20b) and (1.21), we obtain the indentation depth δ due to the axi-symmetric pressure distribution (1.19) to be

$$\delta = \delta_0 + \delta_0' = \frac{\pi a}{2E^*}\left(p_0 + 2p_0'\right). \tag{1.22}$$

The total load required to generate the axi-symmetric $p(r)$ given by (1.19) is

$$P = \int_0^a p\left(r\right) 2\pi r \, dr \, d\theta = \pi a^2 \left(\frac{2}{3}p_0 + 2p_0'\right). \tag{1.23}$$

The elastic energy stored in the spheres due to the pressure distribution (1.19) is

$$\tilde{U}_E = \frac{1}{2}\int_0^{2\pi}\int_0^a p\left(r\right) \, r \, dr \, d\theta \, \bar{u}_z\left(r\right), \tag{1.24}$$

where $\bar{u}_z\left(r\right) = \delta - r^2/2R$. Evaluating the above integral:

$$\tilde{U}_E = \frac{\pi^2 a^3}{E^*}\left(\frac{2}{15}p_0^2 + \frac{2}{3}p_0 p_0' + {p_0'}^2\right). \tag{1.25}$$

If a constant load P acts on the punch while achieving the contact area a and punch

displacement δ, then the amount of work done is

$$\tilde{U}_W = P\delta, \tag{1.26}$$

where δ and P are, respectively, given by (1.22) and (1.23). If contact area a is achieved by keeping δ constant, i.e. fixed grips, then $\tilde{U}_W = 0$.

The surfaces of the spheres lose surface energy $\tilde{U}_S$ while making contact over a circle of radius a, which is given by

$$\tilde{U}_S = -w\pi a^2, \tag{1.27}$$

where w is the surface energy per unit area.

The total energy $\tilde{U}_T$, employing (1.25) and (1.27), is

$$\tilde{U}_T = \tilde{U}_E - \tilde{U}_W + \tilde{U}_S. \tag{1.28}$$

At equilibrium, the variation of the total energy $\tilde{U}_T$ with the contact radius a should vanish (Kanninen and Popelar, 1985, p. 158). This should be true if the total deflection of the two bodies δ is kept constant or whether the load acting on the punch P is held constant. Thus, we have

$$\left.\frac{\partial \tilde{U}_T}{\partial a}\right|_\delta = \left.\frac{\partial \tilde{U}_E}{\partial a}\right|_\delta + \left.\frac{\partial \tilde{U}_S}{\partial a}\right|_\delta = 0 \tag{1.29}$$

or

$$\left.\frac{\partial \tilde{U}_T}{\partial a}\right|_P = \left.\frac{\partial \tilde{U}_E}{\partial a}\right|_P - \left.\frac{\partial \tilde{U}_W}{\partial a}\right|_P + \left.\frac{\partial \tilde{U}_S}{\partial a}\right|_P = 0, \tag{1.30}$$

corresponding to experiments carried out with load and displacement control, respectively.

The partial derivatives in (1.29) may be obtained from (1.25) and (1.27) as, respectively,

$$\left.\frac{\partial \tilde{U}_E}{\partial a}\right|_\delta = \frac{\pi^2 a^2}{E^*} p_0'^2 \quad \text{and} \quad \left.\frac{\partial \tilde{U}_S}{\partial a}\right|_\delta = -2\pi a w. \tag{1.31}$$

Now finding the partial derivatives in (1.30) from (1.25), (1.26) and (1.27) yields, respectively,

$$\left.\frac{\partial \tilde{U}_E}{\partial a}\right|_P = \frac{\pi^2 a^2}{E^*}\left(-\frac{2}{3}p_0 p_0' - p_0'^2\right), \quad \left.\frac{\partial \tilde{U}_M}{\partial a}\right|_P = \frac{\pi^2 a^2}{E^*}\left(-\frac{2}{3}p_0 p_0' - 2p_0'^2\right)$$
$$\text{and} \quad \left.\frac{\partial \tilde{U}_S}{\partial a}\right|_P = -2\pi a w. \tag{1.32}$$

Combining (1.29) and (1.31), or (1.30) and (1.32) yields

$$p_0' = \pm\sqrt{\frac{2wE^*}{\pi a}}. \tag{1.33}$$

From our previous discussion in this section, p_0' has to be negative, so that

$$p_0' = -\sqrt{\frac{2wE^*}{\pi a}}. \tag{1.34}$$

Replacing p_0 and p_0' in (1.22) and (1.23) from, respectively, (1.20)(a) and (1.34), produces the punch displacement and the load acting on the punch in JKR approximation:

$$\delta = \frac{a^2}{R} - \sqrt{\frac{8\pi a w}{3K}} \tag{1.35}$$

and

$$P = \frac{a^3 K}{R} - \sqrt{6\pi w K a^3}. \tag{1.36}$$

Now rearranging (1.36) yields

$$\left(P - \frac{a^3 K}{R}\right)^2 = 6\pi w K a^3. \tag{1.37}$$

Solving the above equation for a^3 we obtain the contact area

$$a^3 = \frac{R}{K}\left(P + 3w\pi R \pm \sqrt{6w\pi RP + (3w\pi R)^2}\right). \tag{1.38}$$

The variation of a with P given by the above equation is shown in Fig. 1.5. In Fig. 1.5, curve B-C represents (1.38) with the positive sign, while the curve O-B is for the negative sign. However, we can*not* trace the curve O-B from experiments, as the contact is lost if we try to unload the spheres below the point 'B'. Thus, we consider only positive sign in

(1.38), i.e.

$$a^3 = \frac{R}{K}\left(P + 3w\pi R + \sqrt{6w\pi RP + (3w\pi R)^2}\right). \tag{1.39}$$

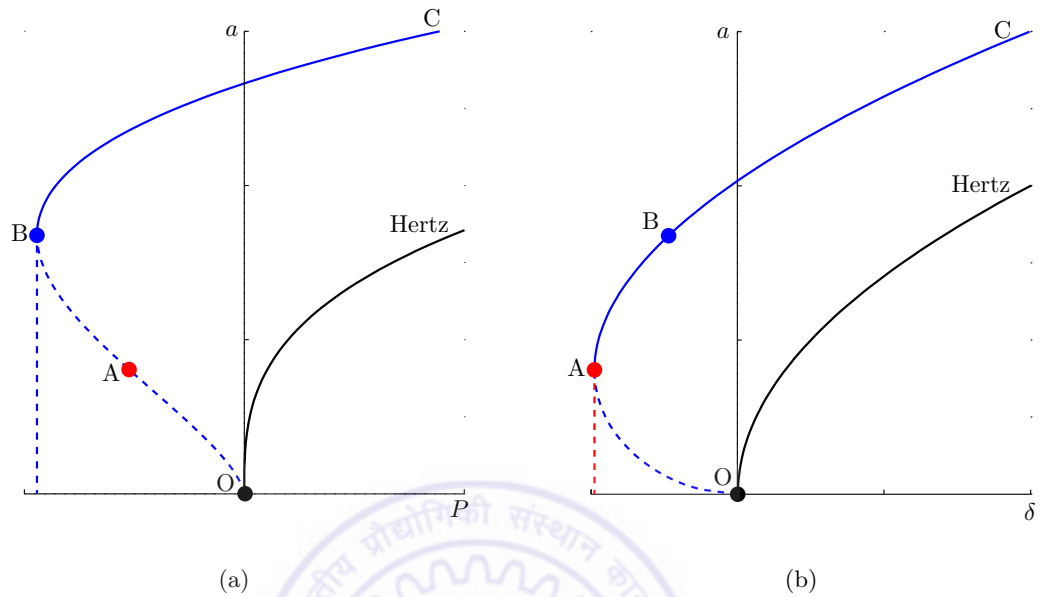

Figure 1.5: Variation of contact area a with (a) total load P and (b) punch's displacement δ is shown for JKR and Hertz approximations. Figure. (a) is adapted from Johnson (1985, p. 128).

The above relationship may also be obtained by alternative approaches of Maugis (1992); cf. Sec. 1.4.

Setting the surface energy $w = 0$ in (1.39) reduces it to the Hertzian relationship (1.16a). From (1.39), we find that when there is no load acting on the spheres, i.e. $P = 0$, they may still be in contact over a circle of radius

$$a^3 = \frac{R}{K}\left(6w\pi R\right), \tag{1.40}$$

which is caused by adhesion. Thus, in order for contact to be lost we have to apply negative (tensile) loads. At these negative loads, for a to be real, we should have

$$6w\pi RP \leq \left(3w\pi R\right)^2, \tag{1.41}$$

in (1.39). Rearranging, we obtain

$$P \geq -\frac{3}{2}w\pi R, \tag{1.42}$$

so that the minimum tensile load that can be applied without loss of contact is

$$P_c = -\frac{3}{2} w\pi R. \tag{1.43}$$

Note that this load is independent of the elastic modulus. At this load the contact radius is given by

$$a_c = \left(\frac{3}{2}\frac{\pi w R^2}{K}\right)^{1/3}. \tag{1.44}$$

The quantities P_c and a_c locate the point 'B' in Fig. 1.5. Applying more tensile loads than P_c will lead to an abrupt loss in contact. Hence, P_c represents the pull-off load. We may also obtain P_c and a_c by setting $dP/da = 0$, where the load P is given by (1.36). Thus, P_c and a_c represent the pull-off load and the corresponding contact area in an experiment where the load is controlled.

The pull-off load and the corresponding contact area in δ controlled experiment are given by $d\delta/da = 0$, where δ is employed from (1.35); see Fig. 1.5(b). The pull-off load and the corresponding contact area in experiments with displacement control are

$$P_c^\delta = -\frac{5}{6}\pi w R \quad \text{and} \quad a_c^\delta = \left(\frac{\pi w R^2}{6K}\right)^{1/3}. \tag{1.45}$$

In Fig. 1.5, P_c^δ and a_c^δ represent the point 'A'. We can*not* trace the curve O-A from either load or displacement controlled experiments, as we lose contact at point 'B' (load controlled test) or point 'A'(displacement controlled test).

1.3 Adhesive contact: DMT approximation

The axi-symmetric adhesive contact between two bodies was also investigated by Derjaguin et al. (1975) building upon Derjaguin (1934). They chose to study the contact between a rigid plane and an adhesive elastic sphere with Young's modulus E, Poisson's ratio ν and radius R; see Fig. 1.6. This so-called DMT theory/approximation may be generalized to the case of two adhesive spheres indentation by redefining $1/R$ and $1/E^*$ as, respectively,

$$\frac{1}{R_c} = \frac{1}{R_1} + \frac{1}{R_2} \quad \text{and} \quad \frac{1}{E_c^*} = \frac{1}{E_1^*} + \frac{1}{E_2^*},$$

where

$$E_1^* = \frac{E_1}{1-\nu_1^2} \quad \text{and} \quad E_2^* = \frac{E_2}{1-\nu_2^2},$$

with E_i and ν_i, i $(i = 1, 2)$, representing the Young's modulus and the Poission's ratio of the sphere's material, respectively.

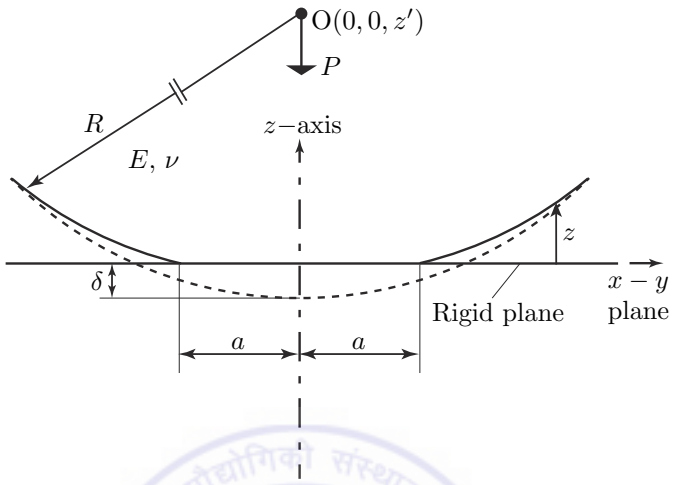

Figure 1.6: The indentation of an adhesive elastic sphere with a rigid plane as approximated by the DMT theory. This figure is adapted from Derjaguin et al. (1975).

In DMT approximation, it is assumed that the contact pressure within the contact region remains Hertzian and is given by (1.12). Hence, the pressure distribution $p(r)$ within the contact region and the indentation depth δ are, respectively,

$$p(r) = \frac{3P}{2\pi a^2}\left(1 - \frac{r^2}{a^2}\right)^{1/2} \quad \text{and} \quad \delta = \frac{a^2}{R} = \frac{3P}{4aE^*}. \tag{1.46}$$

From our discussion on the Hertzian contact in Sec. 1.1, we may find the vertical displacement at a point on the sphere, that lies outside the contact region, employing (1.7). Doing so, and employing (1.46b), we obtain

$$\bar{u}_z(r) = \frac{1}{2\pi R}\left\{2a\sqrt{(r^2-a^2)} + \left(2a^2 - r^2\right)\cos^{-1}\left(1 - \frac{2a^2}{r^2}\right)\right\} \quad \text{for } r > a; \tag{1.47}$$

see also Johnson (1985, p. 61). Because we are considering the contact of Fig. 1.6, we use $\bar{u}_z$ to denote surface displacement of the sphere, which is distinct from $\bar{u}_z$ in (1.1).

The distance between the spherical and the flat surfaces is then

$$z = \frac{r^2}{2R} + \bar{u}_z(r) - \delta. \tag{1.48}$$

Employing (1.46b) and (1.47) in (1.48) yields

$$z = \frac{1}{\pi R}\left[a\sqrt{(r^2-a^2)} - \left(2a^2-r^2\right)\tan^{-1}\left\{\left(\frac{r^2}{a^2}-1\right)^{1/2}\right\}\right] \quad \text{for } r \geq a. \tag{1.49}$$

The microscopic distance between two contacting surfaces can never be zero (Derjaguin et al., 1975). Thus, we rewrite (1.49) as

$$H = \frac{1}{\pi R}\left[a\sqrt{(r^2-a^2)} - \left(2a^2-r^2\right)\tan^{-1}\left\{\left(\frac{r^2}{a^2}-1\right)^{1/2}\right\}\right] + \epsilon \quad \text{for } r \geq a, \tag{1.50}$$

where ϵ is the microscopic distance between the bodies inside the contact area.

Now we proceed to find various energies that are associated with adhesive contact. The elastic energy W_e stored in the sphere due to the contact pressure $p(r)$ is given by

$$W_e = \int_0^{\delta} F_e(\delta)\, d\delta, \tag{1.51}$$

where, from Hertzian theory, we write the force required to produce the deflection δ in the spherical particle is

$$F_e = k\delta^{3/2} = \frac{4E^*\sqrt{R}}{3}\delta^{3/2} = K\sqrt{R}\delta^{3/2}. \tag{1.52}$$

In DMT theory, surface interactions are modeled through an interaction potential $\varphi(H)$. The surface energy due to the potential $\varphi(H)$ acting between the sphere and the flat surface is

$$W_s = \int_0^{L} \varphi(H)\, 2\pi r dr, \tag{1.53}$$

where $L = H_{max}$ is the maximum air-gap between the contacting surfaces. The interaction potential $\varphi(H)$ decreases rapidly with an increase in H as shown in Fig. 1.7. Thus, the upper limit of the integration in (1.53) may conveniently be taken to be infinity. Re-writing (1.53):

$$W_s = \int_0^{\infty} \varphi(H)\, 2\pi r dr = \int_0^{a} \varphi(H)\, 2\pi r dr + \int_a^{\infty} \varphi(H)\, 2\pi r dr = W_s' + W_s'', \tag{1.54}$$

where W_s' and W_s'' represent the surface energies from the contact ($r \leq a$) and non-contact

$(r \geq a)$ regions, respectively.

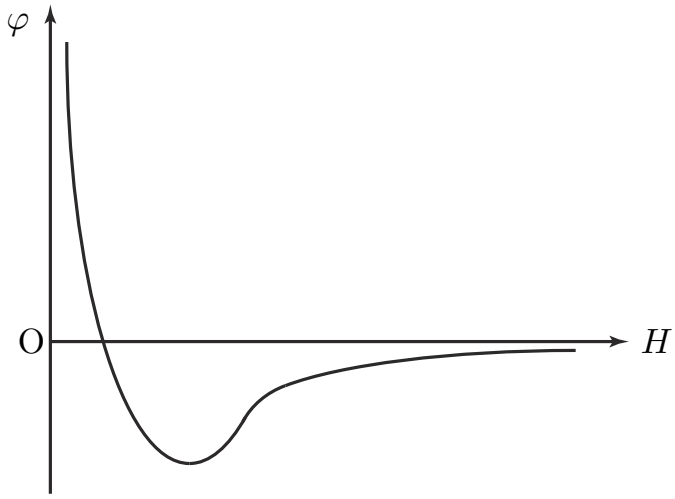

Figure 1.7: A sample interaction potential $\varphi(H)$ with the variation in H.

Once the total surface energy W_s is known, we may find the total adhesive force F_s by differentiating W_s:

$$F_s = -\frac{dW_s}{dz'}, \tag{1.55}$$

where z' is the position of the sphere's center:

$$z' = R + \epsilon - \delta, \quad \text{so that} \quad dz' = -d\delta. \tag{1.56}$$

Combining (1.55) and (1.56), we find the adhesive force

$$F_s = \frac{dW_s}{d\delta}. \tag{1.57}$$

We now proceed to find the surface energy contribution from the contact and non-contact regions. From there the corresponding adhesive force components F_s' and F_s'' will then be found through the formula

$$F_s \quad = \quad \frac{dW_s}{d\delta} = \frac{dW_s'}{d\delta} + \frac{dW_s''}{d\delta} = F_s' + F_s''. \tag{1.58}$$

We first find the surface energy W_s' from the contact region using the fact that within the

contact region $H = \epsilon$. Thus,

$$W_s' = \int_0^a \varphi(\epsilon)\, 2\pi r dr = \pi a^2 \varphi(\epsilon). \tag{1.59}$$

Employing (1.46b), the above equation may be rewritten as

$$W_s' = \pi \delta R \varphi(\epsilon). \tag{1.60}$$

The adhesive force component is then

$$F_s' = \frac{dW_s'}{d\delta} = \pi R \varphi(\epsilon), \tag{1.61}$$

which contributes to the total adhesion force F_s. We observe that F_s' is independent of δ and a.

Next, we find the surface energy component W_s'' and the corresponding adhesive force component F_s'' contributed by the non-contact zone, i.e. $r \geq a$. The surface energy in the non-contact zone is

$$W_s'' = \int_a^\infty \varphi\left[H(r,\delta)\right] 2\pi r\, dr. \tag{1.62}$$

Employing the change of variables $r^2 - a^2 = x^2$, we rewrite (1.62) as

$$W_s'' = 2\pi \int_0^\infty \varphi\left[H(x,\delta)\right] x\, dx, \tag{1.63}$$

where

$$H(x,\delta) = \frac{1}{\pi R}\left\{ax + \left(x^2 - a^2\right)\tan^{-1}\left(\frac{x}{a}\right)\right\} + \epsilon. \tag{1.64}$$

Evaluating F_s'' from (1.58), we obtain

$$F_s'' = \frac{dW_s''}{d\delta} = 2\pi \int_0^\infty \varphi'\left[H(x,\delta)\right] \frac{dH(x,\delta)}{d\delta} x\, dx. \tag{1.65}$$

Because we have not assumed a specific form for the interaction potential $\varphi'(H)$, we can*not* evaluate the above integral. However, we know that $\varphi(H \to \infty) \to 0$ and $\varphi(H \to 0) \to \varphi(\epsilon)$. So, we may obtain limiting value of the integral in (1.65) when contact is lost and the deformation in the spherical particle vanishes. For this, we have to first evaluate $dH/d\delta$

employing (1.64), which yields

$$\frac{d}{d\delta}H\left(x,\delta\right)=\frac{dH}{da}\,\frac{da}{d\delta}=\frac{1}{\pi}\left\{\frac{ax}{x^2+a^2}-\tan^{-1}\left(\frac{x}{a}\right)\right\} \tag{1.66}$$

During unloading, as the deformation in the spherical particle disappears we are going to have a point contact, i.e. $\delta\to 0$ and $a\to 0$. In the limit $\delta\to 0$, (1.64) and (1.66) become, respectively,

$$H|_{\delta\to 0}=\frac{x^2}{2R}+\epsilon,\quad \text{so that}\quad x\,dx=R\,dH, \tag{1.67}$$

and

$$\left.\frac{dH}{d\delta}\right|_{\delta\to 0}=-\frac{1}{2}. \tag{1.68}$$

Evaluating F_s'' after substituting (1.67) and (1.68) in (1.65) provides

$$\begin{aligned}F_s''\left(\delta=0\right) &= 2\pi\int_{\epsilon}^{\infty}\varphi'\left(H\right)\frac{-1}{2}\,R\,dH=-\pi R\,\varphi\left(H\right)|_{\epsilon}^{\infty}\\ &= \pi R\varphi\left(\epsilon\right).\end{aligned} \tag{1.69}$$

Finally, substituting (1.61) and (1.69) in (1.58) yields the total adhesive force

$$F_s=\pi R\varphi\left(\epsilon\right)+\pi R\varphi\left(\epsilon\right)=2\pi R\varphi\left(\epsilon\right). \tag{1.70}$$

When the adhesive sphere does not make a contact with the flat rigid surface, the distance between them is given by

$$H=\frac{r^2}{2R}+H_0, \tag{1.71}$$

where H_0 is the gap between the flat surface and the lowest point of the adhesive sphere; see Fig. 1.8.

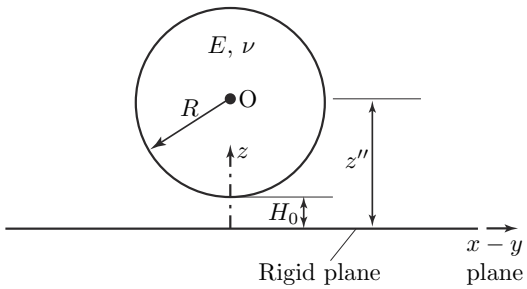

Figure 1.8: An adhesive elastic sphere and a rigid plane when not in contact. This figure is adapted from Derjaguin et al. (1975).

Differentiating (1.71) yields

$$r\,dr = R\,dH. \tag{1.72}$$

Finding the surface energy W_s from (1.53) and (1.72) provides

$$W_s\left(H_0\right) = 2\pi R \int_{H_0}^{\infty} \varphi\left(H\right) dH. \tag{1.73}$$

In the configuration of Fig. 1.8, the position of the spherical particle's center is given by

$$z'' = H_0 + R, \quad \text{so that} \quad dx'' = dH_0. \tag{1.74}$$

Finding the total adhesive force utilizing (1.55) and (1.74) provides

$$F_s = -\frac{dW_s}{dH_0}\Big|_{H_0=\epsilon}. \tag{1.75}$$

Finally, evaluating adhesion force employing (1.73) and (1.75) yields

$$F_s\left(\epsilon\right) = 2\pi R\varphi\left(\epsilon\right). \tag{1.76}$$

From (1.70) and (1.76), respectively, we may conclude that an adhesion force of $2\pi R\varphi\left(\epsilon\right)$ acts between the spherical particle and the flat surface if there is a point contact or just before contact.

To find the total adhesive force during indentation, we assume a specific form for the surface interaction potential. Following Derjaguin et al. (1975), the interaction potential may be considered as

$$\varphi\left(H\right) = \frac{A}{12\pi H^2}, \tag{1.77}$$

where the Hamaker constant A measures the attractive van der Waals forces strength between two surfaces (Maugis, 2000, p.15), is found from

$$\frac{AR}{6\epsilon^2} = 2\pi R\varphi\left(\epsilon\right) = F_0, \tag{1.78}$$

where F_0 is force required to break the contact when the sphere and plane are separated by a distance ϵ.

From (1.58) we already know that the total adhesive force may be found by adding the contributions from the contact and the non-contact regions. From (1.70) we note that F_s' is independent of δ and a, while F_s'' varies with δ as per (1.65). We now compute the total adhesive force F_s.

Employing (1.78) in (1.70) yields

$$F_s' = \frac{F_0}{2}. \tag{1.79}$$

To compute F_s'' we evaluate φ' employing (1.64), (1.77) and (1.78) to find

$$\varphi'(x,a) = -\frac{F_0\epsilon^2}{\pi R\left[\frac{1}{\pi R}\left\{ax + (x^2-a^2)\tan^{-1}\left(\frac{x}{a}\right)\right\} + \epsilon\right]^3}. \tag{1.80}$$

Combining (1.66) and (1.80) with (1.65) provides

$$F_s'' = \frac{2}{\pi}F_0\int_0^\infty \frac{\epsilon^2\left\{\tan^{-1}(x/a) - (ax/x^2+a^2)\right\}}{R\left[(1/\pi R)\left\{ax + (x^2-a^2)\tan^{-1}(x/a)\right\} + \epsilon\right]^3} x\,dx. \tag{1.81}$$

Before proceeding to the evaluation of the integral in (1.81), we set

$$\beta = \frac{\delta}{\epsilon} = \frac{a^2}{R\epsilon} \quad \text{and} \quad \xi = \frac{x}{\sqrt{R\epsilon}}. \tag{1.82}$$

Introducing the above in (1.81), we obtain

$$F_s'' = \frac{2}{\pi}F_0\int_0^\infty \frac{\left\{\tan^{-1}\left(\xi/\sqrt{\beta}\right) - \xi\sqrt{\beta}/\left(\xi^2+\beta\right)\right\}}{\left[(1/\pi)\left\{\xi\sqrt{\beta} + (\xi^2-\beta)\tan^{-1}\left(\xi/\sqrt{\beta}\right)\right\} + 1\right]^3}\xi\,d\xi. \tag{1.83}$$

Finding the total adhesive force employing (1.58), (1.79) and (1.83) yields

$$\frac{F_s}{F_0} = \frac{1}{2} + \frac{2}{\pi}\int_0^\infty \frac{\left\{\tan^{-1}\left(\xi/\sqrt{\beta}\right) - \xi\sqrt{\beta}/\left(\xi^2+\beta\right)\right\}}{\left[(1/\pi)\left\{\xi\sqrt{\beta} + (\xi^2-\beta)\tan^{-1}\left(\xi/\sqrt{\beta}\right)\right\} + 1\right]^3}\xi\,d\xi. \tag{1.84}$$

It is difficult to evaluate the above integral in closed form. However, we may find the asymptotic behavior of the integral at small and large δ. This may be done by expanding the integrand in (1.84) in a series in terms of $\sqrt{\beta}$ and $1/\sqrt{\beta}$, respectively. The integral in (1.84) is then found by integrating the series termwise.

For small δ, we expand the integrand in (1.84) in a Taylor series about small $\sqrt{\beta} = \sqrt{\delta/\epsilon}$

:

$$\frac{F_s}{F_0} \approx \frac{1}{2} + \frac{2}{\pi}\int_0^\infty \left\{ \frac{4\pi\xi}{\left(\xi^2+2\right)^3} - \frac{16}{\left(\xi^2+2\right)^3}\sqrt{\beta} + \frac{12\pi\xi}{\left(\xi^2+4\right)^4}\beta + \cdots \right\} d\xi. \tag{1.85}$$

Integrating the above termwise, we obtain

$$\frac{F_s}{F_0} \approx \frac{1}{2} + \frac{2}{\pi}\left(\frac{\pi}{4} - \frac{3\pi\sqrt{2}}{8}\sqrt{\beta} + \frac{\pi}{4}\beta + \cdots \right), \tag{1.86}$$

which may be simplified and written in terms of δ as

$$\frac{F_s}{F_0} \approx 1 - \frac{3\sqrt{2}}{4}\sqrt{\frac{\delta}{\epsilon}} + \frac{1}{2}\frac{\delta}{\epsilon} + \cdots. \tag{1.87}$$

From (1.87) we observe that, as δ vanishes, the adhesive force F_s becomes $F_0 = 2\pi R\varphi(\epsilon)$, which confirms the result obtained in (1.70).

At large deformations, i.e. $\delta \gg \epsilon$, expanding the integrand in (1.84) in terms of $1/\sqrt{\beta} = \sqrt{\epsilon/\delta}$, we obtain

$$\frac{F_s}{F_0} \approx \frac{1}{2} + \frac{4}{3\pi\sqrt{\beta^3}}\int_0^\infty \frac{\xi^4}{\left\{\left(4\xi^3/3\pi\sqrt{\beta}\right)+1\right\}^3}\, d\xi + \cdots. \tag{1.88}$$

Employing the change of variables

$$t = \xi\left(4/3\pi\sqrt{\beta}\right)^{1/3}, \tag{1.89}$$

(1.88) becomes

$$\frac{F_s}{F_0} \approx \frac{1}{2} + \frac{4}{3\pi\sqrt{\beta^3}}\left(\frac{3\pi\sqrt{\beta}}{4}\right)^{5/3}\int_0^\infty \frac{t^4}{\left(t^3+1\right)^3}\, dt + \cdots. \tag{1.90}$$

With the change of variables $t = (\tan\theta)^{2/3}$, the above may be integrated and written in terms of δ as

$$\frac{F_s}{F_0} \approx \frac{1}{2} + \frac{\pi^2}{9\sqrt{3}\sqrt[3]{6\pi}}\left(\frac{\epsilon}{\delta}\right)^{2/3} + \cdots. \tag{1.91}$$

From (1.91), we see that the adhesive force decreases with increase in indentation depth. At large indentations $F_s = F_0/2 = \pi R\varphi(\epsilon)$. This result is true for any interaction potential φ; for details see Derjaguin et al. (1975).

Finally, the total load P acting on the punch is obtained by adding F_e and F_s:

$$P = F_e + F_s. \tag{1.92}$$

In DMT theory, from (1.87), the contact between the adhesive sphere and the rigid plane is broken when we apply a tensile load of magnitude $2\pi R\varphi(\epsilon)$ on the punch.

1.4 Adhesive contact: Adhesive zone model

From Secs. 1.2 and 1.3, we see that the predictions of JKR (Johnson et al., 1971)) and DMT (Derjaguin et al., 1975) theories are at odds with each other. The main differences between the two theories are shown in Table. 1.1.

JKR theory	**DMT theroy**
(i) Both compressive and tensile stresses are allowed inside the contact region. Singularities in the contact pressure at the contact edges are permissible.	(i) This theory assumes that the stresses in the contact region are compressive only, and the contact pressure profile remains Hertzian.
(ii) No stresses act between the interacting surfaces outside the contact region.	(ii) DMT theory considers the stresses acting between the interacting bodies outside the contact region. The nature of these stresses are tensile.
(iii) From (i) and (ii), we may observe that the stress distribution is discontinuous at the contact edges: as $r \to a^-, \sigma_y \to -\infty$, and as $r \to a^+, \sigma_y \to 0$.	(iii) From (i) and (ii), we see that there is a discontinuity in the stress distribution at the contact edges: as $r \to a^-, \sigma_y \to 0$, and as $r \to a^+, \sigma_y \to -\sigma_0$.

JKR theory	DMT theroy
(iv) In JKR theory, it is assumed that the adhesive forces are strong and, hence, cause deformations in the elastic bodies. This deformation may deviates significantly from Hertzian theory. The deformations caused by adhesive forces play an important role in neck formations, i.e. tangents to the contacting surfaces are vertical, at the contact edges; see Fig. 1.3.	(iv) DMT theory assumes that the adhesive forces are small and, hence, do not cause any deformations in the elastic bodies. Therefore, the deformation in the elastic bodies are only due to stresses in the contact region, and the deformations in the elastic bodies are as given by Hertzian theory. Thus, DMT theory does not allow neck formations at the contact edges.

Table 1.1: Differences betwen JKR and DMT theories

To resolve the percieved discrepancy between JKR and DMT theories, Tabor (1977) proposed that these two theories are the two extreme limits of one general theory. Maugis (1992) proved this hypothesis. He employed an adhesive zone, similar to cohesive zone in fracture mechanics, to account for adhesion outside the contact region. Employing the strength of adhesion as a parameter, Maugis showed that both JKR and DMT theories are contained within one general theory. In this section we discuss Maugis (1992) approach to adhesive contact in detail.

Maugis (1992) considered the axi-symmetric frictionless indentation by a rigid spherical punch of an adhesive elastic half-space. The problem was posed within the framework of fracture mechanics.

We first recall that Sneddon (1965) considered the frictionless indentation by a axi-symmetric rigid punch, whose profile is given by $f(x)$, where $x = r/a$, with an elastic half-space whose Young's modulus and Poisson's ratio are E and ν, respectively. Sneddon obtained the relationships for the indentation depth (or punch displacement) δ, load P acting on the punch, normal traction on the surface $\sigma_y(r, o)$ within the contact zone, i.e. $r \leq a$, and vertical displacement of the surface $u_y(r, o)$ outside the contact zone, i.e. $r \geq a$,

as, respectively,

$$\delta = \int_0^1 \frac{f'(x)}{\sqrt{1-x^2}}\,dx + \frac{\pi}{2}\,\chi(1)\,, \tag{1.93}$$

$$P = \frac{3\pi aK}{4}\int_0^1 \chi(t)\;dt = \frac{3\pi aK}{2}\left(\delta - \int_0^1 \frac{x f(x)}{\sqrt{1-x^2}}\,dx\right), \tag{1.94}$$

$$\sigma_y(r,0) = -\frac{3K}{8a}\left(\frac{\chi(1)}{\sqrt{1-r^2/a^2}} - \int_{r/a}^1 \frac{\chi'(t)}{\sqrt{t^2-r^2/a^2}}\,dt\right) \quad \text{for } r<a, \tag{1.95}$$

and $$u_y(r,0) = \int_0^1 \frac{\chi(t)}{\sqrt{r^2/a^2-t^2}}\,dt \quad \text{for } r>a, \tag{1.96}$$

where

$$\chi(t) = \frac{2}{\pi}\left(\delta - t\int_0^t \frac{f'(x)}{\sqrt{t^2-x^2}}\,dx\right), \tag{1.97}$$

with $K = 4E/3\,(1-\nu^2)$. We observe from (1.95) that the contact pressure is singular at the contact edge $r = a$, unless $\chi(1) = 0$. Thus, when the surface profiles of the interacting surfaces are smooth, we do *not* expect a stress singularity and we set $\chi(1) = 0$ in (1.93)–(1.96), to recover the results for axi-symmetric, non-adhesive indentation. On the other hand, Maugis (1992) showed that allowing $\chi(1) \neq 0$ helps in providing results for adhesive, axi-symmetric indentation, as well as for those indentations where the indenter is not smooth, so that σ_y may be singular at $r = a$.

Employing (1.96), we may find the distance between the elastic half-space and the rigid spherical punch as

$$[u_y] = f\left(\frac{r}{a}\right) - \delta + u_y(r,0)\,; \tag{1.98}$$

see Fig. 1.9.

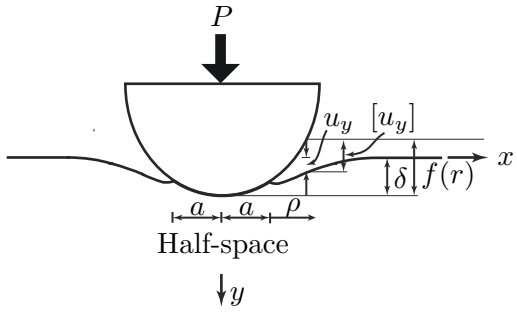

Figure 1.9: The indentation of a rigid spherical punch with an adhesive elastic half-space.

We now represent the stresses in the contact region and the distance between the surfaces in terms of the stress intensity factor K_1 defined by

$$K_1 = -\frac{3K}{8}\chi(1)\sqrt{\frac{\pi}{a}}. \tag{1.99}$$

We shift the coordinate system to the contact edge, and introduce ρ as a measure of distance from the contact edge. Employing (1.95) and (1.98), we may represent the normal surface traction $\sigma_y(r,0)$ inside the contact region, and the distance $[u_y]$ between the contacting surfaces as, respectively,

$$\sigma_y(a-\rho,0) \approx \frac{K_1}{\sqrt{2\pi\rho}}, \tag{1.100}$$

$$\text{and} \quad [u_y](a-\rho,0) \approx \frac{4(1-\nu^2)}{E}K_1\sqrt{\frac{\rho}{2\pi}}. \tag{1.101}$$

The above are analogous to the expressions for crack tip stresses and the crack opening displacement, respectively, in plane strain problems (Kanninen and Popelar, 1985, p. 163). This suggests that we may employ concepts from fracture mechanics to analyse contact problems. We begin by finding the energy release rate – variation of elastic energy with a keeping δ constant. As the stresses at the contact edges can be singular, the energy release rate; see (Kanninen and Popelar, 1985, p. 163),

$$G = \frac{1}{2}\frac{1-\nu^2}{E}K_1^2. \tag{1.102}$$

In (1.102) the factor '1/2' enters as we assume the punch to be rigid, so that frictionless indentation by a rigid punch with an elastic half-space is analogous to half of the Mode-I crack (Kanninen and Popelar, 1985, p. 139).

At equilibrium the Griffith's criterion must hold:

$$G = w, \tag{1.103}$$

which reflects the balance between the elastic energy that is provided and the surface energy lost (gain) to increase (decrease) the contact by da.

For the stable equilibrium (contact is *not* lost suddenly), we should have $\partial G/\partial a > 0$, i.e. load increases with the increase in contact area. However, the load, contact radius and

displacement at this stable equilibrium are different for experiments done at fixed load P from those performed with fixed grips (fixed displacement δ).

Employing the above relationships we now obtain results for few simple cases. For this, we first consider the axi-symmetric indentation of a flat-ended cylindrical rigid punch. We will recover all relationships given by Boussinesq; see Todhunter and Pearson (1893, p. 255). Then we proceed to the axi-symmetric indentation of a rigid spherical punch.

1.4.1 Flat punch

For the flat ended cylindrical punch, the profile of the indenting surface is given by

$$f(x) = 0. \tag{1.104}$$

Substituting the above into (1.93) and (1.97) yields

$$\chi(1) = \chi(t) = \frac{2\delta}{\pi}, \tag{1.105}$$

Employing the above in (1.94)–(1.96) and rearranging terms, we obtain, respectively,

$$\delta = \frac{2P}{3aK}, \tag{1.106}$$

$$\sigma_y(r,0) = -\frac{P}{2\pi a^2}\frac{1}{\sqrt{1-r^2/a^2}} \quad \text{for } r < a, \tag{1.107}$$

and

$$u_y(r,0) = \frac{1-\nu^2}{\pi E}\frac{P}{a}\sin^{-1}\left(\frac{a}{r}\right) \quad \text{for } r > a. \tag{1.108}$$

The above equations were first given by Boussinesq; see Todhunter and Pearson (1893, p. 255). Note that for this case $\chi(1)$ is not zero, as the surface profile of the flat ended cylindrical punch is not smooth; there is a kink in the surface displacement at the contact edge.

Now assume that there is adhesion between the punch and the half-space. Finding the stress intensity factor K_1 employing (1.99), (1.105) and (1.106) we obtain

$$K_1 = -\frac{P}{2\pi a}\sqrt{\frac{\pi}{a}}. \tag{1.109}$$

Computing the energy release rate G from (1.102) yields

$$G = \frac{P^2}{6\pi a^3 K} = \frac{3K\delta^2}{8\pi a}. \tag{1.110}$$

Finally, at equilibrium we invoke Griffith's criterion (1.103) with the first part of the above G, to find the pull-off load to be

$$P_{min} = -\sqrt{6\pi a^3 K w}. \tag{1.111}$$

The negative sign in (1.111) indicates the tensile loads and applying more tensile loads than P_{min} leads to the rupture of the contact. The above relationship was given by Kendall (1971). However, the above equilibrium is always unstable, i.e. contact is lost suddenly, whether the experiment is done at fixed load or at fixed grips.

1.4.2 Spherical punch: Hertzian and JKR contacts

During indentation by a rigid spherical punch with an elastic half-space we write the surface profile as

$$f(x) = \frac{a^2}{2R}x^2, \tag{1.112}$$

where $x = r/a$. Substituting the above into (1.97), we obtain

$$\chi(t) = \frac{2}{\pi}\left(\delta - \frac{a^2}{R}t^2\right), \tag{1.113}$$

and

$$\chi(1) = \frac{2}{\pi}\left(\delta - \frac{a^2}{R}\right). \tag{1.114}$$

- *Non-adhesive (Hertzian) indentation*

In this case the normal stresses σ_y on the surface can not be singular, as the interacting surfaces are smooth. For this $\chi(1)$ must vanish, so that (1.114) yields

$$\delta = \frac{a^2}{R}. \tag{1.115}$$

We now find the total load P, the contact pressure $\sigma_y(r,0)$ and the vertical displacement $u_y(r,0)$ of the surface outside the contact region from, respectively, (1.94), (1.95) and

(1.96):

$$P = \frac{a^3 K}{R}, \tag{1.116}$$

$$\sigma_y(r,0) = -\frac{3}{2}\frac{P}{\pi a^2}\sqrt{1-\frac{r^2}{a^2}} \quad \text{for } r < a, \tag{1.117}$$

and
$$u_y(r,0) = \frac{a^2}{\pi R}\left[\sqrt{\frac{r^2}{a^2}-1} + \left(2-\frac{r^2}{a^2}\right)\sin^{-1}\left(\frac{a}{r}\right)\right] \quad \text{for } r > a, \tag{1.118}$$

These agree with Hertz's (1881) results; see also Sec. 1.1.

Finally, substituting (1.115) and (1.118) into (1.98), we obtain the distance between the surfaces outside the contact zone from (1.98) as

$$[u_y] = \frac{a^2}{\pi R}\sqrt{\frac{r^2}{a^2}-1} + \frac{r^2-2a^2}{\pi R}\cos^{-1}\left(\frac{a}{r}\right) \quad \text{for } r > a. \tag{1.119}$$

- *Adhesive indentation: JKR approximation*

In the JKR approximation, singularities in the contact pressure at the contact edges are allowed. Thus, $\chi(1) \neq 0$, and from (1.94), (1.95) and (1.96) we obtain, respectively,

$$\delta = \frac{a^2}{3R} + \frac{2P}{3aK}, \tag{1.120}$$

$$\sigma_y(r,0) = \frac{K_1}{\sqrt{\pi a}}\frac{1}{\sqrt{1-\frac{r^2}{a^2}}} - \frac{3aK}{2\pi R}\sqrt{1-\frac{r^2}{a^2}} \quad \text{for } r < a, \tag{1.121}$$

and
$$u_y(r,0) = -\frac{2(1-\nu^2)}{\pi E}K_1\sqrt{\pi a}\sin^{-1}\left(\frac{a}{r}\right) + \frac{a^2}{\pi R}\left[\sqrt{\frac{r^2}{a^2}-1} + \left(2-\frac{r^2}{a^2}\right)\sin^{-1}\left(\frac{a}{r}\right)\right] \quad \text{for } r > a; \tag{1.122}$$

in the above, the stress intensity factor K_1 is found from (1.99) and (1.114):

$$K_1 = -\frac{3K}{4\sqrt{\pi a}}\left(\delta - \frac{a^2}{R}\right). \tag{1.123}$$

Employing (1.120), we may also write the above as

$$K_1 = -\frac{1}{2a\sqrt{\pi a}}\left(P - \frac{a^3 K}{R}\right). \tag{1.124}$$

We now calculate the energy release rate G from (1.102) employing (1.123) or (1.124):

$$G = \frac{3K}{8\pi a}\left(\delta - \frac{a^2}{R}\right)^2 = \frac{1}{6\pi a^3 K}\left(\frac{a^3 K}{R} - P\right)^2. \tag{1.125}$$

Combining (1.125) with Griffith's criterion (1.103), we obtain

$$\delta = \frac{a^2}{R} - \left(\frac{8\pi w a}{3K}\right)^{1/2}. \tag{1.126}$$

$$\text{and} \quad \frac{a^3 K}{R} = P + 3\pi w R + \sqrt{6\pi w R P + (3\pi w R)^2} \tag{1.127}$$

The above relationships match with the results of Johnson et al. (1971); see also Sec. 1.2.

From (1.127), we obtain the radius of the contact area at zero load, i.e. $P = 0$ as

$$a_0^3 = \frac{6\pi w R^2}{K}. \tag{1.128}$$

There is an abrupt loss of contact when

$$\frac{\partial G}{\partial a} = 0. \tag{1.129}$$

Substituting (1.125) into (1.129) and keeping the load P fixed we obtain

$$\left(\frac{\partial G}{\partial a}\right)_P = \frac{1}{2\pi a^4 K}\left\{\left(\frac{a^3 K}{R}\right)^2 - P^2\right\} = 0. \tag{1.130}$$

Solving the above we find the minimum load at which contact separation happens abruptly:

$$P_{min} = -\frac{3}{2}\pi w R. \tag{1.131}$$

The contact radius and the punch displacement at this load are obtained from (1.127) and (1.126):

$$a = \left(\frac{3}{2}\frac{\pi w R^2}{K}\right)^{1/3} = 0.63 a_0 \tag{1.132}$$

$$\text{and} \quad \delta = -\frac{a^2}{3R} = -\left(\frac{\pi^2 w^2 R}{12K^2}\right)^{1/3}. \tag{1.133}$$

Repeating the above process for finding the instability point when the grips are kept fixed

gives

$$\left(\frac{\partial G}{\partial a}\right)_{\delta} = \frac{3K}{8\pi R^2 a^2}\left(a^2 - \delta R\right)\left(3a^2 + \delta R\right) = 0, \tag{1.134}$$

so that the minimum depth of penetration at which the punch jumps out of contact is

$$\delta_{min} \;=\; -\frac{3a^2}{R} = -\left(\frac{3}{4}\frac{\pi^2 w^2 R}{K^2}\right)^{1/3}. \tag{1.135}$$

At this δ_{min}, the contact radius and the load are, respectively, from (1.126) and (1.127):

$$a = \left(\frac{\pi w R^2}{6K}\right)^{1/3} = 0.30 a_0 \tag{1.136}$$

and

$$P_{min} = -5P_1 = -\frac{5}{6}\pi w R. \tag{1.137}$$

Thus, we see that the load at which the contact separation happens is quite different for load controlled experiments compared to displacement control. This should be kept in mind while analyzing or performing experiments.

Finally, to find the vertical distance between the surfaces of the sphere and half-space outside the contact region, we employ (1.120) and (1.122) in (1.98):

$$[u_y] = \frac{2\left(1-\nu^2\right)}{\pi E} K_1 \sqrt{\pi a}\cos^{-1}\left(\frac{a}{r}\right) + \frac{a^2}{\pi R}\sqrt{\frac{r^2}{a^2} - 1} + \frac{r^2 - 2a^2}{\pi R}\cos^{-1}\left(\frac{a}{r}\right). \tag{1.138}$$

1.4.3 Adhesive indentation: DMT approximation

The detailed description of the DMT approximation for an adhesive contact is done in Sec. 1.3. Here, we revisit few important aspects of this theory, which will be useful in our later discussions.

In DMT theory, an attractive force acts between the interacting surfaces due to adhesion. The magnitude of this force, just before contact, and at point contact is $2\pi w R$. This force decreases as the contact area increases. Contrary to this, Pashley (1984) showed that this force increases with increase in the contact area. However, we assume that this force remains constant at $2\pi w R$, and write from (1.92) that

$$\frac{a^3 K}{R} = P + 2\pi w R. \tag{1.139}$$

The above relationship provides the correct estimation of the pull-out forces and the contact area at zero load (Muller et al., 1983). Employing (1.103) we obtain the energy release rate G from (1.139) as

$$G = \frac{1}{2\pi R}\left(\frac{a^3 K}{R} - P\right). \tag{1.140}$$

Finally, we recall from Sec. 1.3 that the contact stress distribution and the surface deformations in DMT theory remain the same as in Hertzian theory.

1.4.4 Adhesive indentation: adhesive zone modeling

We now proceed to investigate adhesive contact within the framework of adhesive zone models. In this, an adhesive zone is introduced outside the contact region within which adhesive forces act between the interacting surfaces. These forces are modeled by the Dugdale-Barenblatt model – a constant tensile traction σ_0 acting over the adhesive zone; see the inset of Fig. 1.10.

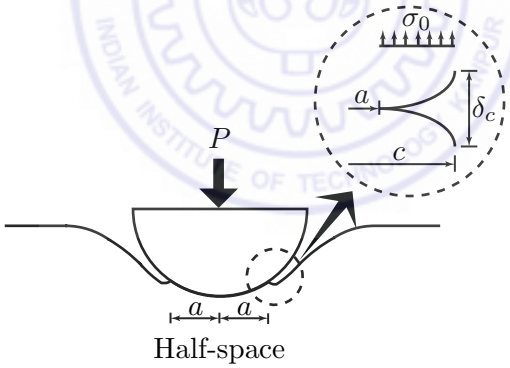

Figure 1.10: The indentation of a rigid spherical punch with an adhesive elastic half-space. The adhesive zone along with active adhesive forces is shown in the inset.

We obtain the solutions for the adhesive-zone model shown in Fig. 1.10 by combining the JKR solution – the *inner* problem – with the solution of the elasticity problem associated with the adhesive zone – the *outer* problem. The JKR results are already known. To find the tractions on the surface of the half-space and its displacement due to the action of the adhesive zone, we first consider the solutions for an external crack under pressure. This solution will be combined with that of an unloading flat punch to yield the solution to the outer problem.

- *External crack under pressure*

The loading due to an adhesive zone with the Dugdale-Barenblatt model representing the adhesive forces within the the adhesive zone may be considered as a problem of an external crack in which a constant tensile pressure σ_0 acts on the crack faces between $r = a$ and $r = c$; see Fig. 1.11.

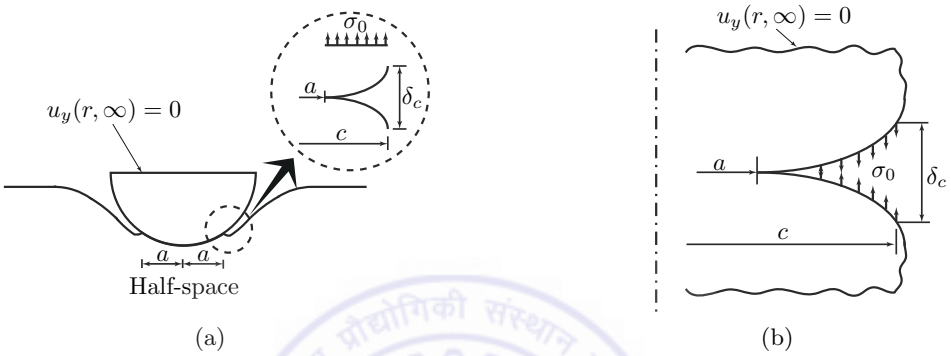

Figure 1.11: (a) An adhesive zone is introduced into the contact problem. A constatnt stress $-\sigma_0$ acts between $r = c$ and $r = a$. The displacement of the punch at faraway loactions is zero. (b) An external crack with a constant stress $-\sigma_0$ acts between $r = c$ and $r = a$.

Lowengrub and Sneddon (1965) found the normal stress distribution inside the body and the vertical displacements of the crack faces for an external crack in which an axi-symmetric pressure distribution $p(r)$ is acting on the crack faces between $r = a$ and $r = c$, with $c > a$. These normal stress distribution inside the body and the crack faces displacement are given by, respectively,

$$\sigma_y(r,0) = \frac{2}{\pi}\left[\frac{g(a)}{\sqrt{a^2-r^2}} + \int_a^\infty \frac{g'(t)}{\sqrt{t^2-r^2}}\,dt\right] \quad \text{for } r < a \tag{1.141}$$

and

$$u_y(r,0) = \frac{4(1-\nu^2)}{\pi E}\int_a^r \frac{g(t)}{\sqrt{r^2-t^2}}\,dt \quad \text{for } r > a, \tag{1.142}$$

with

$$g(t) = \int_t^\infty \frac{sp(s)}{\sqrt{s^2-t^2}}\,ds. \tag{1.143}$$

We note that in the analysis of Lowengrub and Sneddon (1965) the far-field displacements are implicitly assumed to be zero.

In the case of the adhesive zone we set $p(r) = -\sigma_0$ in (1.143) to compute

$$g(t) \quad = \quad -\sigma_0\sqrt{c^2 - t^2} \quad \text{for } t \leq c, \tag{1.144}$$

and $g(t) = 0$ for $t \geq c$. Evaluating $g'(t)$ and $g(a)$ yields

$$g'(t) = \frac{-\sigma_0\, t}{\sqrt{c^2 - t^2}}, \tag{1.145}$$

and

$$g(a) = -\sigma_0\sqrt{c^2 - a^2}. \tag{1.146}$$

Substituting (1.144) – (1.146) in (1.141) and (1.142) yields the normal surface stresses inside the contact region and the displacements outside the contact region as, respectively,

$$\sigma_y(r,0) = \frac{-2\sigma_0}{\pi}\left[\frac{\sqrt{c^2 - a^2}}{\sqrt{a^2 - r^2}} - \tan^{-1}\frac{\sqrt{c^2 - a^2}}{\sqrt{a^2 - r^2}}\right] \quad \text{for } r < a, \tag{1.147}$$

and

$$u_y(r,0) = -\frac{4(1-\nu^2)}{\pi E}\left\{\frac{\sigma_0}{a}\sqrt{c^2 - a^2}\sqrt{r^2 - a^2} - \sigma_0 c^2 \int_a^{\min(r,c)} \frac{\sqrt{r^2 - t^2}}{t^2\sqrt{c^2 - t^2}}\, dt\right\} \quad \text{for } r > a. \tag{1.148}$$

It is to be noted that the constant stresses acting in the adhesive zone deforms the surface profiles of the elastic bodies outside the contact region. However, inherent in the solution of Lowengrub and Sneddon (1965) is the assumption that the displacement at infinity is zero, which, in the case of indentation by a rigid punch, becomes equivalent to the requirement

$$\delta = 0. \tag{1.149}$$

The load required to produce the stress distribution (1.147) is

$$P_{ext} = \int_0^a \sigma_y\, 2\pi r dr = -\sigma_0\pi\left(c^2 - a^2\right) + 2\sigma_0 a^2\left[\frac{c^2}{a^2}\cos^{-1}\left(\frac{a}{c}\right) - \sqrt{\frac{c^2}{a^2} - 1}\right], \tag{1.150}$$

where the first term is due to the adhesive forces acting in the adhesive zone. The application of constant pressure $-\sigma_0$ in the adhesive zone lying between $r = a$ and $r = c$ should produce a total load equal to $-\sigma_0\pi(c^2 - a^2)$. The extra (second) term in (1.150) is due to the assumption (1.149) that the displacement of the punch is zero. For this we

need to impose at infinity a *compressive* load

$$P' = 2\sigma_0 a^2 \left[\frac{c^2}{a^2} \cos^{-1}\left(\frac{a}{c}\right) - \sqrt{\frac{c^2}{a^2} - 1} \right] > 0. \tag{1.151}$$

- *Unloading of flat punch*

The solution to the above problem correspond to a system where the displacement δ at infinity was maintained at zero by the application of the compressive load P'. We, on the other hand, are interested in the solution to the outer problem where the load on the punch at infinity vanishes. This is achieved by applying a *tensile* load P' on the punch, while keeping the contact radius at a, as shown in Fig. 1.12.

The configuration shown in Fig. 1.12 is much like a flat punch pulling away from the surface that is in contact with it. Hence, we may find the solutions of this problem employing the solutions available for flat punch indentation in Sec. 1.4.1. We now present the results for the configuration shown in Fig. 1.12.

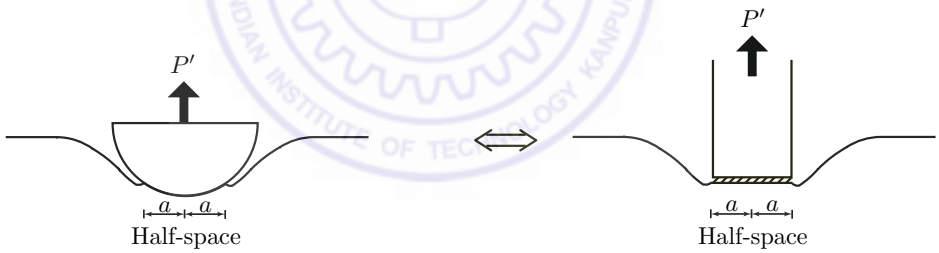

(a) (b)

Figure 1.12: (a) Unloading of the spherical punch while keeping the contact radius at a (left). The problem is solved by appealing to the solutions for the analogous problem of the unloading of a flat cylindrical punch (right).

Finding the normal stresses in the contact region and the displacements outside the contact area, respectively, from (1.107) and (1.108) yields

$$\sigma_y(r,0) = \frac{P'}{2\pi a} \frac{1}{\sqrt{a^2 - r^2}} \quad \text{for } r < a \tag{1.152}$$

and

$$u_b(r,0) = -\frac{(1-\nu^2)}{\pi E} \frac{P'}{a} \sin^{-1}\left(\frac{a}{r}\right) \quad \text{for } r > a, \tag{1.153}$$

respectively. Evaluating the displacement of the punch δ_b from (1.106), we obtain

$$\delta_b = -\frac{(1-\nu^2)}{\pi E}\frac{P'}{a}\frac{\pi}{2}. \tag{1.154}$$

Finally, shifting the origin to the contact edge and employing (1.153) and (1.154), we have

$$u_b'(r,0) = \delta_b - u_b = -\frac{(1-\nu^2)}{\pi E}\frac{P'}{a}\cos^{-1}\left(\frac{a}{r}\right) \quad \text{for } r > a, \tag{1.155}$$

- *Solution to the outer problem*

We now obtain the contribution of the adhesive zone. For this, we add the solutions of the external crack under pressure and appropriately modified solutions due to the unloading of a flat punch described in the preceding two sections.

We find the normal stress in the contact region due to the adhesive zone by adding (1.147) and (1.152):

$$\sigma_T(r,0) = \frac{-\sigma_0}{\pi}\left[\frac{1}{\sqrt{a^2-r^2}}\left(\sqrt{c^2-a^2} + \frac{c^2}{a}\cos^{-1}\left(\frac{a}{c}\right)\right) - 2\tan^{-1}\sqrt{\frac{c^2-a^2}{a^2-r^2}}\right]. \tag{1.156}$$

The total load acting in the contact region due to the above stress field is $p\pi\left(c^2-a^2\right)$, which balances the tensile load of $-p\pi\left(c^2-a^2\right)$ due to adhesive forces active in the adhesive zone. Thus, the total load acting on the punch is now zero.

We now introduce the outer stress intensity factor

$$K_m = \frac{-\sigma_0}{\sqrt{\pi a}}\left[\sqrt{c^2-a^2} + \frac{c^2}{a}\cos^{-1}\left(\frac{a}{c}\right)\right], \tag{1.157}$$

to represent the strength of the singularity in the contact stresses (1.156) due to only adhesive forces. The stress field (1.156) thus simplifies to

$$\sigma_T(r,0) = \frac{K_m}{\sqrt{\pi a}}\frac{a}{\sqrt{a^2-r^2}} + \frac{2\sigma_0}{\pi}\tan^{-1}\sqrt{\frac{c^2-a^2}{a^2-r^2}}. \tag{1.158}$$

The displacement δ_T of the punch due to only adhesive forces is found by adding (1.149) and (1.154):

$$\delta_T = -\frac{(1-\nu^2)}{\pi E}\frac{P'}{a}\frac{\pi}{2}. \tag{1.159}$$

Finally, the total distance between the interacting surfaces outside the contact zone is obtained by subtracting (1.155) from (1.148):

$$\begin{aligned} u_{yT} &= u_y - u'_y \\ &= \frac{2\left(1-\nu^2\right)}{\pi E} K_m \sqrt{\pi a} \cos^{-1}\left(\frac{a}{r}\right) - \frac{4\left(1-\nu^2\right)}{\pi E}\frac{\sigma_0}{\pi a}\left[\sqrt{c^2-a^2}\left\{\sqrt{r^2-a^2} - \right.\right. \\ &\quad \left.\left. a\cos^{-1}\left(\frac{a}{r}\right)\right\} - ac^2 \int_a^{\min(r,c)} \frac{\sqrt{r^2-t^2}}{t^2\sqrt{c^2-t^2}}\, dt\right] \quad \text{for } r > a. \end{aligned} \tag{1.160}$$

- *Final solutions for the adhesive-zone model*

Finally, we obtain expressions for the adhesive-zone model. First, we find the normal stresses in the contact region for the adhesive-zone model by adding (1.121) and (1.158):

$$\begin{aligned} \sigma_y(r,0) = &\frac{K_1}{\sqrt{\pi a}}\frac{a}{\sqrt{a^2-r^2}} - \frac{3K}{2\pi R}\sqrt{a^2-r^2} + \\ &\frac{K_m}{\sqrt{\pi a}}\frac{a}{\sqrt{a^2-r^2}} + \frac{2\sigma_0}{\pi}\tan^{-1}\sqrt{\frac{c^2-a^2}{a^2-r^2}} \quad \text{for } r < a. \end{aligned} \tag{1.161}$$

The load P acting on the punch is evaluated from (1.124):

$$P = \frac{a^3 K}{R} - 2aK_1\sqrt{\pi a}. \tag{1.162}$$

Finally, the punch's displacement δ is obtained by adding (1.120) and (1.159):

$$\delta = \frac{a^2}{3R} + \frac{2P}{3aK} + \frac{\left(1-\nu^2\right)}{E}\sigma_0 a\left[\frac{c^2}{a^2}\cos^{-1}\left(\frac{a}{c}\right) - \sqrt{\frac{c^2}{a^2}-1}\right]. \tag{1.163}$$

We note from (1.161) that the singularities at $r = \pm a$ in the contact stress vanishes if

$$K_1 = -K_m. \tag{1.164}$$

This reduces the contact stress distribution in (1.161) to

$$\sigma_y(r,0) = -\frac{3K}{2\pi R}\sqrt{a^2-r^2} + \frac{2\sigma_0}{\pi}\tan^{-1}\sqrt{\frac{c^2-a^2}{a^2-r^2}}. \tag{1.165}$$

We observe that $\sigma_y(\pm a, 0) = -\sigma_0$. Thus, the condition (1.164) also ensures the continuity

of the stress at the contact edges.

From (1.157) and (1.164), we obtain

$$K_1 = \frac{\sigma_0}{\sqrt{\pi a}} \left[\sqrt{c^2 - a^2} + \frac{c^2}{a} \cos^{-1}\left(\frac{a}{c}\right) \right]. \tag{1.166}$$

Substituting K_1 into (1.162) provides the load acting on the punch:

$$P = \frac{a^3 K}{R} - 2\sigma_0 a^2 \left\{ \sqrt{\frac{c^2}{a^2} - 1} + \frac{c^2}{a^2} \cos^{-1}\left(\frac{a}{c}\right) \right\}. \tag{1.167}$$

Employing the above in (1.163), and simplifying the resulting equation yields the displacement of the punch:

$$\delta = \frac{a^2}{R} - \frac{8\sigma_0}{3K}\sqrt{c^2 - a^2}. \tag{1.168}$$

Finally, the air-gap between the surfaces of the sphere and the half-space is obtained by adding (1.138) and (1.160):

$$[u_y] = \frac{a^2}{\pi R}\left[\sqrt{\frac{r^2}{a^2} - 1} + \left(\frac{r^2}{a^2} - 2\right) \cos^{-1}\left(\frac{a}{r}\right) \right] + \frac{4\left(1-\nu^2\right)}{\pi E}\frac{\sigma_0}{\pi a}\left[ac^2 \int_a^{\min(r,c)} \frac{\sqrt{r^2 - t^2}}{t^2\sqrt{c^2 - t^2}}\, dt - \sqrt{c^2 - a^2}\left\{ \sqrt{r^2 - a^2} - a\cos^{-1}\left(\frac{a}{r}\right) \right\} \right] \quad \text{for } r > a. \tag{1.169}$$

It now remains to find the extent c of the adhesive zone. To this end, we set $r = c$ in (1.169), invoke

$$\cos^{-1}\left(\frac{a}{c}\right) = \tan^{-1}\left(\sqrt{\frac{c^2}{a^2} - 1}\right)$$

and set $m = c/a$ in the resulting equation to obtain the air-gap at the edge of the adhesive zone

$$\delta_c = \frac{a^2}{\pi R}\left[\sqrt{m^2 - 1} + \left(m^2 - 2\right)\tan^{-1}\sqrt{m^2 - 1}\right] + \frac{4\left(1-\nu^2\right)}{\pi E}\sigma_0 a\left[\sqrt{m^2 - 1}\tan^{-1}\sqrt{m^2 - 1} - m + 1\right]. \tag{1.170}$$

We now employ the J-integral (Rice, 1968) to compute the energy release rate for the Dugdale-Barenblatt adhesive zone model as

$$G = \sigma_0 \delta_c. \tag{1.171}$$

Substituting for δ_c from (1.170) into the above we find

$$G = \frac{\sigma_0 a^2}{\pi R}\left\{\sqrt{m^2-1} + \left(m^2-2\right)\tan^{-1}\sqrt{m^2-1}\right\} + \frac{4\left(1-\nu^2\right)}{\pi E}\sigma_0^2 a\left\{\sqrt{m^2-1}\tan^{-1}\sqrt{m^2-1} - m + 1\right\}. \tag{1.172}$$

We may now find c by utilizing the Griffith's criterion (1.103), which yields

$$w = \frac{\sigma_0 a^2}{\pi R}\left[\sqrt{m^2-1} + \left(m^2-2\right)\tan^{-1}\sqrt{m^2-1}\right] + \frac{4\left(1-\nu^2\right)}{\pi E}\sigma_0^2 a\left[\sqrt{m^2-1}\tan^{-1}\sqrt{m^2-1} - m + 1\right]. \tag{1.173}$$

In an adhesive contact problem we know a, w and σ_0, so that the above equation can be solved to find $m = c/a$. We may now find the contact stress distribution $\sigma_y(r,0)$, the load acting on the punch P and the punch's displacement δ from, respectively, (1.165), (1.167) and (1.168).

1.4.5 Limits of the adhesive zone model

We now demonstrate how the JKR and DMT approximations may be obtained as limits of the adhesive-zone model. To this end, we first find σ_0 in terms of K_1 from (1.166) as

$$\sigma_0 = \frac{\pi K_1}{\sqrt{\pi a}}\left\{\sqrt{m^2-1} + m^2\tan^{-1}\left(\sqrt{m^2-1}\right)\right\}^{-1}. \tag{1.174}$$

Employing the above into (1.172), we obtain the energy release rate

$$G = \frac{a^2 K_1}{R\sqrt{\pi a}}\left\{1 - \frac{2\tan^{-1}\sqrt{m^2-1}}{\sqrt{m^2-1} + m^2\tan^{-1}\sqrt{m^2-1}}\right\} + \frac{4\left(1-\nu^2\right)}{E}K_1^2\left\{\frac{\sqrt{m^2-1}\tan^{-1}\sqrt{m^2-1} - m + 1}{\left(\sqrt{m^2-1} + m^2\tan^{-1}\sqrt{m^2-1}\right)^2}\right\}. \tag{1.175}$$

- *JKR limit*

To obtain the JKR approximation, we consider the limit $c/a \to 1$. In this limit, from (1.166) we have

$$\frac{K_1}{\sigma_0\sqrt{\pi a}} \to 0 \quad \text{as } \frac{c}{a} \to 1. \tag{1.176}$$

So, as $c/a \to 1$, the adhesive strength at the contact edges becomes singular, i.e. $\sigma_0 \to \infty$. Also, for $c/a \approx 1$ we have

$$\sqrt{c^2 - a^2} \approx (c^2/a)\, \cos^{-1}(a/c). \tag{1.177}$$

Thus, from (1.166) we obtain

$$\sqrt{c^2 - a^2} \approx \frac{K_1 \sqrt{\pi\, a}}{2\sigma_0}. \tag{1.178}$$

From (1.178), it is also implied that

$$d \approx \frac{\pi\, K_1^2}{8\sigma_0^2}. \tag{1.179}$$

where $d = c - a$. The parameter d shows the extent of adhesive zone outside contact area and this goes to zero in JKR approximation.

Now finding the stress distribution employing (1.165) and (1.174) yields

$$\begin{aligned} \sigma_y\,(r,0) \;\; = \;\; & -\frac{3K}{2\pi R}\sqrt{a^2 - r^2} + \frac{2K_1}{\sqrt{\pi a}} \tan^{-1} \sqrt{\frac{c^2 - a^2}{a^2 - r^2}} \times \\ & \left\{ \sqrt{\frac{c^2}{a^2} - 1} + \frac{c^2}{a^2} \tan^{-1} \left(\sqrt{\frac{c^2}{a^2} - 1} \right) \right\}^{-1}. \end{aligned} \tag{1.180}$$

Substituting $c = a + \epsilon$, where $\epsilon \ll 1$, in the above equation and expanding the resulting equation in a Taylor series about $\epsilon = 0$, we obtain

$$\sigma_y^{JKR}\,(r,0) \approx -\frac{3K}{2\pi R}\sqrt{a^2 - r^2} + \frac{K_1}{\sqrt{\pi a}} \frac{a}{\sqrt{a^2 - r^2}} + \mathcal{O}\,(\epsilon)\,. \tag{1.181}$$

The above leading order normal stress distribution is the JKR pressure distribution of (1.121). Integrating the above stress distribution we obtain the total load acting on the punch

$$P^{JKR} \approx \frac{a^3 K}{R} - 2\, a\, K_1 \sqrt{\pi a}. \tag{1.182}$$

Employing the above to find the stress intensity factor K_1 yields

$$K_1 \approx -\frac{1}{2\, a\, \sqrt{\pi a}} \left(P^{JKR} - \frac{a^3 K}{R} \right). \tag{1.183}$$

Next, we find the displacement δ in the JKR approximation from the adhesive zone model's solution given by (1.168). For this, we employ (1.178) in (1.168) to obtain

$$\delta^{JKR} \approx \frac{a^2}{R} - \frac{4}{3K} K_1 \sqrt{\pi a}. \tag{1.184}$$

Finding the stress intensity factor K_1 in terms of δ gives

$$K_1 \approx -\frac{3K}{4\sqrt{\pi a}} \left(\delta^{JKR} - \frac{a^2}{R} \right). \tag{1.185}$$

We now find the limiting value of the energy release rate G for the adhesive zone model given by (1.175) as $c/a \to 1$. For this, we expand (1.175) in a Taylor series as $m \to 1$:

$$G \approx \frac{1}{2} \frac{1-\nu^2}{E} K_1^2 + \mathcal{O}(m-1). \tag{1.186}$$

The above leading order estimate for G is the energy release rate in the JKR approximation; cf. (1.102).

Substituting K_1 from (1.183) or (1.185) in the leading order approximate of G given by (1.186) yields

$$G \approx \frac{1}{6\pi a^3 K} \left(\frac{a^3 K}{R} - P \right)^2 \approx \frac{3K}{8\pi a} \left(\delta - \frac{a^2}{R} \right)^2. \tag{1.187}$$

Employing Griffith's criterion (1.103) with the above we obtain

$$\frac{a^3 K}{R} \approx P + 3\pi w R \pm \sqrt{6\pi w R P + (3\pi w R)^2}. \tag{1.188}$$

and

$$\delta^{JKR} \approx \frac{a^2}{R} - \left(\frac{8\pi w a}{3K} \right)^{1/2}. \tag{1.189}$$

The above agrees with (1.127) and (1.126) obtained earlier.

Thus, we recover the JKR approximation from the adhesive zone model in the limit $c/a \to 1$. We may also conclude from (1.179) and (1.176) that as $c/a \to 1$, the adhesive zone size outside the contact area goes to zero and the stresses at the contact edges become singular.

- *DMT limit*

We now obtain the DMT theory as a limit of the adhesive zone model when $c/a \to \infty$, i.e. the adhesive zone extends to infinity. As $c/a \to \infty$, (1.166) yields

$$\frac{K_1}{\sigma_0\sqrt{\pi a}} \approx \frac{c^2}{2a^2} \to \infty. \tag{1.190}$$

Employing the above and finding the stress distribution from (1.165) gives

$$\sigma_y^{DMT}(r,0) \approx -\left(\frac{3K}{2\pi R} + \frac{2\sigma_0}{\pi c}\right)\sqrt{a^2 - r^2} + \sigma_0. \tag{1.191}$$

From (1.190) as $c/a \to \infty$, the adhesive strength $\sigma_0 \to 0$ and, hence, the stresses above reduce to the Hertzian distribution, which is the assumed stress distribution in the DMT approximation as well.

To find the limit of δ given by (1.168) as $c/a \to \infty$, we first obtain the adhesive strength σ_0 from (1.190) as

$$\sigma_0 = \frac{K_1}{\sqrt{\pi a}}\frac{2a^2}{c^2}. \tag{1.192}$$

Combining the above with (1.168) yields

$$\delta^{DMT} \approx \frac{a^2}{R} - \frac{16K_1}{\sqrt{\pi a}}\frac{a}{c}\sqrt{1 - \frac{a^2}{c^2}}. \tag{1.193}$$

Taking the limit $c/a \to \infty$, the above reduces to

$$\delta \approx \frac{a^2}{R}. \tag{1.194}$$

The above matches the punch displacement in DMT approximation, which is assumed to be the same as in Hertzian contact. This is due to the fact that in DMT approximation, the adhesive forces acting outside the contact region will not cause any deformations in the elastic bodies. Thus, the displacement in these bodies is only due to the contact pressure, which is Hertzian.

Finally, we obtain the relationship between a and P in the DMT approximation. As

$c/a \to \infty$, employing (1.190), we may write (1.167) as

$$P \approx \frac{a^3 K}{R} - 2aK_1\sqrt{\pi a}. \tag{1.195}$$

Finding the stress intensity factor from the above we obtain

$$K_1 \approx \frac{1}{2a\sqrt{\pi a}}\left(\frac{a^3 K}{R} - P\right). \tag{1.196}$$

To find the energy release rate G in the DMT approximation, we expand (1.175) in a Taylor series about $m \to \infty$:

$$G \approx \frac{K_1 a^2}{R\sqrt{\pi a}} + \mathcal{O}\left(\frac{1}{m^2}\right). \tag{1.197}$$

Substituting K_1 from (1.196) into the leading order approximate of energy release rate G yields

$$G \approx \frac{1}{2\pi R}\left(\frac{a^3 K}{R} - P\right). \tag{1.198}$$

The above matches with the energy release rate in the DMT approximation, cf. (1.140). Finally, employing the Griffith criterion (1.103), we find

$$\frac{a^3 K}{R} \approx P + 2\pi w R. \tag{1.199}$$

The above agrees with the DMT result given by (1.139).

From the above discussions, we conclude that by considering $c/a \to \infty$, which is equivalent to the adhesive stress outside the contact zone going to zero, i.e. $\sigma_0 \to 0$, we recover the DMT approximation for adhesive contact.

1.4.6 Summary

Finally, we summarize how Maugis (1992) resolved differences between the JKR and DMT approximation:

(i) In Maugis (1992), the stresses outside the contact region are taken into account employing an adhesive zone model. And these stresses are considered to be constant, i.e. $\sigma_y = -\sigma_0$ for $a^+ < r < c$.

(ii) According to Maugis (1992), both compressive and tensile stresses are allowed inside the contact region. The stresses at the contact edges do not go either to zero or to infinity. Instead their value will be $-\sigma_0$, i.e. $r \to a^-, \sigma_y \to -\sigma_0$. Thus, there is no discontinuity in the normal stresses at the contact edge, i.e. $r \to a^{\pm}, \sigma_y \to -\sigma_0$.

(iii) From Maugis (1992), the extent of deformation caused by adhesive forces depends upon the non-dimensional adhesion parameter $\lambda = 2\sigma_0 \left(R/\pi w K^2\right)^{1/3}$. At small λ, the adhesion is small compared to the elastic material's Young's modulus. Thus, the adhesive forces cause minimal deformation in the elastic bodies. However, when λ is high, adhesive forces are dominant and/or the material is soft. In this case the adhesive forces deform the elastic bodies and, hence, neck formations are seen at the contact edges.

We see that employing the adhesive-zone model removes the singularities and discontinuities from the contact pressure.

For a more detailed discussion on two-dimensional adhesive contact employing the adhesive zone model and it's corresponding JKR and DMT limits, the reader is suggested to refer Baney and Hui (1997).

1.5 Thesis outline

In the remaining part of this thesis, we discuss indentation by a rigid circular punch of an adhesive elastic layer supported at its ends. In this discussion we limit ourselves to two-dimensional plane strain indentation. We model the adhesion between the interacting surfaces through the adhesive-zone model, in which a constant stress σ_0 acts outside the contact zone and within the adhesive zone. We then obtain the results for different types of contact, i.e. non-adhesive 'Hertzian' contact, JKR approximation, and the transition of the JKR to DMT, by varying the adhesion parameter λ. Now, we provide a brief outline to the subsequent chapters.

In Chapter 2, we start with a mathematical formulation for the indentation of an adhesive elastic layer supported by flexible end supports. We employ displacements due to a point load of an Euler-Bernoulli beam to estimate the displacement of the bottom surface of the elastic layer. We discuss results for different types of contacts in detail. While doing so,

we compare our theoretical results with FE simulations and previously published results. We also outline an experimental procedure for an adhesive contact of beam, and compare our theoretical results with those of preliminary experiments. Finally, we demonstrate the utility of our approach to model structural adhesive.

In Chapter 3, we describe a more general formulation, which is free from the assumptions of Chapter 2. In this formulation, we limit ourselves to clamped and simply supported beams, as these are the two extreme limits for a beam supported on flexible end supports. Finally, we discussed the results for different types of contacts using this approach and compared these results against the results of Chapter 2.

In Chapter 4, we briefly conclude and then discuss the possible extensions for the current work.

भारतीय प्रौद्योगिकी संस्थान कानपुर
INDIAN INSTITUTE OF TECHNOLOGY KANPUR

Chapter 2

Contact mechanics of adhesive beams: Low to moderate indentation.

2.1 Introduction

Research in patterned adhesives is often motivated by the structures of natural adhesives, such as those present in the feet of gekkos; see e.g. Hiller (1976), and Arul and Ghatak (2008). In conventional adhesives, such as thin, sticky tapes, only the top and bottom surfaces are active. However, multiple surfaces may be activated with appropriate patterning. With more surfaces participating in the adhesion process the adhesives show increased hysteresis and, so, better performance. One example of a patterned adhesive is the structural adhesive shown in Fig. 2.1(a), which was developed by Arul and Ghatak (2008). Figure 2.1(b) shows a possible mechanical model of the structural adhesive of Fig. 2.1(a) that utilizes several interacting adhesive beams. This motivates the goal of this study, which is to investigate the adhesive contact of a beam; see Fig. 2.2(a).

Contact with a half-space has been well studied over the past century, and we refer the reader to Alexandrov and Pozharskii (2001), and also the texts of Galin and Gladwell (2008), Gladwell (1980), Johnson (1985), Hills et al. (1993) and Goryacheva (1998). At the same time, the contact of thin layers is an active area of research in view of applications to electronics and computer industry; see, e.g. Barthel and Perriot (2007), and Dalmeya

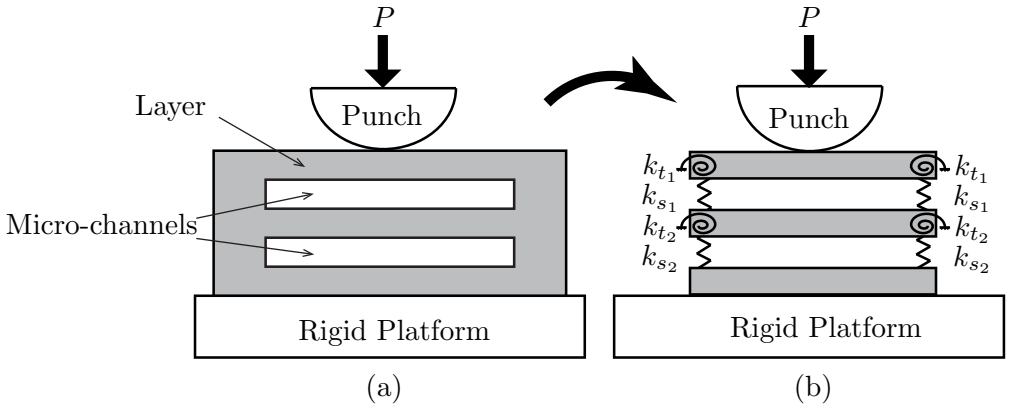

Figure 2.1: (a) Structural adhesive designed by Arul and Ghatak (2008). (b) Mechanical model of the structural adhesive in (a) employing an interconnected stack of adhesive beams. The rigidity of the vertical walls is modeled through torsional (stiffness k_t) and vertical translational (stiffness k_s) springs, as shown. The system is indented by a rigid punch, pressed down by the force P.

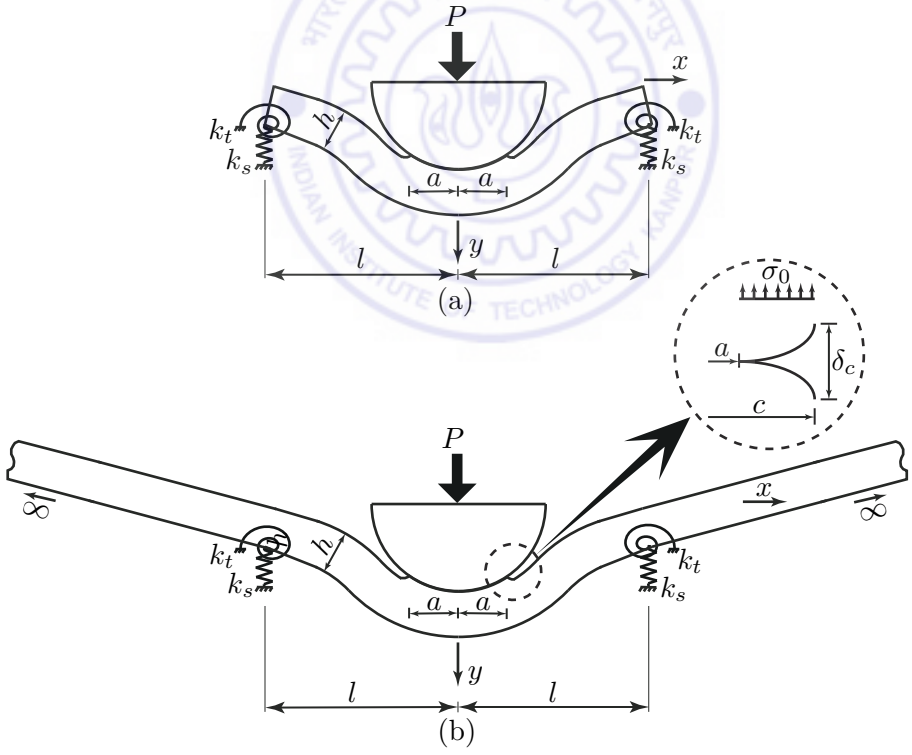

Figure 2.2: (a) Indentation by a rigid cylindrical punch of an adhesive beam resting upon flexible supports. The flexible supports are modeled through torsional and vertical translational springs with stiffnesses k_t and k_s, respectively. (b) Mathematical model of the indentation process shown in (a). The inset shows details of the adhesive zone active near the contact edges; see text for details. The vertical deflection is exaggerated for ease of representation.

et al. (2012). In contrast, the indentation of beams is much less studied.

Seeking the solution to the indentation of a beam through a strength-of-materials approach overlooks the local contact mechanics. To probe the latter, it is necessary to formulate an elasticity problem with appropriate boundary conditions. This is typically a complex problem, and has prompted some alternate approaches to adhesion*less* contact, as discussed in the next paragraph. A careful study of the adhesive contact of beams with a rigid cylindrical punch is not yet available and will be helpful for several applications.

Two-dimensional adhesionless indentation of a beam has been studied in the past by Keer and Silva (1970), Keer and Miller (1983), Keer and Schonberg (1986), Sankar and Sun (1983), Sun and Sankar (1985), and Kim et al. (2014). Keer and Miller (1983) modeled the beam as a linear elastic layer of infinite extent with frictionless bottom and top surfaces. First, the elasticity problem was solved through Fourier transforms, see e.g. (Sneddon, 1995, p. 395-414). Then, employing the Hankel transform (Gladwell, 1980, p. 213) for the pressure distribution, and asymptotically matching the far-field displacements with those obtained from Euler-Bernoulli beam theory, a Fredholm integral equation of the second kind was obtained. This equation was solved numerically.

Sankar and Sun (1983) employed Fourier series in their investigation of adhesionless contact with beams of finite length. Their results were in good agreement with those of Keer and Miller (1983). Recently, Kim et al. (2014) studied beam indentation through asymptotics. Finite element (FE) simulations were also carried out. The contact parameters, i.e. contact area and the total load acting on the punch, obtained through asymptotics, matched results of FE simulations well. In all these studies, the interaction of the beam with the punch is non-adhesive. However, extending these methods to adhesive beams is difficult due to the presence of several iterated integral transforms.

Recently, adhesive beams are studied by Zhang and Li (2011), Wagner and Vella (2012), and Hu and Adams (2016), as they found applications in nano (or) micro electro mechanical systems (NEMs/MEMs). Zhang and Li (2011) investigated the adhesive interaction of graphene layers with a patterned elastic substrate. A theoretical model based on the minimum energy principle was developed to study the contact characteristics of graphene layers with different patternings in the elastic substrate by varying the number of graphene layers. Wagner and Vella (2012) studied the interaction of graphene sheets with a grooved

surface formed inside a rigid substrate. The graphene sheets placed over the grooved surface form a conformal contact over some of its length depending on their adhesive characteristics and bending stiffness. The graphene sheets area modeled as beam employing the Euler-Bernoulli beam theory. Tension in the graphene sheets was neglected. A simple theoretical method was developed employing the minimum energy principle to study the effect of graphene adhesion on contact characteristics. Later, Hu and Adams (2016) extended the analysis of Wagner and Vella (2012) by considering the tension in the graphene sheets.

Sekiguchi et al. (2012) studied the interaction of an adhesive beam, whose bottom surface is brought (pressed) into the contact at an angle, with a rigid, flat surface, as they found applications in grip-and-release processes. The load, displacement and contact area relationships in these adhesive beams are obtained employing the minimum energy principle. In each case, classical beam theories were employed and no effort was made to resolve the details of the contact, e.g. the local pressure distribution.

The recent studies on other structural adhesives like membranes, which are close to beams, include Long et al. (2010), Laprade et al. (2013) and Srivastava and Hui (2013), also highlights the importance of this study. Long et al. (2010) and Laprade et al. (2013) studied the contact mechanics of inflated and highly deformed axi-symmetrical membranes with and without adhesion. Srivastava and Hui (2013) extended this to inflated and highly deformed rectangular membranes.

Here, we propose an alternative approach to the contact of a beam with a rigid punch, shown in Fig. 2.2(a), that models both non-adhesive and adhesive interactions in a straightforward manner. Adhesion is modeled through the introduction of an adhesive zone that extends beyond the contact zone, as shown in the inset of Fig. 2.2(b). An adhesive zone model allows us to investigate the effect of adhesion by admitting continuous variations in it's strength. The popular JKR Johnson et al. (1971) and DMT Derjaguin et al. (1975) models for adhesion are obtained as special cases. The non-adhesive case ('Hertzian contact') is found by setting the adhesion strength to zero.

This chapter is organized as follows. We start by formulating a mathematical model for the adhesive contact of the beam shown in Fig. 2.2(a). We will obtain a Fredholm integral equation of the first kind that relates the contact pressure distribution with the vertical

displacement in the contact patch. Relevant conditions at the edge of the contact zone will also be derived. This integral equation is then solved numerically employing Galerkin projections in terms of Chebyshev polynomials. Theoretical results are compared with FE simulations whenever possible. We then explore the effect of various parameters in the problem, viz. flexibility of end supports, strength of adhesion, the beam's geometry, etc. We close with a comparison with preliminary experimental results, and an application of our solution to complex structural adhesives, such as the one shown in Fig. 2.1(a).

2.2 Mathematical model

We begin by extending the finite beam of Fig. 2.2(a), whose length is $2l$, beyond the supports to infinity, as shown in Fig. 2.2(b). The extension is done in a manner consistent with the kinematic and kinetic constraints imposed by the supports. Thus, the beam is extended linearly along its slope at the supports. The beam may now be thought of as a linear elastic layer of infinite length with thickness h. The beam is isotropic and homogeneous, with Young's modulus E and Poisson's ratio ν. The top and bottom surfaces of the beam are frictionless.

During indentation, a normal traction distribution $-P_c(x)$ acts on the top surface [1]. At this time, the vertical displacement of the bottom surface is $v_b(x)$, which is typically *not* known. When the contact area is less than the beam's thickness, we assume that $v_b(x)$ may be approximated by the displacement obtained from Euler-Bernoulli beam theory when a point load of magnitude P acts at the center of the top surface, as depicted in Fig. A.1. The details of how $v_b(x)$ is calculated for a beam on flexible supports are provided in Appendix A.

The governing equations for the horizontal (u) and vertical (v) displacements in the extended beam (elastic layer) of Fig. 2.2(b), assuming plane strain, are given by

$$\frac{2\,(1-\nu)}{1-2\nu}\frac{\partial^2 u}{\partial x^2}+\frac{\partial^2 u}{\partial y^2}+\frac{1}{1-2\nu}\frac{\partial^2 v}{\partial x\partial y}=0 \tag{2.1a}$$

and

$$\frac{\partial^2 v}{\partial x^2}+\frac{2\,(1-\nu)}{1-2\nu}\frac{\partial^2 v}{\partial y^2}+\frac{1}{1-2\nu}\frac{\partial^2 u}{\partial x\partial y}=0, \tag{2.1b}$$

which reflect horizontal and vertical linear momentum balance, respectively; see, e.g.

[1] The negative sign is introduced in order to report compressive pressure during contact as positive.

(Timoshenko and Goodier, 1970, p. 241) or (Sadd, 2005, p. 125). The boundary conditions may be taken to be

$$\sigma_{xy} = 0, \qquad \sigma_{yy} = -P_c(x) \quad \text{on the top surface, i.e. at } y = 0, \tag{2.2a}$$

and $$\sigma_{xy} = 0, \qquad v = v_b(x) \quad \text{on the bottom surface, i.e. at } y = h. \tag{2.2b}$$

We now follow (Sneddon, 1995, p. 402) to map the above problem into Fourier space by transforming the x coordinate. Solving for the vertical displacement in Fourier space and, then, taking the inverse Fourier transform yields the following integral equation for the vertical displacement of the top surface:

$$\begin{aligned} v\,(x,0) = &-\frac{2}{\pi E^*}\int_0^\infty \bar{P}_c\,(\xi)\,\frac{\sinh^2\xi\,h}{\xi\,(\xi\,h+\sinh\xi\,h\cosh\xi\,h)}\,\cos\xi x\,d\xi \\ &+\frac{1}{\pi}\int_0^\infty \bar{v}_b\,(\xi)\,\frac{\sinh\xi\,h+\xi\,h\cosh\xi\,h}{\xi\,h+\sinh\xi\,h\cosh\xi\,h}\,\cos\xi x\,d\xi, \end{aligned} \tag{2.3}$$

where $E^* = E/\,(1-\nu^2)$,

$$\bar{P}_c\,(\xi) = \int_{-\infty}^\infty -P_c\,(t)\cos\xi t\,dt \quad \text{and} \quad \bar{v}_b\,(\xi) = \int_{-\infty}^\infty v_b\,(t)\cos\xi t\,dt. \tag{2.4}$$

Appendix C provides details of how (2.3) is obtained. For non-dimensionalizing it is more convenient to rewrite (2.3) as

$$\begin{aligned} v\,(x,0) = &\frac{2}{\pi E^*}\int_0^\infty\int_{-\infty}^\infty P_c\,(t)\cos\xi t\,dt\,\frac{\sinh^2\xi\,h}{\xi\,(\xi\,h+\sinh\xi\,h\cosh\xi\,h)}\,\cos\xi x\,d\xi \\ &+\frac{1}{\pi}\int_0^\infty\int_{-\infty}^\infty v_b\,(t)\cos\xi t\,dt\,\frac{\sinh\xi\,h+\xi\,h\cosh\xi\,h}{\xi\,h+\sinh\xi\,h\cosh\xi\,h}\,\cos\xi x\,d\xi, \end{aligned} \tag{2.5}$$

where we have invoked definitions (2.4) of $\bar{P}_c$ and $\bar{v}_b$.

In contact problems the vertical displacement within the contact region is constrained. For example, during indentation with a rigid punch, the surface in the contact region must conform to the shape of the punch. We now approximate the profile of the cylindrical punch of radius R as a parabola in the contact region, as is appropriate if the indentation depth, and the dimensions of the contact region are much smaller than the radius of curvature of the punch. We set δ to be the vertical displacement of the punch. This allows

us to write the vertical displacement of the beam's top surface within the contact region as

$$v(x,0) = \delta - \frac{x^2}{2R}, \quad -a \leq x \leq a, \tag{2.6}$$

where the contact region lies between $-a$ and a.

During contact, the pressure on the beam's top surface depends also on the adhesive interaction between the beam and the punch. This adhesive interaction is, in turn, introduced through the presence of an adhesive zone; see inset of Fig. 2.2(b). Within the adhesive zone the adhesive interaction is modeled through a Dugdale-Barenblatt model Maugis (1992), which assumes the adhesion to be of constant strength σ_0. Thus, we may write the force distribution on the beam's top surface as

$$P_c(x) = \begin{cases} p(x), & |x| \leq a \\ -\sigma_0, & a < |x| \leq c \\ 0, & |x| > c, \end{cases} \tag{2.7}$$

where c locates the outer edge of the adhesive zone; see inset in Fig. 2.2(b). Adhesive zones were introduced by Maugis (1992) in order to avoid the singularity in the pressure at the contact edge ($x = \pm a$) found in JKR theory. For this, it is also necessary that there be no discontinuity in the contact pressure at the contact edge, i.e.

$$\lim_{x \to \pm a^-} p(x) = -\sigma_0. \tag{2.8}$$

To close our mathematical description we require an additional equation to compute the extent c of the adhesive zone. This is obtained by equating the energy release rate computed from the $J-$integral Rice (1968) and the work of adhesion w, which leads to

$$\sigma_0 \delta_c = w, \tag{2.9}$$

where

$$\delta_c = \left(c^2/2R\right) - \delta + v_c \tag{2.10}$$

is the air-gap at which the adhesive forces vanish and $v_c = v(c,0)$; see inset in Fig. 2.2(b). During non-adhesive indentation (2.10) is automatically satisfied as $\sigma_0 = 0 = w$. The JKR approximation is obtained in the limits $\sigma_0 \to \infty$ and $c \to a$, at which the energy

balance (2.9) becomes

$$\frac{K_1^2}{2E^*} = w, \tag{2.11}$$

where

$$K_1 = -\lim_{x \to a^-} \sqrt{2\pi\,(a-x)}\, p\,(x) \tag{2.12}$$

is the *stress intensity factor* that measures the strength of the square root singularity in the pressure at the contact edge; see Maugis (1992). This is equivalent to Griffith's criterion in fracture mechanics; see e.g. (Kanninen and Popelar, 1985, p. 168). In this limit, we do not require the contact pressure end condition (2.8).

Finally, the total load acting on the punch is found by integrating the normal traction over the top surface of the beam:

$$P = \int_{-\infty}^{\infty} P_c\,(x)\; dx = \int_{-a}^{a} p\,(x)\, dx - 2\,\sigma_0\,(c-a)\,. \tag{2.13}$$

2.3 Non-dimensionalization

We introduce the following non-dimensional parameters:

$$A = \frac{a}{l}; \quad \varphi\,(\tau) = \frac{aRl}{Kh^3} p\,(a\bar{\tau})\,; \quad \bar{P} = \frac{PRl}{Kh^3}; \quad k_t^f = \frac{k_t l}{EI}; \quad k_s^f = \frac{k_s l^3}{EI};$$
$$\Delta = \frac{\delta R}{l^2}; \quad L = \frac{l}{R}; \quad \lambda = 2\sigma_0 \left(\frac{R}{\pi w K^2}\right)^{1/3}; \quad m = \left(\frac{\pi w}{RK}\right)^{1/3},$$

where $K = 4\,E^*/3$ and $I = h^3/12$ is the beam's area moment of inertia. We also define the scaled variables

$$\{\bar{x}, \bar{\tau}, \bar{c}, \bar{\gamma}\} = \frac{1}{a}\,\{x, t, c, h\}\,; \quad \{\hat{\tau}, \hat{\gamma}\} = \frac{1}{l}\,\{t, h\}\,; \quad \{\omega, \bar{\omega}, \hat{\omega}\} = \left\{\xi h, \frac{\omega}{\bar{\gamma}}, \frac{\omega}{\hat{\gamma}}\right\};$$
$$\{\vartheta\,(\bar{x}, 0)\,, \vartheta_b\,(\hat{\tau})\} = \frac{R}{l^2}\,\{v\,(\bar{x}, 0)\,, v_b\,(l\hat{\tau})\}\,; \quad \bar{I} = \frac{I}{h^3} = \frac{1}{12}; \quad \Phi\,(\tau) = \frac{aRl}{Kh^3}\, P_c\,(a\bar{\tau})\,.$$

In terms of these variables the non-dimensional vertical displacement of the top surface (2.5) becomes

$$\vartheta\left(\bar{x},0\right) = \frac{8\hat{\gamma}^3}{3\pi}\int_0^{\infty}\int_{-\infty}^{\infty}\Phi\left(\bar{\tau}\right)\cos\left(\bar{\omega}\bar{\tau}\right)\,d\bar{\tau}\;K_1\left(\bar{\omega},\bar{x}\right)\;d\omega \quad + \\ \frac{1}{\pi\hat{\gamma}}\int_0^{\infty}\int_{-\infty}^{\infty}\vartheta_b\left(\hat{\tau}\right)\cos\hat{\omega}\hat{\tau}\,d\hat{\tau}\;K_2\left(\bar{\omega},\bar{x}\right)\,d\omega, \tag{2.14}$$

with the kernels

$$K_1\left(\bar{\omega},\bar{x}\right) = \frac{\sinh^2\omega}{\omega\left(\omega+\sinh\omega\cosh\omega\right)}\,\cos\left(\bar{\omega}\bar{x}\right)$$

and

$$K_2\left(\bar{\omega},\bar{x}\right) = \frac{\sinh\omega+\omega\cosh\omega}{\omega+\sinh\omega\cosh\omega}\,\cos\left(\bar{\omega}\bar{x}\right).$$

From (2.7), we obtain the non-dimensional pressure on the beam's top surface:

$$\Phi\left(\bar{\tau}\right) = \begin{cases} \varphi\left(\bar{\tau}\right), & |\bar{\tau}| \le 1 \\ -\lambda Am/2\hat{\gamma}^3 L, & 1 < |\bar{\tau}| \le \bar{c} \\ 0, & |\bar{\tau}| > \bar{c}. \end{cases} \tag{2.15}$$

Combining (2.14) and (2.15) yields

$$\vartheta\left(\bar{x},0\right) = -\frac{8\hat{\gamma}^3}{3\pi}\int_0^{\infty}\bar{\varphi}\left(\bar{\omega}\right)\,K_1\left(\bar{\omega},\bar{x}\right)\,d\omega - \frac{8\lambda Am}{3\pi L}\int_0^{\infty}\bar{\varphi}_0\left(\bar{\omega}\right)\,K_1\left(\bar{\omega},\bar{x}\right)\,d\omega \\ + \frac{1}{\pi\hat{\gamma}}\int_0^{\infty}\hat{\vartheta}_b\left(\hat{\omega}\right)\,K_2\left(\bar{\omega},\bar{x}\right)\,d\omega, \tag{2.16}$$

with

$$\bar{\varphi}\left(\bar{\omega}\right) = -\int_{-1}^{1}\varphi\left(\bar{\tau}\right)\cos\left(\bar{\omega}\,\bar{\tau}\right)\,d\bar{\tau}, \quad \bar{\varphi}_0\left(\bar{\omega}\right) = \int_1^{\bar{c}}\cos\left(\bar{\omega}\,\bar{\tau}\right)\,d\bar{\tau}$$

and

$$\hat{\vartheta}_b\left(\hat{\omega}\right) = \int_{-\infty}^{\infty}\vartheta_b\left(\hat{\tau}\right)\cos\left(\hat{\omega}\hat{\tau}\right)\,d\hat{\tau}. \tag{2.17}$$

Non-dimensionalizing the displacement in the contact region (2.6), the contact pressure end condition (2.8), and the energy equation (2.9) lead to, respectively,

$$\vartheta(\bar{x},0) = \Delta - \frac{1}{2}\,\bar{x}^2 A^2 \quad \text{for} \quad -1 \le \bar{x} \le 1, \tag{2.18}$$

$$\varphi\,(\pm 1) = -\frac{\lambda\, Am}{2\,\hat{\gamma}^3 L} \tag{2.19}$$

and

$$1 = \frac{\pi\lambda L^2}{2m^2}\left[\frac{\bar{c}^2 A^2}{2} - \Delta + \vartheta_c\right], \tag{2.20}$$

where $\vartheta_c = \vartheta\,(\bar{c},0)$ and Δ is the non-dimensional displacement of the punch. Combining (2.11) and (2.12), and non-dimensionalizing, we obtain

$$\lim_{\bar{x}\to 1^-} \sqrt{(1-\bar{x})}\varphi\,(\bar{x}) = -\frac{m}{2\pi L}\left(\frac{l}{h}\right)^3 \sqrt{\frac{3Am}{L}}, \tag{2.21}$$

which replaces (2.19) and (2.20) whenever we invoke the JKR approximation.

The total non-dimensional load acting on the punch is found from (2.13):

$$\bar{P} = \int_{-1}^{1} \varphi\,(\bar{\tau})\; d\bar{\tau} - \frac{\lambda Am}{\hat{\gamma}^3 L}\,(\bar{c}-1)\,. \tag{2.22}$$

Finally, evaluating (2.16) in the contact region, i.e. for $-1 \le \bar{x} \le 1$, and employing (2.18) we obtain

$$\begin{aligned}\Delta - \frac{1}{2}\,\bar{x}^2 A^2 = &-\frac{8\hat{\gamma}^3}{3\pi}\int_0^\infty \bar{\varphi}\,(\bar{\omega})\; K_1\,(\bar{\omega},\bar{x})\;\; d\omega - \frac{8\lambda Am}{3\pi L}\int_0^\infty \bar{\varphi}_0\,(\bar{\omega})\; K_1\,(\bar{\omega},\bar{x})\;\; d\omega \\ &+ \frac{1}{\pi\hat{\gamma}}\int_0^\infty \hat{\vartheta}_b\,(\hat{\omega})\; K_2\,(\bar{\omega},\bar{x})\;\; d\omega.\end{aligned} \tag{2.23}$$

This is a Fredholm integral equation of first kind; see (Polyanin and Manzhirov, 2008, p. 573). We now solve the above equation, along with boundary conditions (2.19) and (2.20), for the contact pressure $\varphi\,(\bar{x})$, displacement Δ and the location $\bar{c}$ of the adhesive zone's edge, at a given contact area A.

2.4 Numerical solution

The integral equation (2.23) does not admit an analytical solution due to the complex kernels present. Thus, we solve it numerically. To this end, we approximate the unknown pressure distribution $p(x)$ in the contact region through a series of Chebyshev polynomials. Chebyshev polynomials are chosen due to their spectral convergence; see (Mason and Handscomb, 2003, p. 63).

The unknown non-dimensional pressure distribution is expressed as a series of Chebyshev polynomials of the first kind, viz.

$$\varphi(\bar{\tau}) = -\frac{\lambda A m}{2\hat{\gamma}^3 L} + \frac{1}{\sqrt{1-\bar{\tau}^2}} \sum_{n=0}^{N} b_{2n} T_{2n}(\bar{\tau}), \tag{2.24}$$

where b_{2n} are unknown constants that are to be found. Only even Chebyshev polynomials are considered as the problem is symmetric about the origin. The constant term in the approximation is introduced to explicitly account for the continuity condition (2.19) that is imposed on the contact pressure at the edge of the contact zone.

Employing (2.24) to evaluate the integrals $\bar{\varphi}(\bar{\omega})$ and $\bar{\varphi}_0(\bar{\omega})$ from (2.17), we obtain, respectively,

$$\bar{\varphi}(\bar{\omega}) = \frac{\lambda A m}{\hat{\gamma}^3 L} \frac{\sin\bar{\omega}}{\bar{\omega}} - \sum_{n=0}^{N} b_{2n} \alpha_{2n}(\bar{\omega}) \tag{2.25}$$

and

$$\bar{\varphi}_0(\bar{\omega}) = \frac{1}{\bar{\omega}} \left(-\sin\bar{\omega} + \sin\bar{\omega}\bar{c}\right), \tag{2.26}$$

where

$$\alpha_{2n}(\bar{\omega}) = \int_{-1}^{1} \frac{1}{\sqrt{(1-\tau^2)}} T_{2n}(\bar{\tau}) \cos\bar{\omega}\bar{\tau} \; d\bar{\tau}. \tag{2.27}$$

Appendix D provides details of how $\alpha_{2n}(\bar{\omega})$ are computed. Combining (2.22) and (2.24), we find the total load acting on the punch to be

$$\bar{P} = \pi b_0 - \frac{\lambda A m}{\hat{\gamma}^3 L} \bar{c}. \tag{2.28}$$

The displacement of the beam's bottom surface $\bar{\vartheta}_b(\hat{\omega})$ may, with (2.28), be written as

$$\frac{1}{\pi\hat{\gamma}} \hat{\vartheta}_b(\hat{\omega}) = \frac{4}{3\hat{\gamma}\bar{I}(1-\nu^2)} \left(b_0 - \frac{\lambda A m \bar{c}}{\pi\hat{\gamma}^3 L}\right) \hat{\vartheta}_p(\hat{\omega}), \tag{2.29}$$

where $\bar{I}$ is the scaled area moment of inertia, and the exact form of $\bar{\vartheta}_p$ depends upon how the beam is supported at its ends; see Appendix A.

The vertical displacement in the contact region may be expressed in terms of Chebyshev polynomials as

$$\Delta - \frac{1}{2}\,\bar{x}^2 A^2 = \sum_{n=0}^{N} a_{2n} T_{2n}\left(\bar{x}\right) = \left(\Delta - \frac{A^2}{4}\right) T_0\left(\bar{x}\right) - \frac{A^2}{4} T_2\left(\bar{x}\right). \tag{2.30}$$

Employing expansions (2.24)–(2.30) in the integral equation (2.23), we obtain

$$\begin{aligned}\sum_{n=0}^{N} a_{2n} T_{2n}\left(\bar{x}\right) =& \frac{8\hat{\gamma}^3}{3\pi} \sum_{n=0}^{N} b_{2n} \mathcal{J}_{2n}^{(1)}\left(\bar{x}\right) - \frac{8\lambda A m}{3\pi L} \mathcal{J}^{(1)}\left(\bar{x}\right) \quad + \\ & \frac{4}{3\hat{\gamma}\bar{I}\left(1-\nu^2\right)} \left(b_0 - \frac{\lambda A m \bar{c}}{\pi \hat{\gamma}^3 L}\right) \mathcal{J}^{(2)}\left(\bar{x}\right), \end{aligned} \tag{2.31}$$

where

$$\mathcal{J}_{2n}^{(1)}\left(\bar{x}\right) = \int_0^{\infty} \alpha_{2n}\left(\bar{\omega}\right)\, K_1\left(\bar{\omega}, \bar{x}\right)\, d\omega,$$

$$\mathcal{J}^{(1)}\left(\bar{x}\right) = \int_0^{\infty} \frac{\sin \bar{\omega}\, \bar{c}}{\bar{\omega}}\, K_1\left(\bar{\omega}, \bar{x}\right)\, d\omega$$

and

$$\mathcal{J}^{(2)}\left(\bar{x}\right) = \int_0^{\infty} \hat{\vartheta}_p\left(\hat{\omega}\right)\, K_2\left(\bar{\omega}, \bar{x}\right)\, d\omega.$$

We evaluate the above integrals at any $\bar{x}$ through the Clenshaw-Curtis quadrature (Press et al., 1992, p. 196). We now follow (Gladwell, 1980, p. 267) and utilize Galerkin projections to solve (2.31) for the unknown coefficients b_{2n}. To this end, we multiply both sides of (2.31) by $T_{2m}\left(\bar{x}\right)/\sqrt{1-\bar{x}^2}$, for $m = 0, \cdots, N$, and integrate from $\bar{x} = -1$ to $\bar{x} = 1$. This yields the following system of $N+1$ linear algebraic equations:

$$\sum_{n=0}^{N} a_{2n} \mathcal{J}_{nm} = \frac{8\hat{\gamma}^3}{3\pi} \sum_{n=0}^{N} b_{2n} \mathcal{J}_{nm}^{(1)} - \frac{8\lambda A m}{3\pi L} \mathcal{J}_m^{(1)} + \frac{4}{3\hat{\gamma}\bar{I}\left(1-\nu^2\right)} \left(b_0 - \frac{\lambda A m \bar{c}}{\pi \hat{\gamma}^3 L}\right) \mathcal{J}_m^{(2)}, \tag{2.32}$$

where

$$\mathcal{J}_{nm} = \int_{-1}^{1} \frac{T_{2n}(\bar{x})\, T_{2m}(\bar{x})}{\sqrt{1-\bar{x}^2}}\, d\bar{x}, \qquad \mathcal{J}^{(1)}_{nm} = \int_{-1}^{1} \frac{\mathcal{J}^{(1)}_{2n}(\bar{x})\, T_{2m}(\bar{x})}{\sqrt{1-\bar{x}^2}}\, d\bar{x},$$

$$\mathcal{J}^{(1)}_{m} = \int_{-1}^{1} \frac{\mathcal{J}^{(1)}(\bar{x})\, T_{2m}(\bar{x})}{\sqrt{1-\bar{x}^2}}\, d\bar{x} \quad \text{and} \quad \mathcal{J}^{(2)}_{m} = \int_{-1}^{1} \frac{\mathcal{J}^{(2)}(\bar{x})\, T_{2m}(\bar{x})}{\sqrt{1-\bar{x}^2}}\, d\bar{x}.$$

The foregoing integrals are evaluated through a Gauss-Chebyshev quadrature (Gladwell, 1980, p. 260).

Equations for b_{2n}, Δ and $\bar{c}$ are now obtained. Employing the expansion (2.24) in the contact pressure end condition (2.19) yields

$$b_0 + b_2 + \cdots + b_{2N} = 0. \tag{2.33}$$

The energy balance (2.20) provides

$$\frac{\pi\lambda L^2}{2m^2}\left(\frac{\bar{c}^2 A^2}{2} - \Delta + \vartheta_c\right) = 1, \tag{2.34}$$

where the non-dimensional displacement of the punch

$$\Delta = \frac{8\hat{\gamma}^3}{3\pi}\sum_{n=0}^{N} b_{2n}\mathcal{J}^{(1)}_{2n}(0) - \frac{8\lambda A m}{3\pi L}\mathcal{J}^{(1)}(0) + \frac{4}{3\hat{\gamma}\bar{I}(1-\nu^2)}\left(b_0 - \frac{\lambda A m \bar{c}}{\pi\hat{\gamma}^3 L}\right)\mathcal{J}^{(2)}(0), \tag{2.35}$$

and the air gap at the end of the adhesive zone is

$$\vartheta(\bar{c}) = \frac{8\hat{\gamma}^3}{3\pi}\sum_{n=0}^{N} b_{2n}\mathcal{J}^{(1)}_{2n}(\bar{c}) - \frac{8\lambda A m}{3\pi L}\mathcal{J}^{(1)}(\bar{c}) + \frac{4}{3\hat{\gamma}\bar{I}(1-\nu^2)}\left(b_0 - \frac{\lambda A m \bar{c}}{\pi\hat{\gamma}^3 L}\right)\mathcal{J}^{(2)}(\bar{c}). \tag{2.36}$$

Finally, we have $N+1$ equations from (2.32) and one each from (2.33) and (2.34), for a total of $N+3$ equations. For a given contact area A, the total number of unknowns in this problem are also $N+3$: the unknown coefficients b_{2n}, with $n = 0, \cdots, N$ in the expansion (2.24) of the contact pressure $\varphi(\bar{x})$, the displacement Δ of the punch, and the location $\bar{c}$ of the adhesive zone's edge.

The system of equations (2.32)–(2.34) are linear in b_{2n} and Δ, but *non*-linear in $\bar{c}$; cf. (2.34). Thus, an iterative procedure is followed beginning with an initial guess for $\bar{c}$. At any $\bar{c}$,

(2.32) and (2.33) are solved for b_{2n} and Δ. These b_{2n} and Δ must satisfy (2.34) at the current value of $\bar{c}$. If (2.34) is not satisfied, then the value of $\bar{c}$ is updated through a Newton-Raphson root finding algorithm; see, e.g. Chatterjee (2002). We continue to iterate until a consistent set of b_{2n}, Δ and $\bar{c}$ is found. Care should be taken while finding the adhesive zone size $\bar{c}$, as it depends sensitively on the initial guess, and on the root finding algorithm that is employed. Once b_{2n}, Δ and $\bar{c}$ are found, the contact pressure $\varphi(\bar{x})$ and the total load $\bar{P}$ may be obtained from (2.24) and (2.28), respectively.

2.5 Finite element simulations

For comparison later, we will also solve the non-adhesive ('Hertzian') contact of a rigid punch with a beam through the finite element (FE) method. We employ the commercial FE package ABAQUS. While ABAQUS does provide some cohesive zone models that may be employed to simulate adhesive contact, they are not easily compared with the Dugdale-Barenblatt model that we employ. Thus, we restrict comparisons with FE results to non-adhesive contact. We also limit FE simulations to clamped and simply supported beams.

In our FE simulations, the beam is modeled as a linear elastic layer with Young's modulus $E = 2000$ MPa and Poisson's ratio $\nu = 0.3$. The beam's thickness and half-span are taken as $h = 4$ mm and $l = 40$ mm, respectively. We note that these material properties are not typical of beams employed in structural adhesives, for example by Arul and Ghatak (2008). However, these properties are selected as their magnitudes allow us to easily distinguish the effect of external inputs to the punch.

The cylindrical punch has radius $R = 225$ mm and Young's modulus $E_p = 2 \times 10^6$ MPa - a thousand times the Young's modulus of the beam. A high E_p is chosen in order to approximate a rigid punch.

In our FE analysis, plane-strain elements are considered for both the beam and the punch. For more details we refer the reader to Appendix E. The load is applied on the punch. The remaining contact parameters, i.e. contact pressure, contact area, and the displacement of the punch, are obtained after post-processing the computation's output. These parameters are now compared with the semi-analytical results of Sec. 2.4.

2.6 Results: Non-adhesive ('Hertzian') contact

We first investigate the adhesionless contact of a rigid punch with elastic beams. We will consider beams that are clamped, simply supported, or rest on flexible supports. Some results will be compared with FE simulations of Sec. 2.5.

Equations for the indentation of a non-adhesive beam are obtained by setting $\lambda = 0$ in (2.32):

$$\sum_{n=0}^{N} a_{2n}\mathcal{J}_{nm} = \frac{8\hat{\gamma}^3}{3\pi}\sum_{n=0}^{N} b_{2n}\mathcal{J}_{nm}^{(1)} + \frac{4b_0}{3\hat{\gamma}\bar{I}\,(1-\nu^2)}\mathcal{J}_m^{(2)} \quad \text{for } m = 0, \cdots, N. \tag{2.37}$$

The contact pressure vanishes at the edge $\bar{x} = \pm 1$ of the contact zone, so that (2.33) holds. The energy condition (2.34) is now redundant. The $N+2$ equations that comprise (2.33) and (2.37) are to be solved for the $N+2$ unknowns b_{2n} $(n = 0, \cdots, N)$ and Δ for a given choice of A. The contact pressure distribution and the total load are then found from (2.24) and (2.28), respectively, after setting $\lambda = 0$.

Computations are carried out with $N = 5$, i.e. the expansion (2.24) is truncated at the Chebyshev polynomial T_{10}.

2.6.1 Clamped beam

A clamped beam is obtained in the limit of $k_s^f,\, k_t^f \to \infty$. Thus, $\bar{\vartheta}_p\,(\hat{\omega})$ is given by (A.15), which then enters into the computation of $\mathcal{J}_m^{(2)}$ in (2.37). The unknown contact pressure distribution $\varphi\,(\bar{x})$ is obtained by solving (2.37) and (2.33).

We compare the results of our semi-analytical procedure of Sec. 2.4 with FE simulations in Fig. 2.3 and with the results of Keer and Miller (1983) in Fig. 2.4. We observe from Figs. 2.3 and 2.4 that, when the ratio a/h of the contact area to the beam's thickness is low, the maximum contact pressure is obtained at the center of the contact region. We also find from Fig. 2.4 that at low a/h ratios the pressure profiles are similar to the pressure distribution obtained for indentation into an elastic half-space. Increasing the a/h ratio – which, for a given beam (fixed h and l) corresponds to increasing the load, as the contact area increases – causes the pressure at the center of the contact region to decrease, but increase near its ends; thus, the pressure profiles acquire a double-humped character. Our semi-analytical results are in good agreement with those of FE simulations,

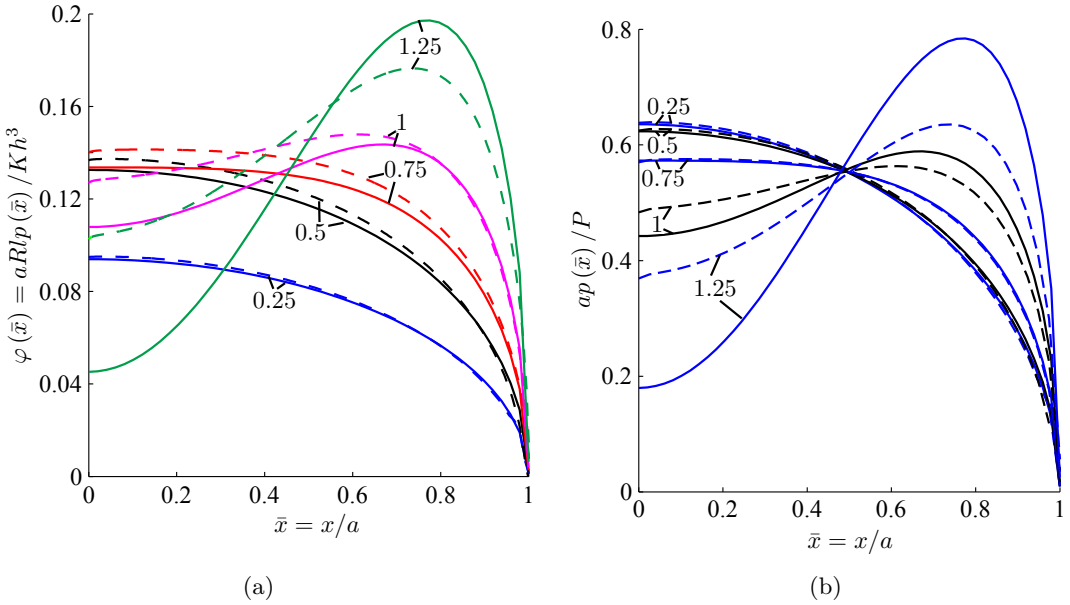

Figure 2.3: Non-adhesive contact of a clamped beam. Non-dimensional contact pressures (a) $\varphi(\bar{x})$ and (b) $ap(\bar{x})/P$ are shown. The beam's slenderness ratio $l/h = 10$. Several contact areas a are investigated by varying a/h, which are noted next to their associated curves. Solid lines are results obtained from the semi-analytical procedure of Sec. 2.4. Dashed lines correspond to FE simulations of Sec. 2.5.

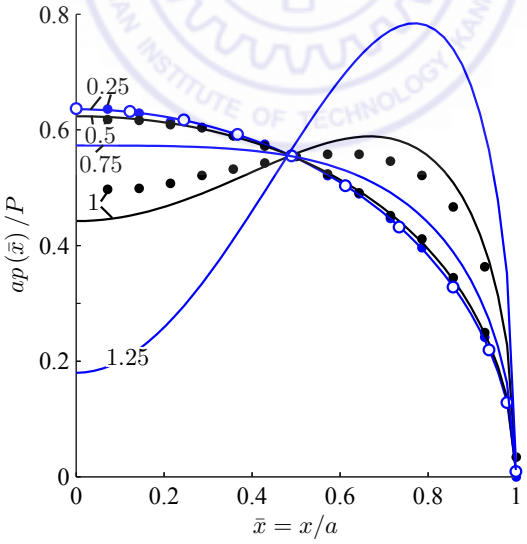

Figure 2.4: Non-adhesive contact of a clamped beam. Non-dimensional contact pressure $ap(\bar{x})/P$ is shown. The beam's slenderness ratio $l/h = 10$. Several contact areas a are investigated by varying a/h, which are noted next to their corresponding curves. Solid lines are results obtained from the semi-analytical procedure of Sec. 2.4. Open-circles represent the solution for an elastic half-space. Results of Keer and Miller (1983), when available, are shown by filled circles.

and the theoretical results of Keer and Miller (1983) for $a/h \lessapprox 1$; see Figs. 2.3 and 2.4, respectively. For $a/h > 1$, our assumption that the displacement of the beam's bottom surface may be approximated through Euler-Bernoulli beam theory breaks down. This causes the semi-analytical results to deviate from those of FE computations in Fig. 2.3.

We have followed Keer and Miller (1983) in plotting $ap\left(\bar{x}\right)/P$ along the vertical axis in Figs. 2.3(b) and 2.4. A match employing this scale may not guarantee a correspondence of the actual pressure profiles $\varphi\left(\bar{x}\right)$ or $p\left(\bar{x}\right)$. This is because the total load P in the denominator of $ap\left(\bar{x}\right)/P$ is calculated by integrating $\varphi\left(\bar{x}\right)$ in the numerator. Thus, even if a constant factor is missed in $p\left(\bar{x}\right)$, the ratio $ap\left(\bar{x}\right)/P$ will remain unaffected. Given this, the comparison of pressure profiles shown in Fig. 2.3(a) is more illuminating. Finally, the pressure profiles in Figs. 2.3(b) and 2.4 do not vary much with the slenderness ratio l/h. These plots may therefore be utilized to estimate pressures at other l/h as well.

Next, the variation of the contact area A with the total load $\bar{P}$ and with the displacement Δ of the punch are shown in Fig. 2.5. Results of both clamped and simply supported

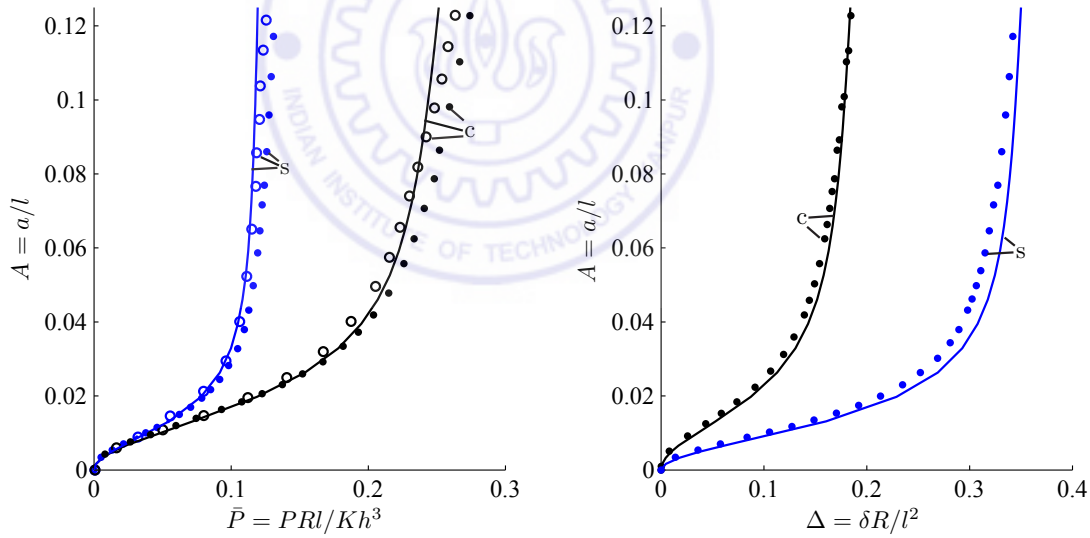

Figure 2.5: Non-adhesive contact of clamped ('c') and simply supported ('s') beams. The contact area A is plotted as a function of (a) the total load $\bar{P}$ acting on the punch and (b) the punch's displacement Δ. The beam's slenderness ratio l/h=10. Solid lines are results obtained from the semi-analytical procedure of Sec. 2.4. Filled circles correspond to FE simulations of Sec. 2.5. Predictions of Sankar and Sun (1983) are shown by open circles, when available.

beams (discussed in the next section) are shown. From Fig. 2.5(a) we find that to obtain the same contact area A, a clamped beam requires higher load compared to the simply

supported beam. Similarly, Fig. 2.5(b) shows that, at a given A, a clamped beam displaces less than a simply supported beam. Both these outcomes are expected, as the bending stiffness of the clamped beam is higher than that of a simply supported beam. Thus, the contribution to vertical displacement Δ from the beam's bending is lowered in the case of a clamped beam. Similarly, a clamped beam wraps less about the punch, thereby lowering the contact area at given load. The clamped beam's greater bending stiffness compared to that of a simply supported beam is clearly demonstrated by Fig. 2.6 that plots the deflection of the beam's center point – which equals the punch's displacement Δ – against the total load $\bar{P}$. The linear response of Δ with $\bar{P}$ is not unexpected as the displacement of the beam's bottom surface is obtained from beam theory. From Figs. 2.5 and 2.6 it is evident that end supports have significant bearing on the beam's indentation. Finally, in Figs. 2.5 and 2.6, we again find a good match both with FE simulations and with the results of Sankar and Sun (1983).

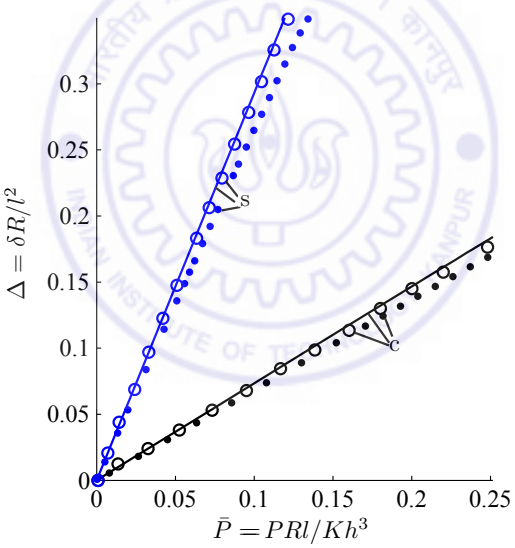

Figure 2.6: Non-adhesive contact of clamped ('c') and simply supported ('s') beams. The displacement Δ of the punch is shown as a function of the total load $\bar{P}$. See also the caption of Fig. 2.5.

As mentioned in Sec. 2.5, the material parameters employed in FE simulations may not be relevant for typical applications. Thus, in Figs. 2.7 and 2.8 we report results with parameters more commonly encountered. Following Dalmeya et al. (2012), the Young's modulus and Poisson's ratio of the beam are taken corresponding to those observed in soft materials: $E = 0.083$ MPa and $\nu = 0.4$, respectively. The beam's geometry remains the same as before. The contact pressure profiles, employing these material parameters, for

different thick beams, and how they approach those of an elastic half-space, are presented in Appendix F; cf. Fig. F.1(a).

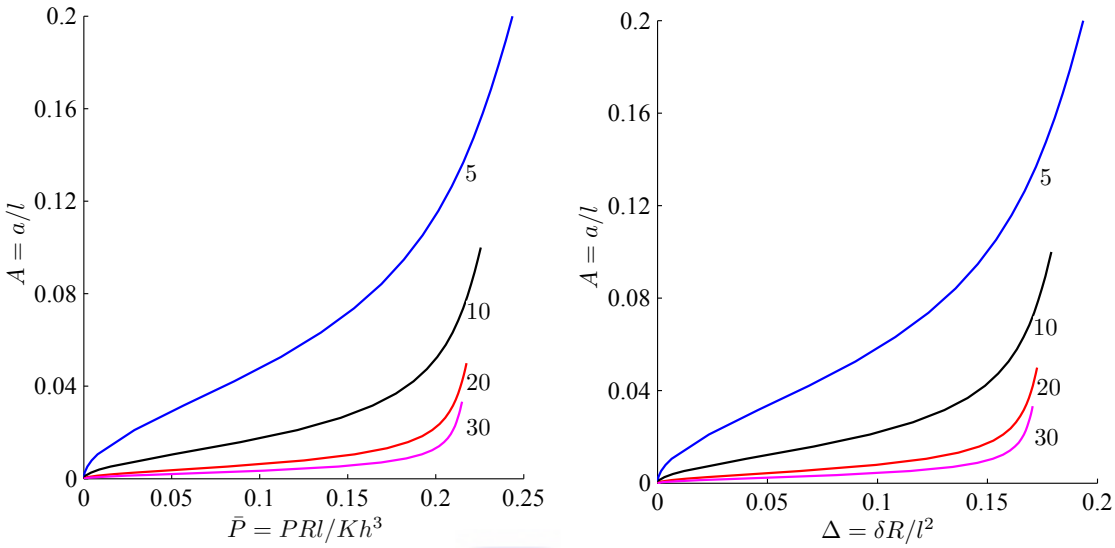

Figure 2.7: Non-adhesive contact of clamped beams. Variation of contact area A with (a) total load $\bar{P}$ and (b) punch's displacement Δ is shown. Different slenderness ratios l/h are considered and these are noted next to their associated curves.

The contact area A is plotted against the total load acting on the punch $\bar{P}$ and the displacement Δ of the punch in Fig. 2.7 for clamped beams of different slenderness ratios l/h. A more slender beam is less resistant to bending. Thus, beams with higher l/h require less load P compared to lower l/h to achieve the same contact area a. But, the curves in A versus $\bar{P}$ plot, i.e. Fig. 2.7(a), does not show this, as these non-dimensional terms are expressed using the beam's geometric parameters, i.e. l and h. To observe this phenomenon more clearly we refer the reader to Appendix G, where we plot the variation of contact area with the variation in total load and punch displacement employing new non-dimensional parameters that are free from both l and h. Similarly, the punch's displacement Δ is high for more slender beams. However, the curves in Fig. 2.7(b) show this phenomenon correctly, by shifting downward with growing l/h, Appendix G explains this phenomenon more accurately. We also demonstrate, by varying thickness of beams, how our predications approach those of an elastic half-space in Appendix F; see Figs. F.2(a) and (b).

Finally, in Fig. 2.8 we plot variation of the displacement Δ of the punch with the total load $\bar{P}$ for different l/h ratios. We observe that, our choice of non-dimensionalization (cf.

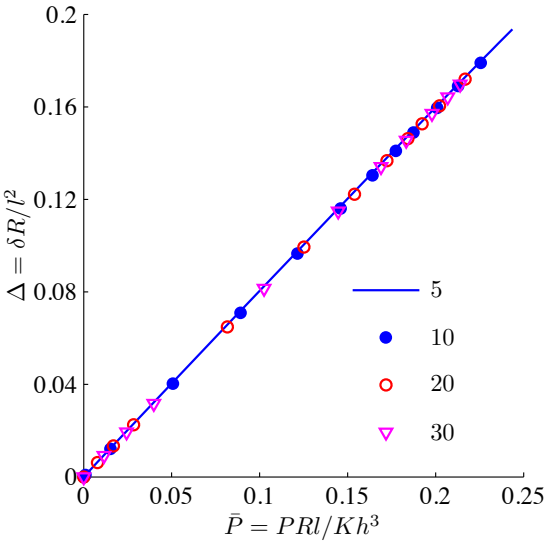

Figure 2.8: Non-adhesive contact of clamped beams. Variation of punch's displacement Δ with total load $\bar{P}$ is shown. Different slenderness ratios l/h are considered as noted in the legend.

Sec. 2.3) for the punch's displacement and the total load allows the curves in Fig. 2.8 to collapse onto a single line. This is not seen for other scalings, cf. Secs. 2.7 and 2.8, where we report results for adhesive contact.

2.6.2 Effect of end conditions

We obtain results for a simply supported beam in the limit $k_s^f \to \infty$ and $k_t^f \to 0$. The vertical displacement of the bottom surface is given by (A.16). The contact pressure $\varphi(\bar{x})$ is then found by solving (2.37) and (2.33), and invoking (2.24). The behavior of a simply supported beam is qualitatively similar to that of a clamped beam, but differs quantitatively.

Figure 2.9 repeats Figs. 2.3 and 2.4 for simply supported beams and compare our semi-analytical results with those of FE simulations, and Keer and Miller (1983). As before, we find good agreement between all three approaches for $a/h \lessapprox 1$.

Contrasting Figs. 2.3(a) and 2.9(a) we find that, at the same a/h, pressures found in a simply supported beam are lower compared to those in a clamped beam. Thus, the total load $\bar{P}$ required to achieve the same contact area, for clamped and simply supported beams of the same thickness, is very different. This reinforces the importance of correctly modeling end supports in beam indentation. Interestingly, because of the manner in which

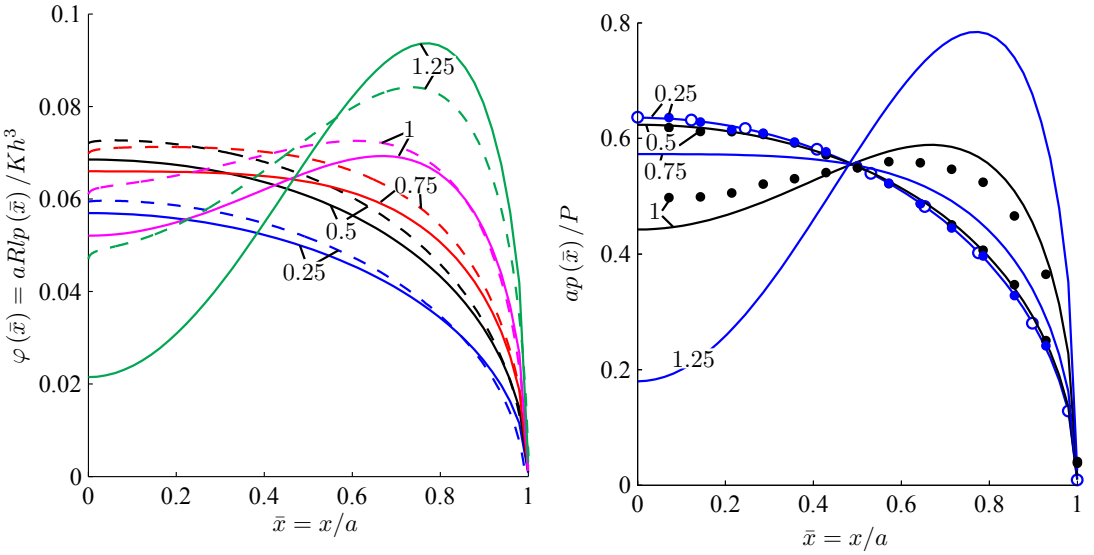

Figure 2.9: Non-adhesive contact of a simply supported beam. Non-dimensional contact pressure (a) $\varphi(\bar{x})$ and (b) $ap(\bar{x})/P$ are shown. Several contact areas are investigated by varying a/h as noted next to the associated curves, while keeping $l/h = 10$. Solid lines are results obtained from the semi-analytical procedure of Sec. 2.4. Dashed lines in (a) correspond to FE simulations of Sec. 2.5. Open circles in (b) represent the solution for an elastic half-space. Results of Keer and Miller (1983), when available, are shown in (b) by filled circles.

the contact pressure is scaled, Figs. 2.4 and 2.9(b) are nearly the same.

Finally, we report results on the non-adhesive contact of beams resting on flexible supports with parameters utilized to generate Figs. 2.7 and 2.8. Again, for beams with slenderness ratio $l/h = 10$, the contact area A is plotted against the total load $\bar{P}$ acting on the punch and the punch's displacement Δ in Figs. 2.10 and 2.11. Figure 2.10 shows results for several torsional spring stiffnesses k_t^f after setting the vertical translational spring's stiffness k_s^f to infinity. Such a beam may be thought of as a simply supported beam with some resistance to rotation at the ends, or a beam whose clamped ends allow some rotational play. Results lie between those obtained for clamped and simply supported beams. Expectedly, increasing k_t^f shifts the results towards those of a clamped beam, and decreasing it yields results close to those of a simply supported beam. This is seen clearly in Fig. 2.10.

Figure 2.11 repeats Fig. 2.10, but this time keeping k_t^f as infinity and varying k_s^f. We find that increasing k_s^f does *not* affect the variation of A with $\bar{P}$, but the dependence of A on Δ changes; see the inset in Fig. 2.11(b). The latter change is, however, due to

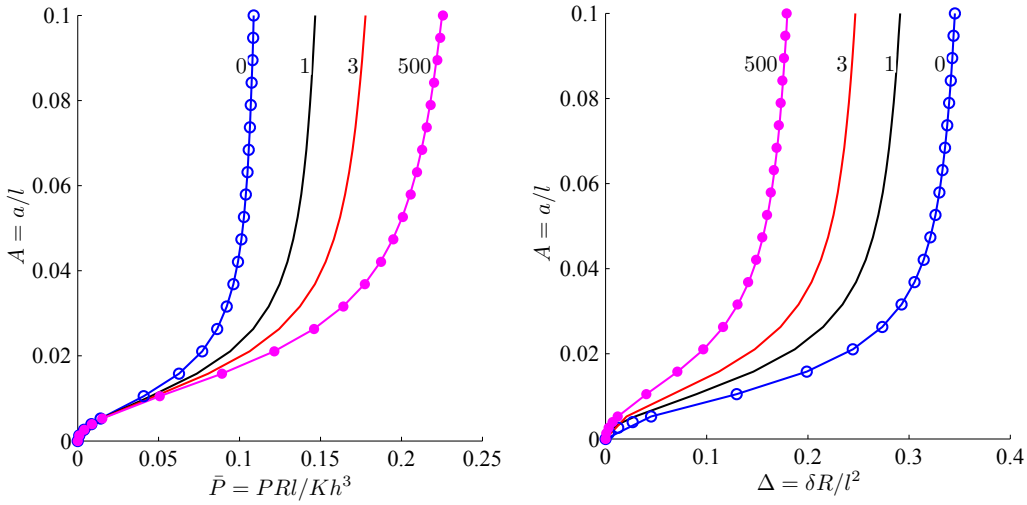

Figure 2.10: Non adhesive contact of beams on flexible supports. The contact area A is plotted as a function of (a) the total load $\bar{P}$ acting on the punch and (b) the punch's displacement Δ. The beam's slenderness ratio $l/h = 10$. The vertical translational spring's stiffness $k_s^f = \infty$. Various torsional springs are considered and their stiffnesses k_t^f are indicated next to their associated curves. Open and filled circles represent results for simply supported and a clamped beams, respectively.

the vertical displacement Δ_l of the beam's spring supports. The presence of Δ_l shifts the datum downwards, so that indentation now initiates from $y = \Delta_l$, rather than from $y = 0$. Once we correct for Δ_l we find that displacement plots in the inset of Fig. 2.11(b) are also unaffected by variation in k_s^f, as shown in Fig. 2.11(b).

2.7 Results: Adhesive contact - JKR approximation

We now consider adhesive contact of beams after invoking the JKR approximation, previously discussed in Secs. 2.2 and 2.3. Thus, we need to solve the integral equation (2.23) along with energy balance (2.21), in the limit of adhesive strength dominating elastic stiffness, i.e. $\lambda \to \infty$, while the adhesive zone becomes infinitesimally small, so that $\bar{c} \to 1$. Employing expansion (2.24) for the contact pressure, (2.23) and (2.21) become, respectively,

$$\sum_{n=0}^{N} a_{2n}\mathcal{J}_{nm} = \frac{8\hat{\gamma}^3}{3\pi}\sum_{n=0}^{N} b_{2n}\mathcal{J}_{nm}^{(1)} + \frac{4b_0}{3\hat{\gamma}\bar{I}\,(1-\nu^2)}\mathcal{J}_m^{(2)} \quad \text{for } m = 0, \cdots, N \tag{2.38}$$

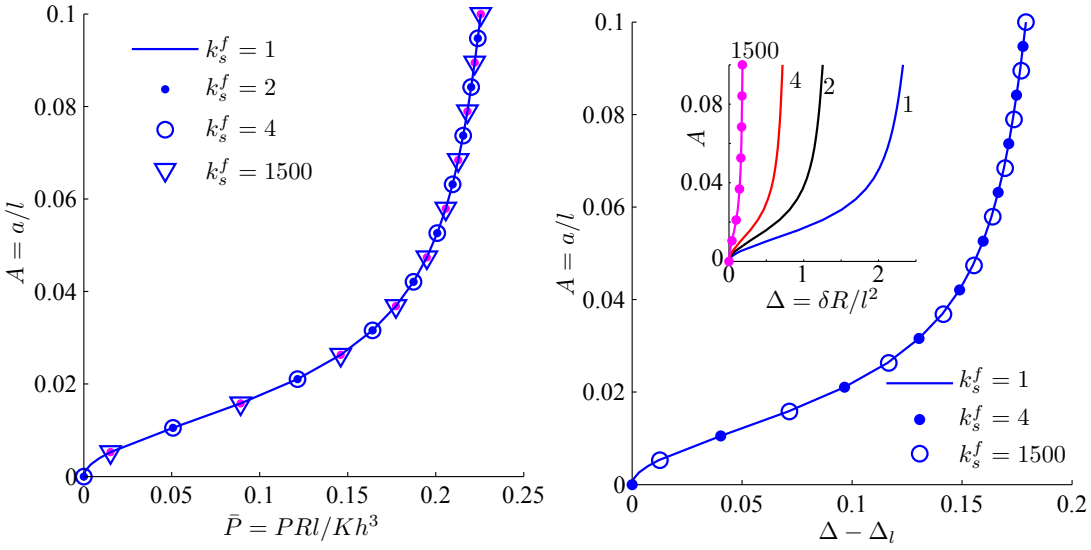

(a) (b)

Figure 2.11: Non-adhesive contact of beams on flexible supports. The contact area A is plotted as a function of (a) the total load $\bar{P}$ acting on the punch and (b) the adjusted punch displacement $\Delta - \Delta_l$. The inset in (b) shows the variation of the contact area A with the punch's displacement Δ. The beam's slenderness ratio $l/h = 10$. The torsional spring stiffness $k_t^f = \infty$. Various vertical translational springs are considered and their stiffnesses k_s^f are indicated either in the legend or next to their associated curves. Filled circles in the inset in (b) represent results for a clamped beam.

and

$$b_0 + b_2 + \cdots + b_{2N} = -\frac{m}{2\pi L}\left(\frac{l}{h}\right)^3 \sqrt{\frac{6Am}{L}}. \tag{2.39}$$

From here on, we follow Maugis (1992) and employ

$$\hat{A} = \frac{AL}{m} = a\left(\frac{K}{\pi w R^2}\right)^{1/3}, \quad \hat{P} = \frac{\bar{P}H^3}{Lm^3} = \frac{P}{\pi w} \quad \text{and} \quad \hat{\Delta} = \frac{\Delta L^2}{m^2} = \delta\left(\frac{K^2}{\pi^2 w^2 R}\right)^{1/3}, \tag{2.40}$$

where $H = h/R$, instead of, respectively, A, P, and Δ, to report our results. This is done in order to facilitate contact with other work on adhesion. We set the adhesion energy $w = 0.02 \times 10^{-3}$ J/mm^2.

Figure 2.12 plots the variation of the contact area $\hat{A}$ with the total load $\hat{P}$ acting on the punch and with punch's displacement $\hat{\Delta}$ for clamped beams. While the slenderness ratio $l/h = 10$, two different combinations of l and h are considered. From Fig. 2.12 we observe that the variation of $\hat{A}$ with $\hat{P}$ and $\hat{\Delta}$ is sensitive to the choice of l and h, notwithstanding the fact that l/h is kept constant. This is in contrast to the case of non-adhesive contact of Sec. 2.6, where results depended only on l/h. However, this behavior is expected for

adhesive beams as the right hand side of (2.39) depends on $L = l/R$. This aspect is further exemplified in Fig. 2.13, which plots $\hat{A}$ against $\hat{P}$ and $\hat{\Delta}$ for clamped beams for different choices of l and h.

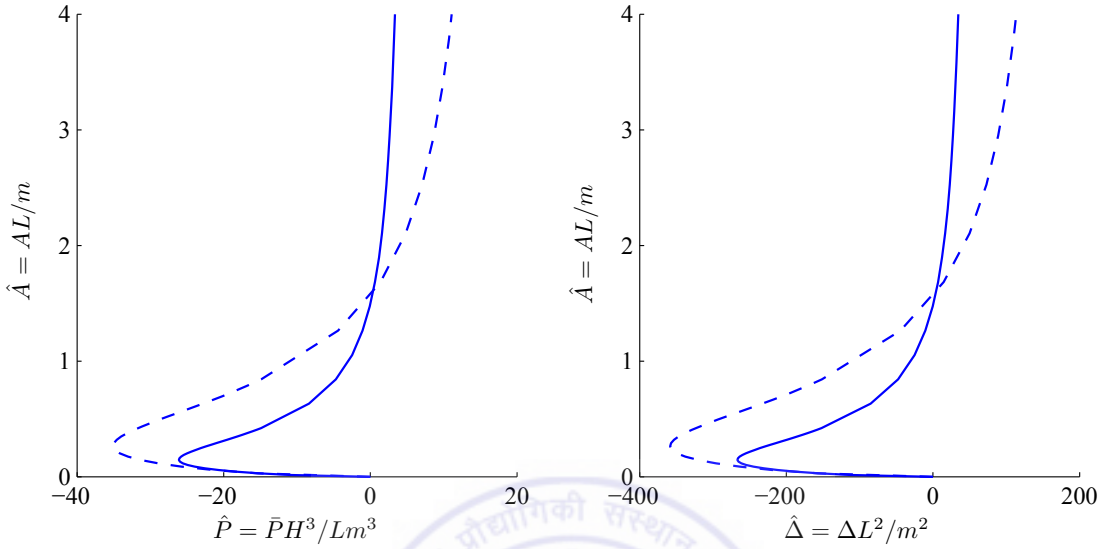

Figure 2.12: Adhesive contact of clamped beams with the JKR approximation. Variation of contact area $\hat{A}$ with the (a) total load $\hat{P}$ and (b) the punch's displacement $\hat{\Delta}$. The beam's slenderness ratio $l/h = 10$. Solid lines correspond to $l = 40$ mm and $h = 4$ mm, while the dashed line is for a beam with $l = 80$ mm and $h = 8$ mm.

In Figs. 2.12 and 2.13, negative values of $\hat{P}$ and $\hat{\Delta}$ reflect tensile loads and upward displacement of the punch, respectively. We recall that $\hat{\Delta}$ equals the deflection of the center point on the beam's top surface, so that $\hat{\Delta} < 0$ indicates that the beam bends upwards. Negative values of $\hat{P}$ and $\hat{\Delta}$ are due to the attractive adhesive forces. Due to adhesion, the beam bends upwards and jumps into contact. Equivalently, adhesive forces also act on the punch to pull it down, so that we require a tensile force to hold the punch in it's place. This tensile force $\hat{P}$ is small for slender beams as they bend easily. For the same reason, this tensile force is smaller for a simply supported beam compared to a clamped beam of same slenderness ratio; cf. Fig. 2.14. Once contact is established, the tensile force is slowly released and replaced by a compressive (downwards) force in order to increase downward indentation. Again, for compressive loads, slender beams bend more easily to wrap around the punch. Thus, slender beams show greater contact area and displacement at the same compressive load $\hat{P}$. This explains the intersection of the curves in Fig. 2.13. Therefore, with increasing slenderness ratio, the $\hat{A}$–$\hat{P}$ curves in the left column of Fig. 2.13

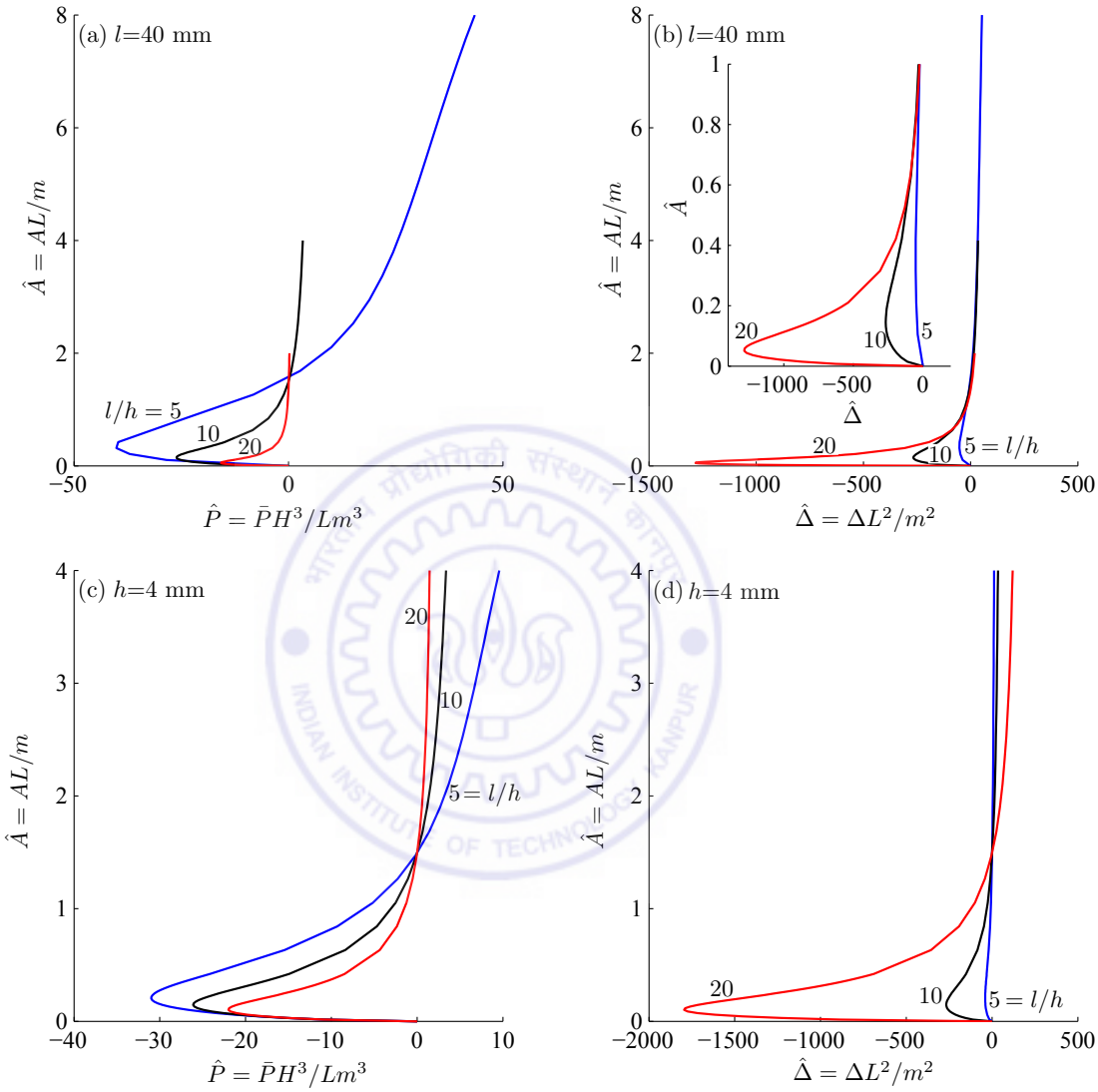

Figure 2.13: Adhesive contact of clamped beams with the JKR approximation. Left column reports the variation of contact area $\hat{A}$ with total load $\hat{P}$, while the right column plots the change of $\hat{A}$ with the punch's displacement $\hat{\Delta}$. Results in the top row are obtained by setting $l = 40$ mm and varying h as shown, while those in the bottom row have $h = 4$ mm but different l, as indicated. The inset in (b) illustrates behavior at low $\hat{A}$.

move towards (inwards) the zero-load ($\hat{P} = 0$) vertical line, and $\hat{A}$–$\hat{\Delta}$ curves in the right column of Fig. 2.13 move away (outwards) from the $\hat{\Delta} = 0$ line.

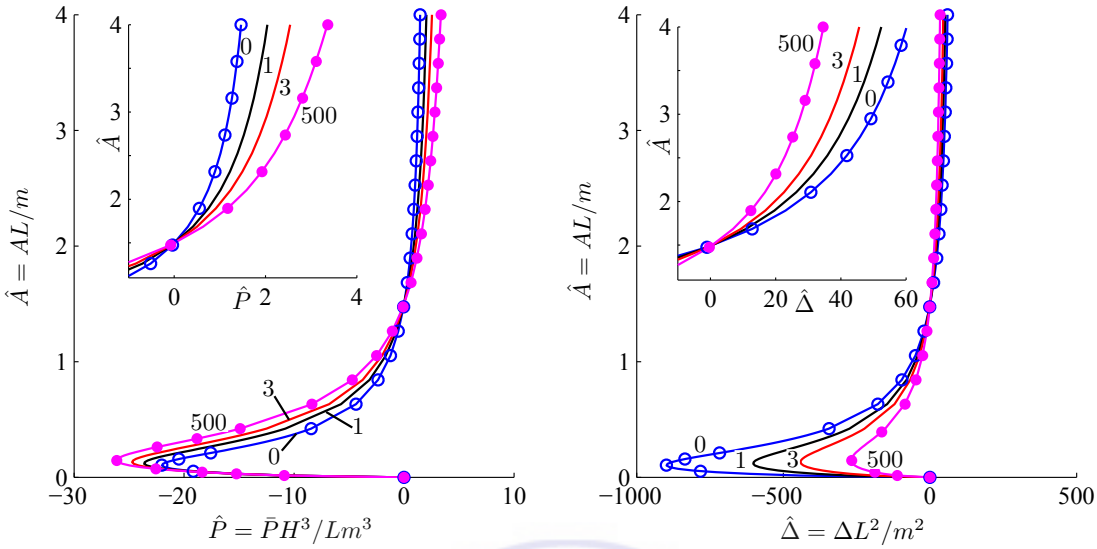

(a) (b)

Figure 2.14: Adhesive contact of beam on flexible supports with the JKR approximation. The contact area $\hat{A}$ is plotted as a function of (a) the total load $\hat{P}$ acting on the punch and (b) the punch's displacement $\hat{\Delta}$. The beam's thickness $h = 4$ mm and $l = 40$ mm. The vertical translational spring's stiffness $k_s^f = \infty$. Various torsional springs are considered and their stiffnesses k_t^f are indicated next to their associated curves. The insets correspond to behavior at high $\hat{A}$. Open and filled circles represent results for adhesive beams that are, respectively, simply supported and clamped.

Finally, for adhesive beams on flexible supports we plot the contact area $\hat{A}$ against the load $\hat{P}$ and displacement $\hat{\Delta}$ for various k_t^f in Fig. 2.14. Convergence to the results obtained for clamped and simply supported beams may be observed in Fig. 2.14 by varying k_t^f. From our discussion in Sec. 2.6.2, we know that the variation of k_s^f does not affect how the contact area $\hat{A}$ varies with the load $\hat{P}$. At the same time, change in $\hat{A}$ with the displacement $\hat{\Delta}$ is affected by variation in k_s^f only through the vertical displacement of the translational springs supporting the beam at its ends. By removing this global displacement $\hat{\Delta}_l$ from $\hat{\Delta}$ – as in Sec. 2.6.2 – the response of $\hat{A}$ to $\hat{\Delta}$-$\hat{\Delta}_l$ is found to be invariant to k_s^f.

2.8 Results: Adhesive contact with an adhesive zone model

We finally consider contact with an adhesive beam within the framework of adhesive zone models. As already mentioned, we will assume that an adhesive zone of length $d = c - a$ extends outside the contact zone; cf. Fig. 2.2(b). Within the adhesive zone the interaction

is modeled through the Dugdale-Barenblatt model of (2.7). To obtain the contact pressure $\varphi(\bar{x})$, the displacement Δ and the location c of the adhesive zone's edge, we have to solve (2.32)–(2.34).

For the clamped beam we plot in Fig. 2.15 the contact area $\hat{A}$ against the total load $\hat{P}$ and displacement $\hat{\Delta}$ for various adhesive strengths λ. With increase in λ, the solutions approach the JKR solution, and we see a close match at $\lambda = 3$. On the other hand, as $\lambda \to 0$, i.e. as adhesion reduces, solutions approach those obtained for non-adhesive contact in Sec. 2.6.

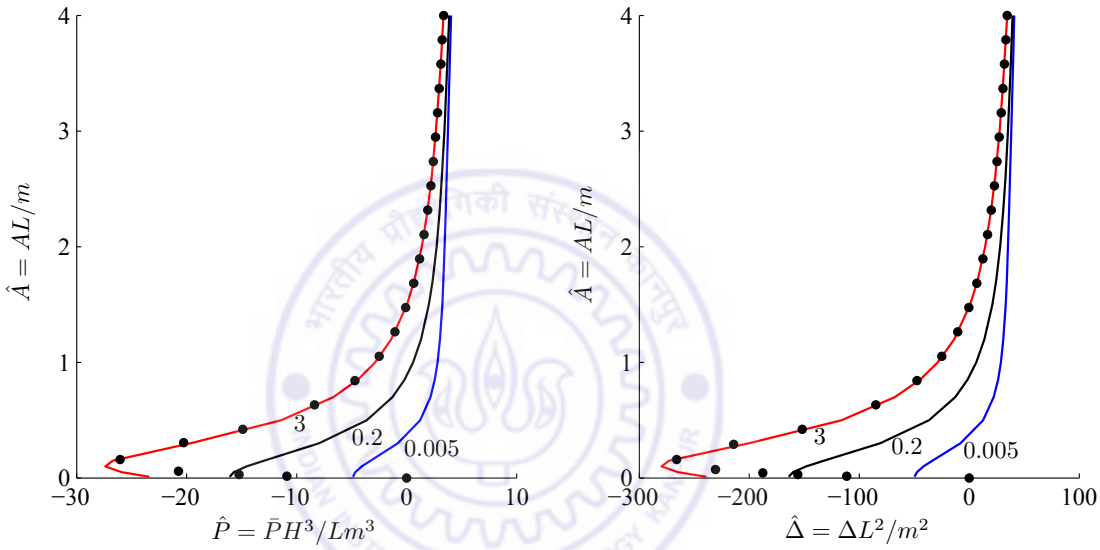

Figure 2.15: Adhesive contact of clamped beams with an adhesive zone model. Variation of contact area $\hat{A}$ with (a) the total load $\hat{P}$ and (b) the punch's displacement $\hat{\Delta}$. Different adhesive strengths λ are considered and these are indicated next to their associated curves. The beam's thickness $h = 4$ mm and $l = 40$ mm. Filled circles represent the JKR solution for the corresponding beam; cf. Sec. 2.7

From previous discussions, it is expected that results for beams with flexible supports will lie between those obtained for clamped and simply supported beams. Hence, we do not explore this parameter space in great detail. We only consider the variation of $\hat{P}$ and $\hat{\Delta}$ with $\hat{A}$ for several values of torsional stiffness k_t^f for a beam with $h = 4$ mm and $l = 40$ mm. Two different adhesive strengths λ are investigated. The results are shown in Fig. 2.16. The vertical translational spring's stiffness k_s^f is set to infinity. When $k_t^f = 0$, the solutions match with those of a simply supported beam with the corresponding λ. With increase in k_t^f, the solution curves move towards those obtained for a clamped beam and will coincide

when k_t^f becomes infinity. It is seen in Fig. 2.16 that curves for different k_t^f intersect with each other due to rotation permitted at the supports by the torsional springs – greater the rotation allowed, higher the displacements, and lower the loads for the same contact area. This intersection point moves up with increasing λ, as strong adhesive forces are able to bend the beam upwards more easily.

Finally, in Fig. 2.17 we plot the variation of the non-dimensional adhesive zone size $\bar{d} = \bar{c} - 1$ with the contact area $\hat{A}$ for different adhesive strengths λ and various k_t^f. We observe that the adhesive zone size is large for smaller λ, and decreases with increasing λ, finally vanishing as $\lambda \to \infty$. Moreover, we find that the adhesive zone's size does not vary much with the slenderness ratio l/h, and spring stiffnesses k_s^f and k_t^f.

2.9 Experiments and Applications

In this final section, we present preliminary experimental results on a clamped beam, as well as apply our methods to model structural adhesives of the type shown in Fig. 2.1(a).

2.9.1 Experiments

We have experimentally investigated the indentation of a clamped PDMS (poly-dimethyl-siloxane) beam by a cylindrical glass punch. To make PMDS samples, a uniform mixture of Sylgard 184 silicone elastomer base and curing agent is prepared by taking them in 10:1 weight ratio. Air is desiccated from this mixture, which is then poured into a rectangular mould of desired size. This is cured at room temperature ($\approx 17^o$C) for two days and the PDMS sample is extracted from the mould.

First, micro-tensile tests are carried out on the PDMS samples to measure their Young's modulus E. This is found to be in the range of 1 – 2 MPa. Next, standard JKR indentation Chaudhury et al. (1996) tests are carried out. In these tests, PDMS samples of thickness $h \approx 25$ mm are rigidly attached to the micro-positioner, and a cylindrical glass punch of radius $R \approx 27.5$ mm is placed on top of the semi-micro balance; see Fig. 2.18(a). The PDMS samples are brought into contact with the glass punch employing the micro-positoner. The rectangular contact patch thus formed, shown in the upper inset of Fig. 2.18(a), is observed through a microscope, and the load acting on the punch is

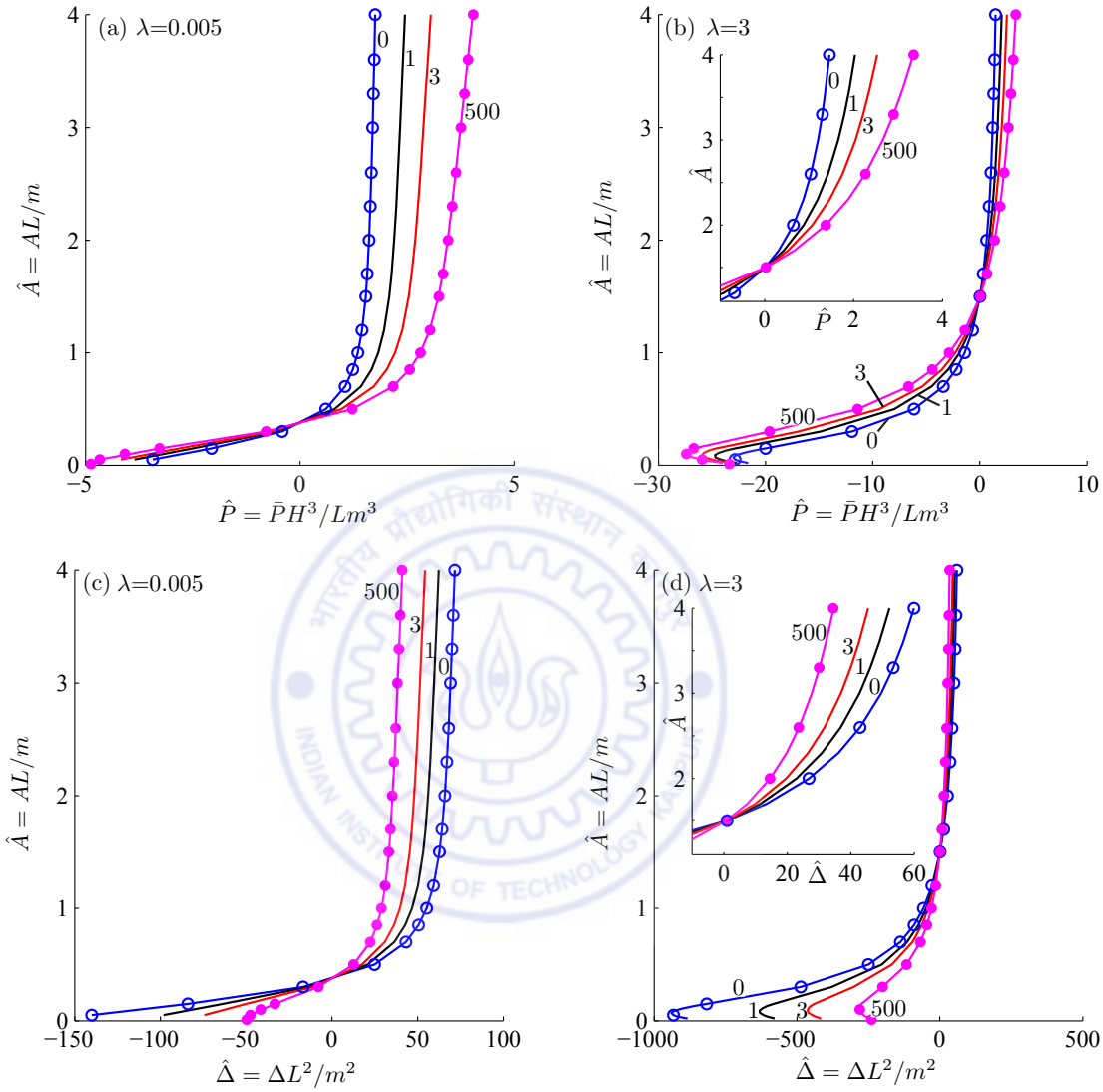

Figure 2.16: Adhesive contact of beams on flexible supports with an adhesive zone model. Top row reports the variation of contact area $\hat{A}$ with total load $\hat{P}$, while the bottom row plots the change of $\hat{A}$ with the punch's displacement $\hat{\Delta}$. Different torsional spring stiffnesses k_t^f are considered, and they are noted next to their associated curves. Two different adhesive strengths λ are considered, as indicated. The beam's thickness $h = 4$ mm and half-span $l = 40$ mm. The insets in (b) and (d) depict behavior at high $\hat{A}$. Open and filled circles represent results for a simply supported and a clamped beam, respectively, at the corresponding λ.

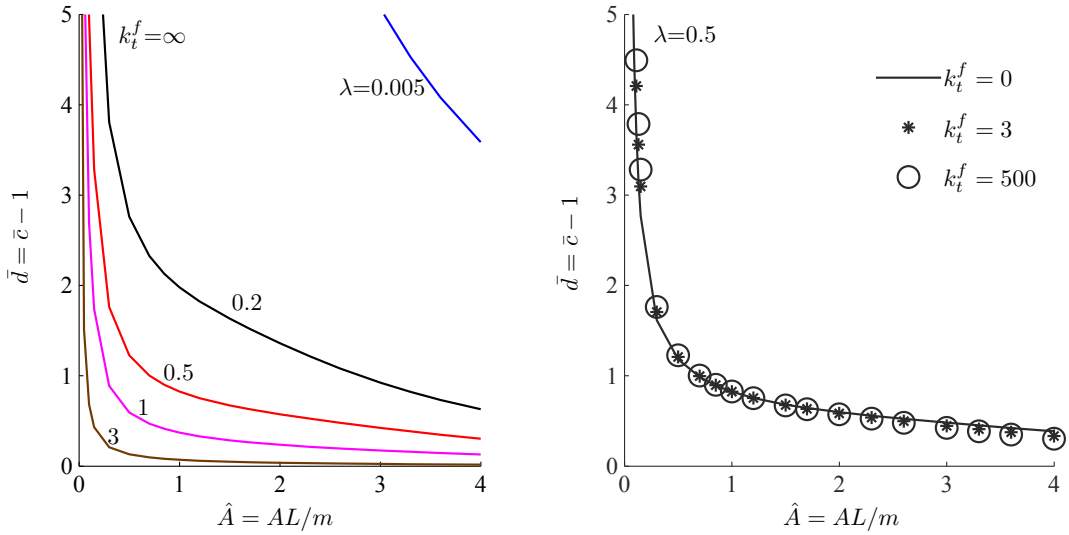

Figure 2.17: Adhesive contact of beams on flexible supports with an adhesive zone model. Variation of the adhesive zone's size $\bar{d}$ with the contact area $\hat{A}$ for (a) different adhesive strengths λ, with $k_t^f = \infty$ and $k_s^f = \infty$, and (b) three different torsional spring stiffnesses k_t^f at $\lambda = 0.5$.

noted from the semi-micro balance. The Young's modulus E and the work of adhesion w are then found following Chaudhury et al. (1996); see Appendix H. The JKR experiments confirm the range for E found from micro-tensile tests, and find the work of adhesion $w \approx 27$ mJ/mm^2. The values of E and w compare well with those reported earlier by Johnston et al. (2014), and Arul and Ghatak (2008).

Finally, contact mechanics experiments are carried out on a clamped PDMS beam. In these experiments, the beam's half-span and thickness are maintained at $l \approx 50$ mm and $h \approx 8$ mm, respectively. The total load P and contact patch width $2a$ are measured. The results obtained are then compared with the predictions of our semi-analytical approach in Fig. 2.18(b). We find good agreement. We observe that the results for a beam vary considerably from that of a half-space lending support for the necessity of the theoretical development presented in this chapter.

More thorough experiments, where we vary parameters like flexibility of end supports, beam thickness h, the work of adhesion w, etc. are under progress.

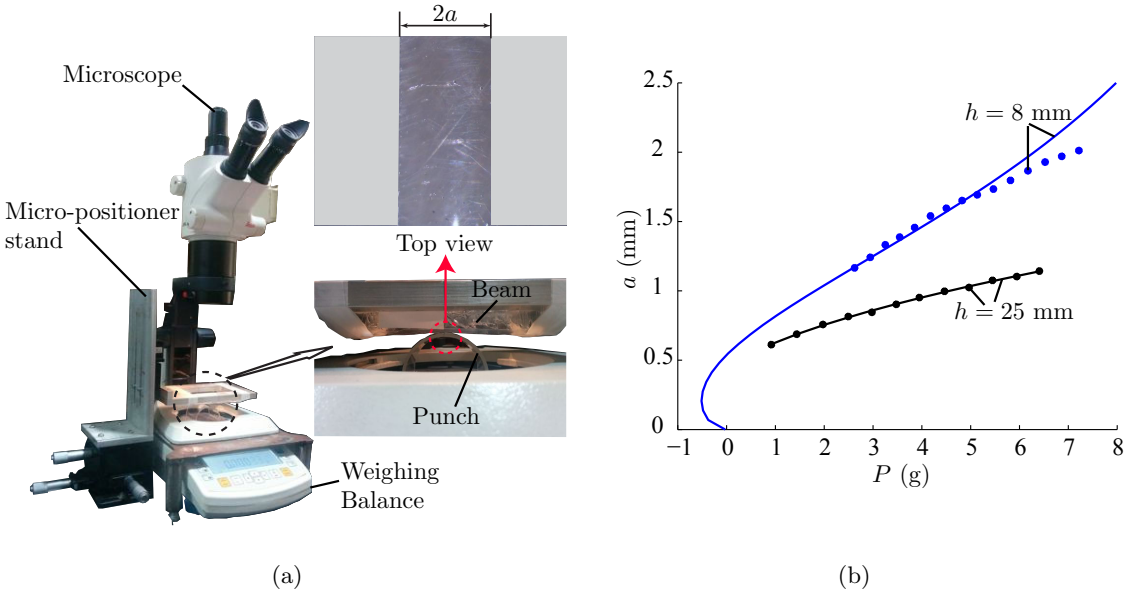

(a) (b)

Figure 2.18: (a) Indentation experiments for an adhesive clamped beam of thickness $h = 8$ mm and half-span $l = 50$ mm. Insets show a closeup of the side view of the indentation and a top view of the contact patch. (b) Variation of the contact area a (in mm) with the total load P (in g). Filled circles represent experimental data. Solid lines correspond to theoretical predictions. For $h = 8$ mm, we followed Sec. 2.7, while $h = 25$ mm, we employed the standard JKR solution for a half-space Chaudhury et al. (1996).

2.9.2 Application

We now demonstrate the application of our semi-analytical procedure to the indentation of structural adhesives with one micro-channel, as shown in Fig. 2.19(a). To this end, the parameters shown in Table 2.1 are employed to generate our theoretical results. The stiffnesses of the flexible end supports are estimated from a strength-of-materials approach to be $k_s^f \approx 12b'l^3/h_ch^3$ and $k_t^f \approx lb'^3/h_ch^3$, where the various geometrical parameters are indicated in Fig. 2.19(a). Here we have assumed $b' > h$, as b' is *not* reported by Arul and Ghatak (2008). Our results are then compared with the experimental results of Arul and Ghatak (2008) in Fig. 2.19(b). We find good agreement upto an indentation depth $\delta \approx 0.1$ mm, i.e. until the point S_{23}. At this point, the bottom surface S_2 begins to interact with the surface S_3 in experiments. This feature is not yet implemented in our mathematical model, so that it is expected that our predictions will deviate from experimental observations.

Geometrical and material parameters	Value
Beam thickness	$h = 0.8$ mm
Micro-channel's thickness	$h_c = 0.1$ mm
Beam's length	$2l = 5 - 8$ mm
Punch radius	$R = 2.24$ mm
Punch length	$l_p = 2.7$ mm
Shear modulus	$G = 1$ MPa
Poission's ratio	$\nu = 0.49$
Young's modulus	$E = 2\,(1+\nu) \approx 3$ MPa
Work of adhesion	$w = 0.045 \times 10^{-3}$ mJ/mm^2 or N/mm

Table 2.1: Geometrical and material parameters considered for modeling adhesives with one micro-channel; see also Fig. 2.19(a). These values are taken from Arul and Ghatak (2008).

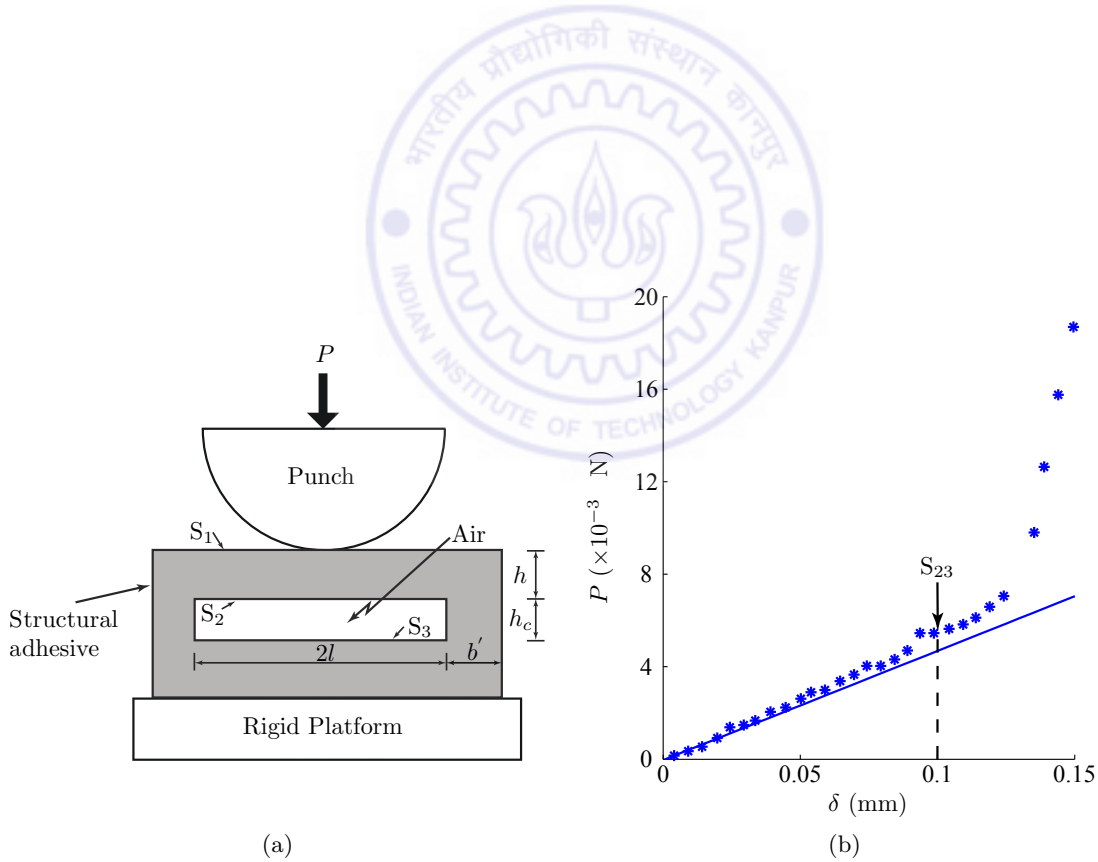

Figure 2.19: (a) A structural adhesive with one micro-channel. (b) Variation of the total load P with the punch's displacement δ. The solid line represents the solution obtained from the procedure of Sec. 2.7. Asterisk (*) are the experiemtal results of Arul and Ghatak (2008).

2.10 Conclusions

In this article we present a theoretical model for the indentation of adhesive beams mounted on flexible supports. Adhesion, when present, was incorporated through either the JKR approximation or an adhesive zone model. We approximate the displacement of the bottom surface of the beam through Euler-Benoulli beam theory. This is then utilized to formulate a boundary value problem, which is reduced to a single Fredholm integral equation of the first kind for the unknown contact pressure. The integral equation is then solved through a Galerkin projection employing Chebyshev polynomials. Finite element (FE) simulations were carried out for clamped and simply supported non-adhesive beams, and our results compared well with FE predictions, as well as with previously reported theoretical results. Results for adhesive contact were found for several combinations of adhesive strengths, beam geometries, and support flexibilities characterized through torsional and vertical translational springs. Theoretical results for adhesive clamped beam were compared with preliminary experiments and a satisfactory match was observed. Finally, we demonstrated the application of our approach to model a complex structural adhesive.

भारतीय प्रौद्योगिकी संस्थान कानपुर
INDIAN INSTITUTE OF TECHNOLOGY KANPUR

Chapter 3

Contact mechanics of adhesive beams: Low to high contact areas.

3.1 Introduction

In this chapter we greatly expand the theoretical framework of Chapter 2.

In recent years, indentation of thin adhesive structures have attracted the attention of researchers because of their applications in electronics and computer industry, see e.g. Barthel and Perriot (2007) and Dalmeya et al. (2012). Some of the designs for these structural adhesives are inspired from biology, such as the one proposed by Arul and Ghatak (2008); see Fig. 2.1. The theoretical modeling and characterisation of such structural adhesives is of great interest. Chapter 2 presented a step towards the modeling of structural adhesives of the type shown in Fig. 2.1, by investigating the indentation of adhesive beams resting on flexible supports.

Indentation studies on non-adhesive beams were pursued in the past by Keer and Miller (1983), and Sankar and Sun (1983). They employed integral transforms and Fourier series, respectively. Adhesion was not considered. Recently Kim et al. (2014), revisited the indention of non-adhesive beams through approximate techniques. However, extending the methods of these papers to adhesive beams pose difficulties, as they involve several iterated integral transforms and/or asymptotic matching. Chapter 2 presented a formulation which could address non-adhesive and adhesive contact of beams within the same framework.

In Chapter 2, we investigated indentation by a rigid cylindrical punch of non-adhesive and

adhesive beams on flexible end supports. However, the mathematical model assumed that, during indentation, the displacement of the beam's bottom surface could be approximated by the deflection of the corresponding Euler-Bernoulli beam under the action of a point load. This approximation limited the application of Chapter 2's approach to indentations where the extent a of the contact region was less than or equal to the thickness h of the beam. Here we release the assumption of Chapter 2 in order to extend our framework to indentation with large contact areas. This leads naturally to a set of dual integral equations for the unknown contact pressure and the displacement of the beam's bottom surface.

In this chapter, we restrict ourselves to clamped and simply supported beams which, as shown in Chapter 2, bound the range of behaviors displayed by beams on flexible supports.

As in Chapter 2, adhesion is modeled through the adhesive-zone model, which allows us to study the JKR (Johnson et al., 1971) and DMT (Derjaguin et al., 1975) approximations of adhesive contact by varying a parameter that regulates adhesive strength. Additionally, by setting adhesive strength to zero we obtain results for non-adhesive contact.

This chapter is organised as follows: We first present the mathematical model, which leads to a set of dual integral equations in terms of the contact pressure and the vertical displacement of the beam's lower surface. This is followed by non-dimensionalization and the formulation of the corresponding numerical algorithm to solve the integral equations. We then briefly discuss the FE model employed to study non-adhesive beam indentation. Next, we present and discuss results for different types of adhesive and non-adhesive contacts. Finally, we compare our predictions with preliminary experiments.

3.2 Mathematical model

We begin, as in Chapter 2, by extending the beams of Fig. 3.1(a) beyond the supports to infinity; see Fig. 3.1(b). This extension is done in keeping with the kinematic and kinetic constraints imposed by the supports. Thus, the beam is extended linearly along the slope at the supports. The beams may now be represented as a linear elastic layer of infinite length with thickness h, and with Young's modulus E and Poisson's ratio ν. The top and bottom surfaces of the beam are frictionless. The corresponding elasticity problem is now

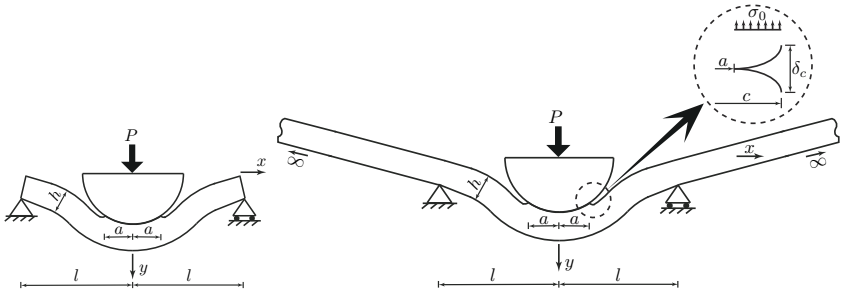

Figure 3.1: (a) Indentation by a rigid circular punch of an adhesive simply supported beam. (b) Mathematical model for the simply supported beam indentation by extending the beam to infinity along its slope near the ends. The inset shows the adhesive zone model employed in our mathematical formulation.

solved, the details of which are in Sec. 2 of Chapter 2. This yields the vertical displacement of the beam's top surface ($y = 0$) and the normal traction acting on the beam's bottom surface ($y = h$) as, respectively,

$$v(x,0) = -\frac{2}{\pi E^*}\int_0^\infty \bar{P}_c(\xi)\; K_1(\xi,x)\; d\xi + \frac{1}{\pi}\int_0^\infty \bar{v}_b(\xi)\; K_2(\xi,x)\; d\xi \tag{3.1}$$

and
$$\tau_{yy}(x,h) = \frac{1}{\pi}\int_0^\infty \bar{P}_c(\xi)\; K_2(\xi,x)\; d\xi + \frac{E^*}{\pi}\int_0^\infty \bar{v}_b(\xi)\; K_3(\xi,x)\cos\xi x\, d\xi, \tag{3.2}$$

where

$$\bar{P}_c(\xi) = \int_{-\infty}^{\infty} -P_c(t)\cos\xi t\, dt \quad \text{and} \quad \bar{v}_b(\xi) = \int_{-\infty}^{\infty} v_b(t)\cos\xi t\, dt \tag{3.3}$$

are the Fourier transforms of the normal force $P_c(t)$ acting on the beam's top surface and the vertical displacement $v_b(t)$ of the beam's bottom surface, respectively, while

$$K_1(\xi,x) = \frac{\sinh^2\xi h}{\xi\left(\xi h + \sinh\xi h\cosh\xi h\right)}\cos\xi x, \quad K_2(\xi,x) = \frac{\sinh\xi h + \xi h\cosh\xi h}{\xi h + \sinh\xi h\cosh\xi h}\cos\xi x$$

and
$$K_3(\xi,x) = \frac{\xi}{2}\cdot\frac{\sinh^2\xi h - \xi^2 h^2}{\xi h + \sinh\xi h\cosh\xi h}\cos\xi x.$$

To ease non-dimensionalization we expand (3.1) and (3.2) by employing definitions of $\bar{P}_c$ and $\bar{v}_b$ to obtain:

$$v\left(x,0\right)=\frac{2}{\pi E^{*}}\int_{0}^{\infty}\int_{-\infty}^{\infty}P_c\left(t\right)\cos\xi t\,dt\,K_1\left(\xi,x\right)\,d\xi+\frac{1}{\pi}\int_{0}^{\infty}\int_{-\infty}^{\infty}v_b\left(t\right)\cos\xi t\,dt\,K_2\left(\xi,x\right)\,d\xi \tag{3.4}$$

$$\text{and}\quad \tau_{yy}\left(x,h\right)=\frac{1}{\pi}\int_{0}^{\infty}\int_{-\infty}^{\infty}-P_c\left(t\right)\cos\xi t\,dt\,K_2\left(\xi,x\right)\,d\xi+\frac{E^{*}}{\pi}\int_{0}^{\infty}\int_{-\infty}^{\infty}v_b\left(t\right)\cos\xi t\,dt\,K_3\left(\xi,x\right)\,d\xi. \tag{3.5}$$

In (3.5), the second integral is singular at $\xi\to\infty$. This singularity may be eliminated by integrating twice by parts, to find

$$\tau_{yy}\left(x,h\right)=\frac{1}{\pi}\int_{0}^{\infty}\int_{-\infty}^{\infty}-P_c\left(t\right)\cos\xi t\,dt\,K_2\left(\xi,x\right)\,d\xi-\frac{E^{*}}{\pi}\int_{0}^{\infty}\int_{-\infty}^{\infty}\kappa_b\left(t\right)\cos\xi t\,dt\;\frac{1}{\xi^2}K_3\left(\xi,x\right)\,d\xi, \tag{3.6}$$

where $\kappa_b\left(t\right)=d^2v_b/dt^2$.

The contact region's vertical displacement is fixed by the displacement of the punch δ and the profile $g(x)$ of the punch. So within the contact zone, i.e. $-a\le x\le a$ – where a locates the contact edge - we set $v(x,0)=\delta-g(x)$. When a and δ are small compared to the radius R of the punch, we approximate the cylindrical profile of the punch by a parabola. Furthermore, there is no normal traction at the bottom surface of the beam, except at the supports; see Fig. 3.1. Thus, at the top and bottom surfaces of the layer we have, respectively,

$$v(x,0)=\delta-\frac{x^2}{2R}\quad\text{for}\quad -a\le x\le a, \tag{3.7}$$

$$\text{and}\qquad \tau_{yy}\left(x,h\right)=0\quad\text{for}\quad -l<x<l. \tag{3.8}$$

We model adhesive interaction between the punch and the beam through an adhesive-zone (Maugis, 1992). The normal tractions within the adhesive zone follow the Dugdale-Barenblatt model, in which a constant attractive force σ_0 acts per unit length within the adhesive zone of length $d=c-a$, where c demarcates the adhesive zone's outer edge, see

inset in Fig. 3.1(b). With this we write the normal traction on the top surface as

$$P_c(x) = \begin{cases} p(x) & \text{for } |x| \le a, \\ -\sigma_0 & \text{for } a \le |x| \le c, \\ 0 & \text{for } |x| > c. \end{cases} \tag{3.9}$$

An adhesive-zone model resolves stress singularities at the contact edges ($x = \pm a$) inherent in the JKR approximation by requiring the normal traction be continuous there, i.e.,

$$\lim_{x \to \pm a^{\mp}} p(x) = -\sigma_0. \tag{3.10}$$

An adhesive zone introduces the extra variable c into the contact problem. The required additional equation is obtained by equating the energy release rate G – computed employing the $J-$Integral (Rice, 1968) – to the work of adhesion w, to obtain the energy balance

$$\sigma_0 \delta_c = w, \tag{3.11}$$

where

$$\delta_c = \left(c^2/2R\right) - \delta + v_c \tag{3.12}$$

is the air gap at the end of the adhesive zone (see inset in Fig. 3.1(b)) and $v_c = v(c, 0)$ is the vertical displacement of the top surface at $x = c$.

In non-adhesive indentation, $\sigma_0 = 0 = w$, and (3.11) is automatically satisfied. When the JKR approximation is invoked, $\sigma_0 \to \infty$ and $c \to a$, so that employing the Griffith's criterion (3.11) becomes

$$\frac{K_1^2}{2E^*} = w, \tag{3.13}$$

where

$$K_1 = -\lim_{x \to a^-} \sqrt{2\pi (a - x)} p(x) \tag{3.14}$$

is the *stress intensity factor*; see e.g. Kanninen and Popelar (1985, p. 168). Note that the continuity condition (3.10) is redundant for the JKR approximation.

Finally, the total load acting on the punch is

$$P = \int_{-\infty}^{\infty} P_c(x)\, dx = \int_{-a}^{a} p(x)\, dx - 2\,\sigma_0\,(c - a). \tag{3.15}$$

3.3 Non-dimensionalization

We generally follow the non-dimensionalization of Chapter 2:

$$A = \frac{a}{l}; \quad \varphi(\bar{\tau}) = \frac{aRl}{Kh^3} p(a\bar{\tau}); \quad \bar{P} = \frac{PRl}{Kh^3};$$
$$\Delta = \frac{\delta R}{l^2}; \quad L = \frac{l}{R}; \quad \lambda = 2\sigma_0 \left(\frac{R}{\pi w K^2}\right)^{1/3}; \quad m = \left(\frac{\pi w}{RK}\right)^{1/3},$$

where $K = 4\,E^*/3$. The variables are scaled as

$$\left\{\bar{x}, \bar{\tau}, \bar{c}, \bar{l}, \bar{\gamma}\right\} = \frac{1}{a}\{x, t, c, l, h\}; \quad \{\hat{x}, \hat{\tau}, \hat{\gamma}\} = \frac{1}{l}\{x, t, h\}; \quad \{\omega, \bar{\omega}, \hat{\omega}\} = \left\{\xi h, \frac{\omega}{\bar{\gamma}}, \frac{\omega}{\hat{\gamma}}\right\};$$
$$\Phi(\tau) = \frac{aRl}{Kh^3} P(a\bar{\tau}); \quad \vartheta_b(\hat{\tau}) = v_b(\hat{\tau}) \left(\frac{R}{l^2}\right); \quad \kappa_b(\hat{\tau}) = \frac{d^2\vartheta_b(\hat{\tau})}{d\hat{\tau}^2}; \quad \mathcal{T}(\hat{x}, h) = \frac{\tau_{yy}(\hat{x}, h)}{K} \frac{8\hat{\gamma}}{3L}.$$

Employing the above, the non-dimensional vertical displacement of the top surface (3.4) and the normal traction at the bottom surface (3.6) become, respectively,

$$\vartheta(\bar{x}, 0) = \frac{8\hat{\gamma}^3}{3\pi} \int_0^\infty \int_{-\infty}^\infty \Phi(\bar{\tau}) \cos(\bar{\omega}\tau)\, d\bar{\tau}\, K_1^t(\bar{\omega}, \bar{x})\, d\omega + \frac{1}{\pi\hat{\gamma}} \int_0^\infty \int_{-\infty}^\infty \vartheta_b(\hat{\tau}) \cos(\hat{\omega}\hat{\tau})\, d\hat{\tau}\, K_2^t(\bar{\omega}, \bar{x})\, d\omega \tag{3.16}$$

and

$$\mathcal{T}(\hat{x}, h) = \frac{8\hat{\gamma}^3}{3\pi} \int_0^\infty \int_{-\infty}^\infty -\Phi(\bar{\tau}) \cos(\bar{\omega}\bar{\tau})\, d\bar{\tau}\, K_1^b(\hat{\omega}, \hat{x})\, d\omega - \frac{\hat{\gamma}}{\pi} \int_0^\infty \int_{-\infty}^\infty \kappa_b(\hat{\tau}) \cos(\hat{\omega}\hat{\tau})\, d\hat{\tau}\, K_2^b(\hat{\omega}, \hat{x})\, d\omega, \tag{3.17}$$

where the kernels

$$K_1^t(\bar{\omega}, \bar{x}) = \frac{\sinh^2\omega}{\omega(\omega + \sinh\omega\cosh\omega)} \cos(\bar{\omega}\bar{x}), \qquad K_2^t(\bar{\omega}, \bar{x}) = \frac{\sinh\omega + \omega\cosh\omega}{\omega + \sinh\omega\cosh\omega} \cos(\bar{\omega}\bar{x}),$$
$$K_1^b(\hat{\omega}, \hat{x}) = \frac{\sinh\omega + \omega\cosh\omega}{\omega + \sinh\omega\cosh\omega} \cos(\hat{\omega}\hat{x}) \quad \text{and} \qquad K_2^b(\hat{\omega}, \hat{x}) = \frac{1}{\omega} \cdot \frac{\sinh^2\omega - \omega^2}{\omega + \sinh\omega\cosh\omega} \cos(\hat{\omega}\hat{x}). \tag{3.18}$$

Non-dimensionalizing (3.7) – (3.11) yields

$$\vartheta(\bar{x},0) = \Delta - \frac{1}{2}\,\bar{x}^2 A^2 \quad \text{for} \quad -1 \le \bar{x} \le 1, \tag{3.19}$$

$$\mathcal{T}\,(\hat{x},h) = 0 \quad \text{for} \quad -1 < \hat{x} < 1, \tag{3.20}$$

$$\Phi\,(\bar{\tau}) = \begin{cases} \varphi\,(\bar{\tau})\,, & -1 \le \bar{\tau} \le 1 \\ -\lambda A m/2\hat{\gamma}^3 L, & 1 \le |\bar{\tau}| \le \bar{c} \\ 0, & |\bar{\tau}| > \bar{c} \end{cases} \tag{3.21}$$

$$\varphi\,(\pm 1) = -\frac{\lambda A m}{2\hat{\gamma}^3 L} \tag{3.22}$$

and

$$1 = \frac{\pi\lambda L^2}{2m^2}\,\left(\frac{1}{2}\,\bar{c}^2\,A^2 - \Delta + \vartheta_c\right), \tag{3.23}$$

where $\vartheta\,(\bar{c}) = \vartheta\,(\bar{c},0)$, and $\Delta = \vartheta\,(0,0)$. In the JKR approximation, we replace (3.22) and (3.23) by the non-dimensional Griffith's criterion, obtained from (3.13) and (3.14):

$$\lim_{\bar{x}\to 1^-} \sqrt{(1-\bar{x})}\varphi\,(\bar{x}) = -\frac{m}{2\pi L}\left(\frac{l}{h}\right)^3 \sqrt{\frac{3Am}{L}}. \tag{3.24}$$

Substituting (3.21) in (3.16) and (3.17) yields

$$\vartheta\,(\bar{x},0) = -\,\frac{8\hat{\gamma}^3}{3\pi}\int_0^\infty \bar{\varphi}\,(\bar{\omega})\,K_1^t\,(\bar{\omega},\bar{x})\,d\omega - \frac{8\lambda A m}{3\pi L}\int_0^\infty \bar{\varphi}_0\,(\bar{\omega})\,K_1^t\,(\bar{\omega},\bar{x})\,d\omega + \frac{1}{\pi\hat{\gamma}}\int_0^\infty \hat{\vartheta}_b\,(\hat{\omega})\,K_2^t\,(\bar{\omega},\bar{x})\,d\omega, \tag{3.25}$$

and

$$\mathcal{T}\,(\hat{x},h) = \frac{8\hat{\gamma}^3}{3\pi}\int_0^\infty \bar{\varphi}\,(\bar{\omega})\,K_1^b\,(\hat{\omega},\hat{x})\,d\omega + \frac{8\lambda A m}{3\pi L}\int_0^\infty \bar{\varphi}_0\,(\bar{\omega})\,K_1^b\,(\hat{\omega},\hat{x})\,d\omega - \frac{\hat{\gamma}}{\pi}\int_0^\infty \hat{\kappa}_b\,(\hat{\omega})\,K_2^b\,(\hat{\omega},\hat{x})\,d\omega, \tag{3.26}$$

with

$$\bar{\varphi}\,(\bar{\omega}) = -\int_{-1}^{1} \varphi\,(\bar{\tau})\cos\bar{\omega}\,\bar{\tau}\,d\bar{\tau}, \qquad \bar{\varphi}_0\,(\bar{\omega}) = \int_1^{\bar{c}} \cos\bar{\omega}\,\bar{\tau}\,d\bar{\tau},$$

$$\hat{\vartheta}_b\,(\hat{\omega}) = \int_{-\infty}^{\infty} \vartheta_b\,(\hat{\tau})\cos\hat{\omega}\hat{\tau}\,d\hat{\tau} \quad \text{and} \quad \hat{\kappa}_b\,(\hat{\omega}) = \int_{-\infty}^{\infty} \kappa_b\,(\hat{\tau})\cos\hat{\omega}\hat{\tau}\,d\hat{\tau}. \tag{3.27}$$

Then, combining (3.25) with (3.19), and (3.26) with (3.20), we obtain

$$\Delta - \frac{1}{2}\,\bar{x}^2 A^2 = -\frac{8\hat{\gamma}^3}{3\pi}\int_0^\infty \bar{\varphi}\,(\bar{\omega})\;K_1^t\,(\bar{\omega},\bar{x})\;\,d\omega - \frac{8\lambda A m}{3\pi L}\int_0^\infty \bar{\varphi}_0\,(\bar{\omega})\;K_1^t\,(\bar{\omega},\bar{x})\;\,d\omega$$
$$+\frac{1}{\pi\hat{\gamma}}\int_0^\infty \hat{\vartheta}_b\,(\hat{\omega})\;K_2^t\,(\bar{\omega},\bar{x})\;\,d\omega \quad \text{for } -1\le\bar{x}\le 1 \tag{3.28}$$

and

$$0 = -\frac{8\hat{\gamma}^3}{3\pi}\int_0^\infty \bar{\varphi}\,(\bar{\omega})\;K_1^b\,(\hat{\omega},\hat{x})\;\,d\omega - \frac{8\lambda A m}{3\pi L}\int_0^\infty \bar{\varphi}_0\,(\bar{\omega})\;K_1^b\,(\hat{\omega},\hat{x})\;\,d\omega$$
$$+\frac{\hat{\gamma}}{\pi}\int_0^\infty \hat{\kappa}_b\,(\hat{\omega})\;K_2^b\,(\hat{\omega},\hat{x})\;\,d\omega \quad \text{for } -1<\hat{x}<1. \tag{3.29}$$

Finally, the total non-dimensional load acting on the punch is given by

$$\bar{P} = \int_{-1}^{1}\varphi\,(\bar{\tau})\;d\bar{\tau} - \frac{\lambda A m}{\hat{\gamma}^3 L}\,(\bar{c}-1)\,. \tag{3.30}$$

Equations (3.28) and (3.29) are coupled Fredholm integral equations of the first kind; see Polyanin and Manzhirov (2008, p. 573). These, along with (3.22) and (3.23), are to be solved for $\bar{\varphi}$, $\bar{\vartheta}$, $\bar{c}$ and Δ for a given contact area A. The numerical algorithm employed for this is discussed next.

3.4 Numerical solution

The dual integral equations (3.28) and (3.29) cannot be solved in closed form due to the presence of complex kernels; cf. (3.18). We, therefore employ a numerical solution.

We begin by approximating the contact pressure φ as

$$\varphi\,(\bar{\tau}) = \frac{-\lambda A m}{2\hat{\gamma}^3 L} + \frac{1}{\sqrt{(1-\bar{\tau}^2)}}\sum_{n=0}^{N} b_{2n}T_{2n}\,(\bar{\tau}) \quad \text{for } -1\le\bar{\tau}\le 1, \tag{3.31}$$

where $T_{2n}\,(\bar{\tau})$ are Chebyshev polynomials of the first kind and b_{2n} are constants that are to be determined. Only even Chebyshev polynomials are considered as the indentation is symmetric about $\bar{\tau}=0$. The constant term is chosen to account for the contact pressure at the contact edge in the adhesive-zone model explicitly. Evaluating the integrals $\bar{\varphi}\,(\bar{\omega})$

and $\bar{\varphi}_0(\bar{\omega})$ in (3.27) after employing (3.31) yields

$$\bar{\varphi}(\bar{\omega}) = \frac{\lambda A m}{\hat{\gamma}^3 L}\frac{\sin\bar{\omega}}{\bar{\omega}} - \sum_{n=0}^{N} b_{2n}\alpha_{2n}(\bar{\omega}) \quad \text{and} \quad \bar{\varphi}_0(\bar{\omega}) = \frac{1}{\bar{\omega}}\left(-\sin\bar{\omega} + \sin\bar{\omega}\,\bar{c}\right), \tag{3.32}$$

where

$$\alpha_{2n}(\bar{\omega}) = \int_{-1}^{1} \frac{1}{\sqrt{(1-\bar{\tau}^2)}} T_{2n}(\bar{\tau})\cos\bar{\omega}\bar{\tau}\; d\bar{\tau}. \tag{3.33}$$

The evaluation of the integrals $\alpha_{2n}(\bar{\omega})$ at different n are available in Appendix D.

Next, we approximate the displacement of the bottom surface $\vartheta_b(\hat{\tau})$ in a series of the natural mode shapes $S_n(\hat{\tau})$ of the beam:

$$\vartheta_b(\hat{\tau}) = d_0 + \sum_{n=1}^{M} d_n S_n(\hat{\tau}). \tag{3.34}$$

We note that $S_n(\hat{\tau}) = \cos(n\pi\hat{\tau})$ and $S_n(\hat{\tau}) = \sin\{(2n-1)\pi(\hat{\tau}+1)/2\}$ for clamped and simply supported beams, respectively. After these approximations are made to satisfy the beam's end conditions, which gives d_0 in the above, the curvature κ_b of the beam is calculated from ϑ_b. The details of these calculations are available in Appendix I. From (I.15) we find that the Fourier transforms $\hat{\vartheta}_b(\hat{\omega})$ and $\hat{\kappa}_b(\hat{\omega})$, for both clamped and simply supported beams, may be written as

$$\hat{\vartheta}_b(\hat{\omega}) = \sum_{n=1}^{M} d_n\hat{\beta}_n(\hat{\omega}) \quad \text{and} \quad \hat{\kappa}_b(\hat{\omega}) = \sum_{n=1}^{M} d_n\hat{\kappa}_n(\hat{\omega}), \tag{3.35}$$

where the expressions for $\hat{\beta}_n$ and $\hat{\kappa}_n$ are provided in Appendix I.

Substituting (3.32) and (3.35) in the integral equations (3.28) and (3.29) yields, respectively,

$$\Delta - \frac{1}{2}\bar{x}^2A^2 = \frac{8\hat{\gamma}^3}{3\pi}\sum_{n=0}^{N} b_{2n}\mathcal{J}^t_{2n}(\bar{x}) - \frac{8\lambda A m}{3\pi L}\mathcal{J}^t(\bar{x}) + \frac{1}{\pi\hat{\gamma}}\sum_{n=1}^{M} d_n\mathcal{Q}^t_n(\bar{x}) \tag{3.36}$$

and

$$0 = \frac{8\hat{\gamma}^3}{3\pi}\sum_{n=0}^{N} b_{2n}\mathcal{J}^b_{2n}(\hat{x}) - \frac{8\lambda A m}{3\pi L}\mathcal{J}^b(\hat{x}) + \frac{\hat{\gamma}}{\pi}\sum_{n=1}^{M} d_n\mathcal{Q}^b_n(\hat{x}), \tag{3.37}$$

where

$$\mathcal{J}^t_{2n}(\bar{x}) = \int_0^\infty \alpha_{2n}(\bar{\omega})\ K^t_1(\bar{\omega},\bar{x})\ d\omega, \qquad \mathcal{J}^t(\bar{x}) = \int_0^\infty \frac{1}{\bar{\omega}}\sin(\bar{\omega}\,\bar{c})\ K^t_1(\bar{\omega},\bar{x})\ d\omega,$$

$$\mathcal{Q}^t_n(\bar{x}) = \int_0^\infty \hat{\beta}_n(\hat{\omega})\ K^t_2(\bar{\omega},\bar{x})\ d\omega, \qquad \mathcal{Q}^b_n(\hat{x}) = \int_0^\infty \hat{\kappa}_n(\hat{\omega})\ K^b_2(\hat{\omega},\hat{x})\ d\omega,$$

$$\mathcal{J}^b_{2n}(\hat{x}) = \int_0^\infty \alpha_{2n}(\bar{\omega})\ K^b_1(\hat{\omega},\hat{x})\ d\omega \quad \text{and} \quad \mathcal{J}^b(\bar{x}) = \int_0^\infty \frac{1}{\bar{\omega}}\sin(\bar{\omega}\,\bar{c})\ K^b_1(\hat{\omega},\hat{x})\ d\omega.$$

The above integrals may be evaluated at any $\bar{x}$ or $\hat{x}$ through the Clenshaw-Curtis quadrature; see Press et al. (1992, p. 196).

Employing (3.31), the constraint (3.22) on the contact pressure at the ends of the contact region provides

$$b_0 + b_2 + \cdots + b_{2N} = 0. \tag{3.38}$$

Utilizing the approximations (3.32) and (3.35), the energy balance equation (3.23) yields

$$\frac{\pi\lambda L^2}{2m^2}\left(\frac{1}{2}\,\bar{c}^2\,A^2 - \Delta + \vartheta_c\right) = 1, \tag{3.39}$$

with

$$\vartheta(\bar{c}) = \frac{8\hat{\gamma}^3}{3\pi}\sum_{n=0}^{N} b_{2n}\mathcal{J}^t_{2n}(\bar{c}) - \frac{8\lambda A m}{3\pi L}\mathcal{J}^t(\bar{c}) + \frac{1}{\pi\hat{\gamma}}\sum_{n=1}^{M} d_n\mathcal{Q}^t_n(\bar{c}), \tag{3.40}$$

where Δ is the displacement of the punch. We recall that the energy balance (3.39) is redundant for the case of adhesionless contact or when the JKR approximation is invoked.

Finally, the total load acting on the punch becomes after employing (3.8) and (3.31):

$$\bar{P} = \pi b_0 - \frac{\lambda A m}{\hat{\gamma}^3 L}\bar{c}. \tag{3.41}$$

3.5 Algorithm

We need to solve (3.36) – (3.39) for the $N + M + 3$ unknowns b_{2n}, d_n, Δ and $\bar{c}$ at any given contact area A. These are solved through the collocation technique (Atkinson, 1997, p. 135), which provides the necessary $N + M + 3$ algebraic equations.

In the collocation method, (3.36) and (3.37) are required to hold exactly at, respectively, $N+1$ and M *collocation points*. The collocation points for (3.36) and (3.37) are selected to be

$$\bar{x}_i = \cos\left\{\frac{(2i-1)\,\pi}{2\,(N+1)}\right\} \text{ for } i = 1, \cdots, N+1,$$

and

$$\hat{x}_k = \frac{k-1}{M} \text{ for } k = 1, \cdots, M,$$

respectively. Here, $\bar{x}_i$ are the $N+1$ zeros of the (Chebyshev) polynomials $T_{2N+2}(\bar{x}_i)$ (Mason and Handscomb, 2003, p. 19), while $\hat{x_k}$ are simply equally spaced points lying between 0 and 1. At these collocation points (3.36) and (3.37) become, respectively,

$$\Delta - \frac{1}{2}\,\bar{x}_i^2 A^2 = \frac{8\hat{\gamma}^3}{3\pi}\sum_{n=0}^{N} b_{2n}\mathcal{J}_{2n}^t\left(\bar{x}_i\right) - \frac{8\lambda A m}{3\pi L}\mathcal{J}^t\left(\bar{x}_i\right) + \frac{1}{\pi\hat{\gamma}}\sum_{n=1}^{M} d_n \mathcal{Q}_n^t\left(\bar{x}_i\right) \tag{3.42}$$

and

$$0 = \frac{8\hat{\gamma}^3}{3\pi}\sum_{n=0}^{N} b_{2n}\mathcal{J}_{2n}^b\left(\hat{x}_k\right) - \frac{8\lambda A m}{3\pi L}\mathcal{J}^b\left(\hat{x}_k\right) + \frac{\hat{\gamma}}{\pi}\sum_{n=1}^{M} d_n \mathcal{Q}_n^b\left(\hat{x}_k\right), \tag{3.43}$$

with $i = 1, \cdots, N+1$ and $k = 1, \cdots, M$. Thus, we obtain $N+1$ equations from (3.42) and M equations from (3.43) for a total of $N+M+1$ equations. Along with (3.38) and (3.39), we finally obtain the required $N+M+3$ equations to solve for the $N+1$ unknowns b_{2n}, M unknowns d_n, Δ and $\bar{c}$. This system of non-linear algebraic equations is solved for any given contact area A through the following algorithm:

Step 1: For the given contact area A, we make an initial guess for $\bar{c}$.

Step 2: We then write (3.42) and (3.43) in matrix notation as

$$\Delta\,\underline{e} - \underline{f} - \underline{\lambda} = \underline{\underline{R}}\,\underline{a}, \tag{3.44}$$

where

$$\underline{e} = \left[\underline{e}^t, \underline{e}^b\right]^{\mathrm{T}}; \quad \underline{f} = \left[\underline{f}^t, \underline{f}^b\right]^{\mathrm{T}}; \quad \underline{\lambda} = \left[\underline{\lambda}^t, \underline{\lambda}^b\right]^{\mathrm{T}}; \quad \underline{a} = \left[\underline{a}^t, \underline{a}^b\right]^{\mathrm{T}}; \quad \underline{\underline{R}} = \begin{bmatrix} \underline{\underline{\mathcal{J}}}^t & \underline{\underline{\mathcal{Q}}}^t \\ \underline{\underline{\mathcal{J}}}^b & \underline{\underline{\mathcal{Q}}}^b \end{bmatrix}, \tag{3.45}$$

with

$$a_i^t = b_{2i-2};\; a_k^b = d_k; \quad e_i^t = 1;\; e_k^b = 0; \quad f_i^t = \frac{x_i^2 A^2}{2}; \quad f_k^b = 0;$$
$$\lambda_i^t = -\frac{8\lambda A m}{3\pi L}\mathcal{J}^t(\bar{x}_i); \quad \lambda_k^b = -\frac{8\lambda A m}{3\pi L}\mathcal{J}^b(\hat{x}_k); \quad \mathcal{J}_{i\,j}^t = \frac{8\hat{\gamma}^3}{3\pi}\mathcal{J}_{2j-2}^t(\bar{x}_i);$$
$$\mathcal{Q}_{i\,r}^t = \frac{1}{\pi\hat{\gamma}}\mathcal{Q}_r^t(\bar{x}_i); \quad \mathcal{J}_{k\,j}^b = \frac{8\hat{\gamma}^3}{3\pi}\mathcal{J}_{2j-2}^b(\hat{x}_k); \quad \mathcal{Q}_{i\,r}^b = \frac{\hat{\gamma}}{\pi}\mathcal{Q}_r^b(\hat{x}_k), \tag{3.46}$$

for $i, j = 1, 2, \cdots, N+1$ and $k, r = 1, 2, \cdots, M$. Thus, $\underline{e}$, $\underline{f}$, $\underline{\lambda}$, $\underline{a}$ are column vectors of size $N+M+1$, and $\underline{\underline{R}}$ is a matrix of size $(N+M+1)\times(N+M+1)$.

Step 3: Note that the column vector $\underline{a}$ consists of the coefficients occurring in expressions (3.31) for the contact pressure and (3.34) for the displacement. We now invert (3.44) to find $\underline{a}$ in terms of Δ:

$$\underline{a} = \Delta\underline{E} - \underline{F} - \underline{\Lambda}, \tag{3.47}$$

where

$$\underline{E} = \underline{\underline{R}}^{-1}\cdot\underline{e}, \quad \underline{F} = \underline{\underline{R}}^{-1}\cdot\underline{f} \quad \text{and} \quad \underline{\Lambda} = \underline{\underline{R}}^{-1}\cdot\underline{\lambda}.$$

Step 4: Employing the end condition (3.38) for the contact pressure, we obtain the punch's displacement

$$\Delta = \frac{p_0 + \sum_{i=1}^{N+1} F_i + \sum_{i=1}^{N+1}\Lambda_i}{\sum_{i=1}^{N+1} E_i}, \tag{3.48}$$

where

$$p_0 = \begin{cases} 0 & \text{if there is no adhesion or an adhesive zone is present,} \\ -\left(m\sqrt{6Am}/2\pi L^2\right)(l/h)^3 & \text{if the JKR approximation is invoked.} \end{cases} \tag{3.49}$$

Step 5: Once Δ is known, we evaluate $\underline{a}$ from (3.47) through

$$\underline{a} = \left(\frac{p_0 + \sum_{i=1}^{N+1} F_i + \sum_{i=1}^{N+1}\Lambda_i}{\sum_{i=1}^{N+1} E_i}\right)\underline{E} - \underline{F} - \underline{\Lambda}. \tag{3.50}$$

Step 6: Employing Δ and $\underline{a}$, we calculate the displacement of the beam's top surface at $\bar{c}$ from (3.40) and check whether (3.39) holds. If not, then we update $\bar{c}$ employing the Newton-Raphson method (Chatterjee, 2002). Steps 1-6 are repeated until (3.39)

is satisfied. Steps 1 and 6 are required only when we employ an adhesive zone. When the Hertzian or JKR approximations are invoked we may conveniently skip this Step 6.

Step 7: We finally proceed to find the contact pressure distribution $\varphi(\bar{\tau})$ and the total load $\bar{P}$ from (3.31) and (3.41), respectively.

3.6 Finite element (FE) computations

Finite element (FE) computations are carried out for clamped and simply supported beams for adhesionless contact. These are employed to validate our semi-analytical results.

The FE model is prepared in ABAQUS as described in Chapter 2: the beam is modelled as a linear elastic layer of Young's modulus $E = 2000$ MPa, Poisson's ratio $\nu = 0.3$, thickness $h = 4$ mm, and half-span $l = 40$ mm. The rigid punch is modeled as a much stiffer elastic material with Young's modulus $E_p = 2 \times 10^6$ MPa and radius $R = 225$ mm. Plane-strain elements are considered both for the beam and the punch. A concentrated load is applied on the punch. Computations provide the contact pressure φ, contact area A, punch's displacement Δ, and the displacement ϑ_b of the beam's bottom surface.

3.7 Results: Non-adhesive ('Hertzian') contact

We now report results for the non-adhesive interaction of clamped and simply supported beams with a rigid cylindrical punch.

For non-adhesive interaction, we set $\lambda = 0$ in (3.36) and (3.37) to obtain

$$\Delta - \frac{1}{2}\bar{x}^2 A^2 = \frac{8\hat{\gamma}^3}{3\pi}\sum_{n=0}^{N} b_{2n}\mathcal{J}_{2n}^{t}(\bar{x}) + \frac{1}{\pi\hat{\gamma}}\sum_{n=1}^{M} d_n \mathcal{Q}_n^{t}(\bar{x}) \tag{3.51}$$

and

$$0 = \frac{8\hat{\gamma}^3}{3\pi}\sum_{n=0}^{N} b_{2n}\mathcal{J}_{2n}^{b}(\hat{x}) + \frac{\hat{\gamma}}{\pi}\sum_{n=1}^{M} d_n \mathcal{Q}_n^{b}(\hat{x}), \tag{3.52}$$

respectively. In non-adhesive contact, the interacting surfaces detach smoothly at the contact edges, so that the pressure vanishes at the contact edge, and (3.38) holds, i.e.

$$b_0 + b_2 + \cdots + b_{2N} = 0. \tag{3.53}$$

We proceed to solve (3.51) – (3.53) through the procedure of Sec. 3.5. We set $N = 5$ and $M = 50$ in our computations. Initially to compare our results with FE computations we employ the parameters of Sec. 3.6.

Figure 3.2 plots $\varphi(\bar{x})$ and $ap(\bar{x})$, computed by solving (3.51) – (3.53) and from FE simulations. Results for both clamped and simply supported beams are shown. These pressure

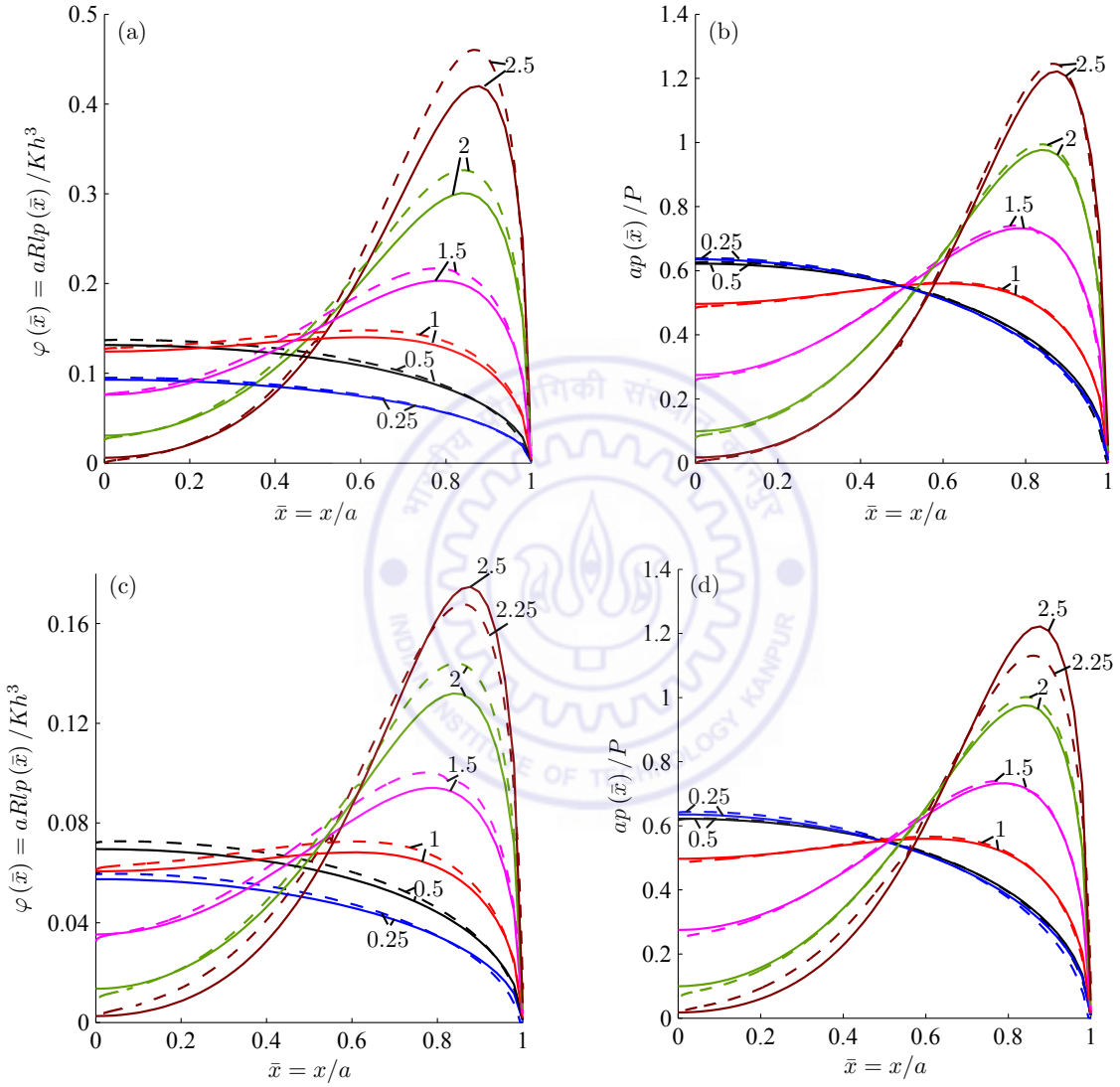

Figure 3.2: The non-dimensional contact pressures $\varphi(\bar{x})$ and $ap(\bar{x})/P$ during the non-adhesive indentation of a clamped (a and b) and simply supported (c and d) beams. We set $h = 4$ mm and $l = 40$ mm. Several contact areas a are investigated by varying a/h ratio, which are noted next to then corresponding curves. The solid lines are results obtained from the semi-analytical procedure of Sec. 3.4, while dashed line represent FE computations.

profiles are plotted at different a/h ratios, by varying the contact area a, for a beam of thickness h and half-span l. We observe that at low a/h ratios, the contact pressure is

maximum at the center of the contact area and vanishes as we approach the contact edges. Increasing a/h causes the contact pressure to decrease at the center of the contact area and increase near its ends. This behavior was also observed in Chapter 2.

As in Chapter 2, we find that, at the same a/h, the contact pressure φ in a simply supported beam is smaller than that in a clamped beam, because the bending stiffness of the former is lower. However, this difference is not reflected when we plot $ap\,(\bar{x})$; cf. Figs. 3.2(b) and 3.2(d) . We observe a close match between our predictions and FE simulations for all a/h, except for a small deviation between the two at $a/h = 2.5$ in the case of simply supported beams. We suspect that the latter may be due to the zero displacement end condition at the bottom surface of the beam that was employed in the theoretical analysis but can not be imposed explicitly in the FE model. We note that the method of Chapter 2 does well untill $a/h \approx 1$. With greater indentation, the a/h ratio increases, and the contact pressure at the center of the contact patch becomes negative. This reflects loss of contact[1], which is observed in both theoretical predictions and FE computations. For clamped beams, contact loss initiates at the center of the contact area when $a/h \gtrsim 2.5$. In simply supported beams contact loss is predicted for $a/h \gtrsim 2.5$ by our analytical model but for $a/h \gtrsim 2.25$ by FE simulations.

Next, in Fig. 3.3 we compare our results for contact pressures $ap\,(\bar{x})$ with those of Keer and Miller (1983) for both clamped and simply supported beams. We find an extremely close match between the two untill $a/h \approx 2$. Beyond that, while the match remains close for almost the entire contact area, a deviation is observed at the center of the contact patch: we find negative pressures at the center of the contact patch, whereas Keer and Miller (1983) report no negative contact pressure. From this, it appears that the earlier formulations of Keer and Miller (1983) – also Sankar and Sun (1983), which we discuss later – do *not* predict contact loss. Figure 3.3 confirms our previous observation that contact pressures of clamped and simply supported beams do *not* vary much, when scaled as $ap(\bar{x})/P$.

Next, in Fig. 3.4 we plot the variation of the contact area A with the total load $\bar{P}$ on the punch and the punch's displacement Δ for both clamped and simply supported beams. We also compare with FE computations and results of Sankar and Sun (1983). The process is

[1]The current theoretical formulation is not valid after the contact loss.

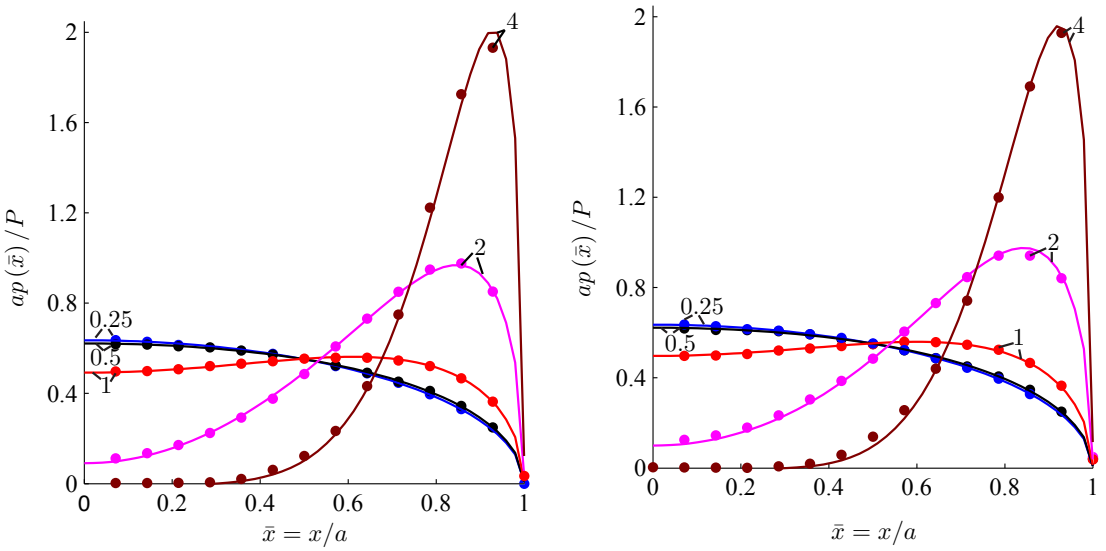

Figure 3.3: The non-dimensional contact pressures $ap(\bar{x})/P$ during the non-adhesive indentation of (a) a clamped and (b) a simply beam. The slenderness ratio of the beam $l/h = 10$. Several contact areas a are investigated by varying a/h ratio, which are noted next to then corresponding curves. The solid lines are results obtained from the semi-analytical procedure of Sec. 3.4. Dots represent the predictions of Keer and Miller (1983).

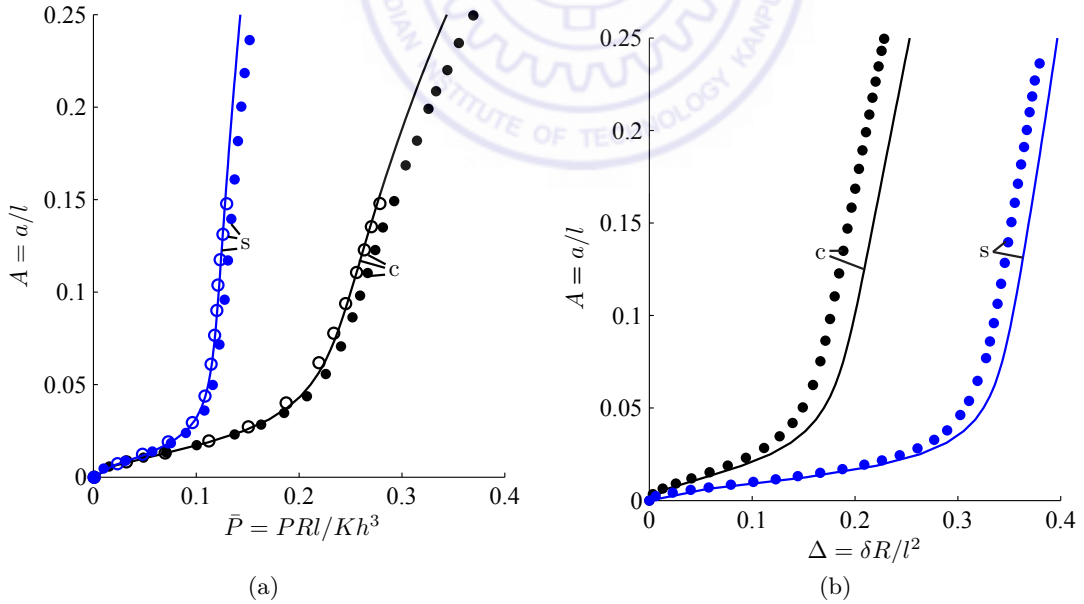

Figure 3.4: Non-adhesive contact of clamped ('c') and simply supported ('s') beams. The contact area A is plotted as a function of (a) the total load $\bar{P}$ acting on the punch and (b) the punch's displacement Δ. The beam's slenderness ratio l/h=10. Solid lines are results obtained from the semi-analytical procedure of Sec. 3.4. Filled circles correspond to FE simulations of Sec. 3.6. Predictions of Sankar and Sun (1983) are shown by open circles, when available.

repeated for the variation of Δ with $\bar{P}$ in Fig. 3.5. Figure 3.4(a) shows that for the same contact area A, the load $\bar{P}$ required for a simply supported beam is small compared to a clamped beam. This is because the simply supported beam bends more easily. This is also why we observe greater displacements Δ in these beams in Figs. 3.4(b) and 3.5. Finally, Figs. 3.4 and 3.5 show a close match of our theoretical predictions with FE computations and the results of Sankar and Sun (1983).

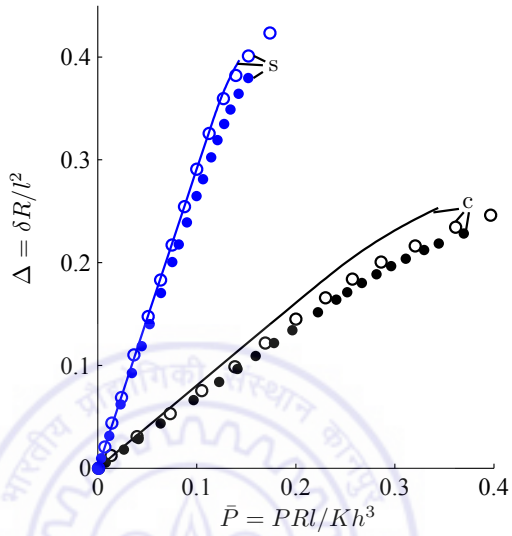

Figure 3.5: Non-adhesive contact of clamped ('c') and simply supported ('s') beams. The displacement Δ of the punch is shown as a function of the total load $\bar{P}$. See also the caption of Fig. 3.4.

As in Chapter 2, we now set the Young's modulus and Poisson's ratio to $E = 0.083$ MPa and $\nu = 0.4$, respectively, as representative of typical adhesives. We also use these material parameters while studying the adhesive beams. The geometric parameters remain unchanged, i.e. $l = 40$ mm, $R = 225$ mm. We show, by varying thickness, the convergence of pressure profiles to that of an elastic half-space in Appendix F ; see Fig. F.1(b).

In Fig. 3.6, we plot the variation of the contact area A with respect to the total load $\bar{P}$ acting on the punch and the punch's displacement Δ at several slenderness ratios l/h for both clamped and simply supported beams. With increasing l/h, the beam's resistance to bending decreases and hence, we find smaller loads $\bar{P}$, or larger deflections Δ, at the same contact area A. For the same reason the load $\bar{P}$ required to achieve the same A in simply supported beam is smaller than the ones for clamped beams. At the same time, the displacements Δ are higher for simply supported beams.

In Fig. 3.6, we observe that the curves change their slope abruptly. This is due to the

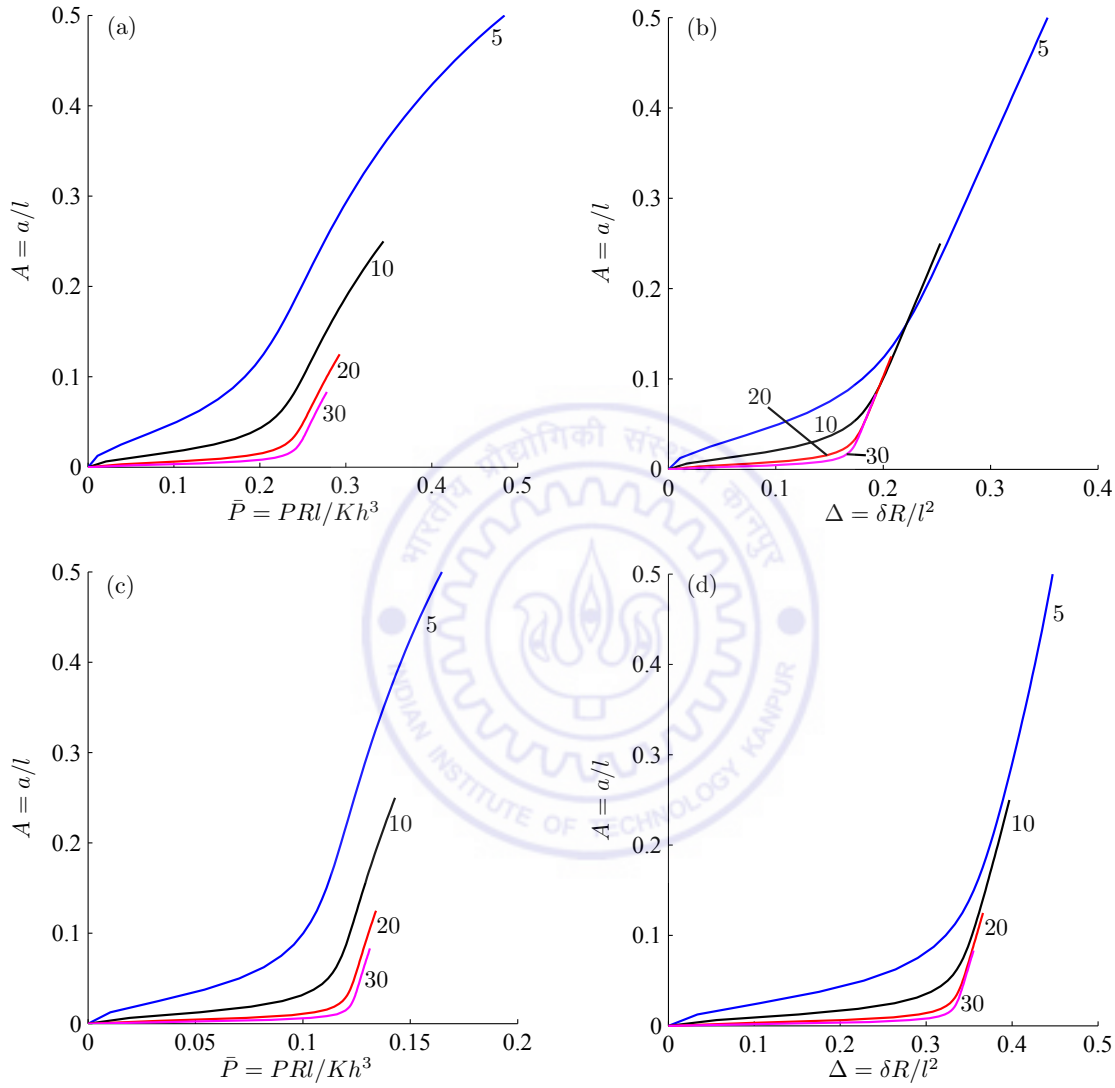

Figure 3.6: Non-adhesive contact of clamped (top row) and simply supported (bottom row) beams. Variation of contact area A with total load $\bar{P}$ and punch's displacement Δ is shown. Different slenderness ratios l/h are considered and these are noted next to their associated curves.

beam wrapping around the punch rapidly with only a small increase in the load or the punch's displacement. However, the plots in Fig. 3.6 do not reflect this aspect well, as l is a common parameter in A, $\bar{P}$, Δ and l/h. At the end of this section we will employ an alternative set of non-dimensional variables which will provide clearer insight.

Next, in Fig. 3.7 we plot the variation of Δ with $\bar{P}$ for various l/h for both clamped and simply supported beams. In Chapter 2, we found that these collapsed onto a single curve. This is not observed in Fig. 3.7. This collapse observed in Chapter 2 was driven by the assumption that displacement at the bottom surface of the beam was given by the displacement of an Euler-Bernoulli beam. The relationship between Δ and $\bar{P}$ for Euler-Bernoulli beams with different l/h is self-similar. However, here, the displacement of the bottom surface is found directly as a solution to the elasticity problem and is distinct from that obtained in Chapter 2.

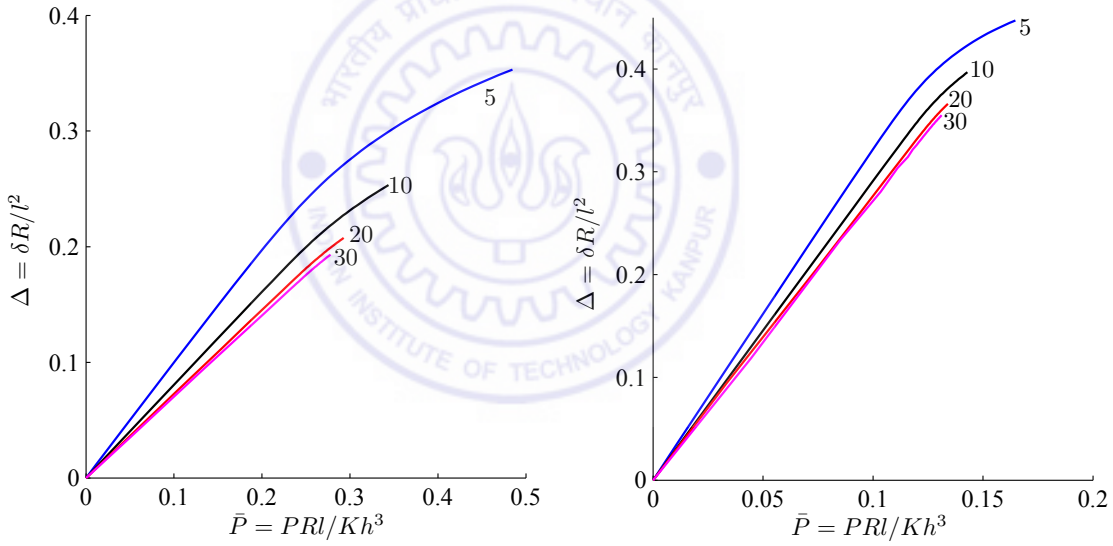

Figure 3.7: Non-adhesive contact of (a) clamped and (b) simply supported beams. Variation of punch's displacement Δ with total load $\bar{P}$ is shown. Several slenderness ratios l/h, as noted next to their associated curves, are considered.

We return to explaining the sudden change of slope observed in the curves of Fig. 3.6. To this end, we follow Maugis (1992) and employ the non-dimensionalized parameters

$$\hat{A} = \frac{AL}{m} = a\left(\frac{K}{\pi w R^2}\right)^{1/3}, \quad \hat{P} = \frac{\bar{P}H^3}{Lm^3} = \frac{P}{\pi w} \quad \text{and} \quad \hat{\Delta} = \frac{\Delta L^2}{m^2} = \delta\left(\frac{K^2}{\pi^2 w^2 R}\right)^{1/3}, \tag{3.54}$$

where $H = h/R$, instead of, respectively, A, P and Δ, to report our results. We set the

adhesion energy $w = 0.02 \times 10^{-3}$ J/mm^2. In the present case of non-adhesive contact w serves only to facilitate non-dimensionalization.

We plot the variation of $\hat{A}$ with $\hat{P}$ and $\hat{\Delta}$ at several l/h in Fig. 3.8. Only clamped beams are considered. The results for simply supported beams are qualitatively similar. The rapid wrapping of the beam is reflected by the sudden increase in A in Fig. 3.8. As slender beams bend easily, this wrapping happens at lower loads for such beams; see Fig. 3.8(a). For the same reason, we observe more displacement in these beams in Fig. 3.8(b). We also demonstrate how an elastic half-space results are obtained by varying the thickness of the beam in Appendix F ; see Figs. F.2(c) and (d).

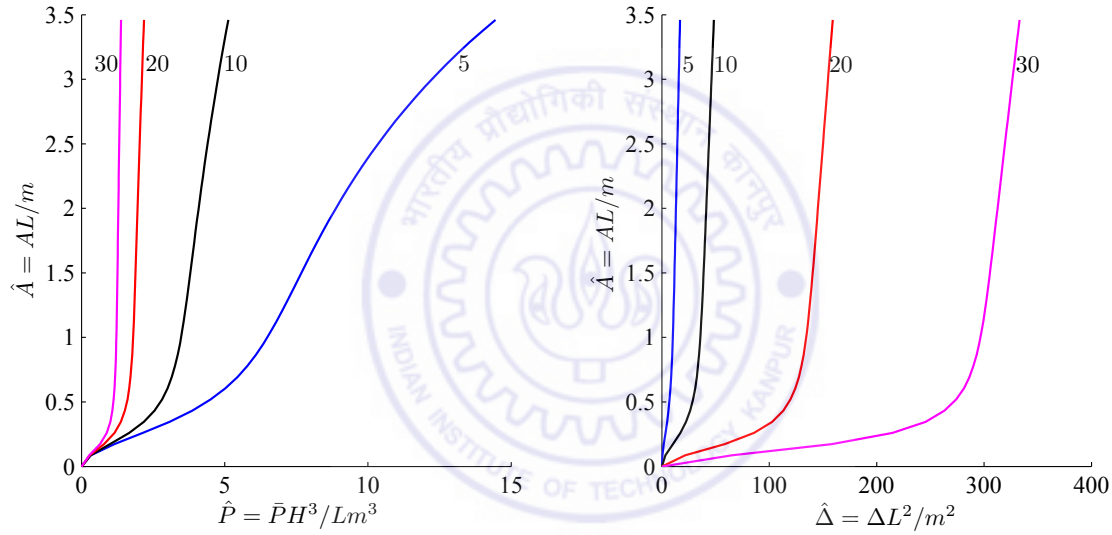

Figure 3.8: Non-adhesive contact of clamped beams. Variation of contact area $\hat{A}$ with (a) total load $\hat{P}$ and (b) punch's displacement $\hat{\Delta}$ is shown. Different slenderness ratios l/h are considered and these are noted next to their associated curves.

3.8 Results: Adhesive contact - JKR approximation

The JKR approximation is recovered when the scaled adhesive strength $\lambda \to \infty$ and the adhesive zone vanishes, i.e. $\bar{c} \to 1$. Hence, equations (3.28) and (3.29) become,

respectively,

$$\Delta - \frac{1}{2}\,\bar{x}^2 A^2 = \frac{8\hat{\gamma}^3}{3\pi}\sum_{n=0}^{N} b_{2n}\mathcal{J}_{2n}^{t}\left(\bar{x}\right) + \frac{1}{\pi\hat{\gamma}}\sum_{n=1}^{M} d_n \mathcal{Q}_n^{t}\left(\bar{x}\right) \tag{3.55}$$

and

$$0 = \frac{8\hat{\gamma}^3}{3\pi}\sum_{n=0}^{N} b_{2n}\mathcal{J}_{2n}^{b}\left(\hat{x}\right) + \frac{\hat{\gamma}}{\pi}\sum_{n=1}^{M} d_n \mathcal{Q}_n^{b}\left(\hat{x}\right). \tag{3.56}$$

The end condition on the contact pressure is determined by the Griffith criterion (3.24). By substituting (3.31) in (3.24), we obtain

$$b_0 + b_2 + \cdots + b_{2N} = -\frac{m}{2\pi L}\left(\frac{l}{h}\right)^3 \frac{\sqrt{6Am}}{L}. \tag{3.57}$$

We now solve (3.55) – (3.57) through the algorithm of Sec. 3.5.

In Fig. 3.9 we plot the variation of the contact area $\hat{A}$ with the load $\hat{P}$ acting on the punch and the displacement $\hat{\Delta}$ of the punch for both clamped and simply supported beams. The slenderness ratio l/h is kept constant, but two different combinations of l and h are investigated. We observe that the curves for same l/h are sensitive to l and h individually and depend *not* only on the slenderness ratio. This was also observed in Chapter 2. This may be traced back to the presence of $L = l/R$ on the right hand side of (3.57). It is easier to explore the dependence of h and l repeatedly by employing $\hat{A}$, $\hat{P}$ and $\hat{\Delta}$ and we do so in Figs. 3.10 and 3.11.

Curves in Fig. 3.10 are obtained for several l/h by varying h while keeping $l = 40$ mm. Beams with high l/h ratio bend easily due to the adhesion, and we observe smaller negative loads $\hat{P}$ and larger negative displacements $\hat{\Delta}$ at a given contact area $\hat{A}$. Note that negative loads and displacements indicate, respectively, tensile force on the punch and the upward bending of beams. From Fig. 3.10 we observe that these slender beams wrap around – as indicated by sudden slope changes in $\hat{A}$ versus $\hat{P}$ and $\hat{\Delta}$ curves – the punch earlier, i.e. at smaller $\hat{P}$. For sufficiently slender beams, the wrapping occurs even when there is no compressive (positive) load on the punch. In these beams the bending resistance is unable to counterbalance adhesive forces. The above features, viz. extent of wrapping and the response to adhesive forces, are, expectedly, heightened in the case of simply supported beams, whose bending resistance is lower.

Finally, we plot the variation of the contact area $\hat{A}$ with the load $\hat{P}$ acting on the punch

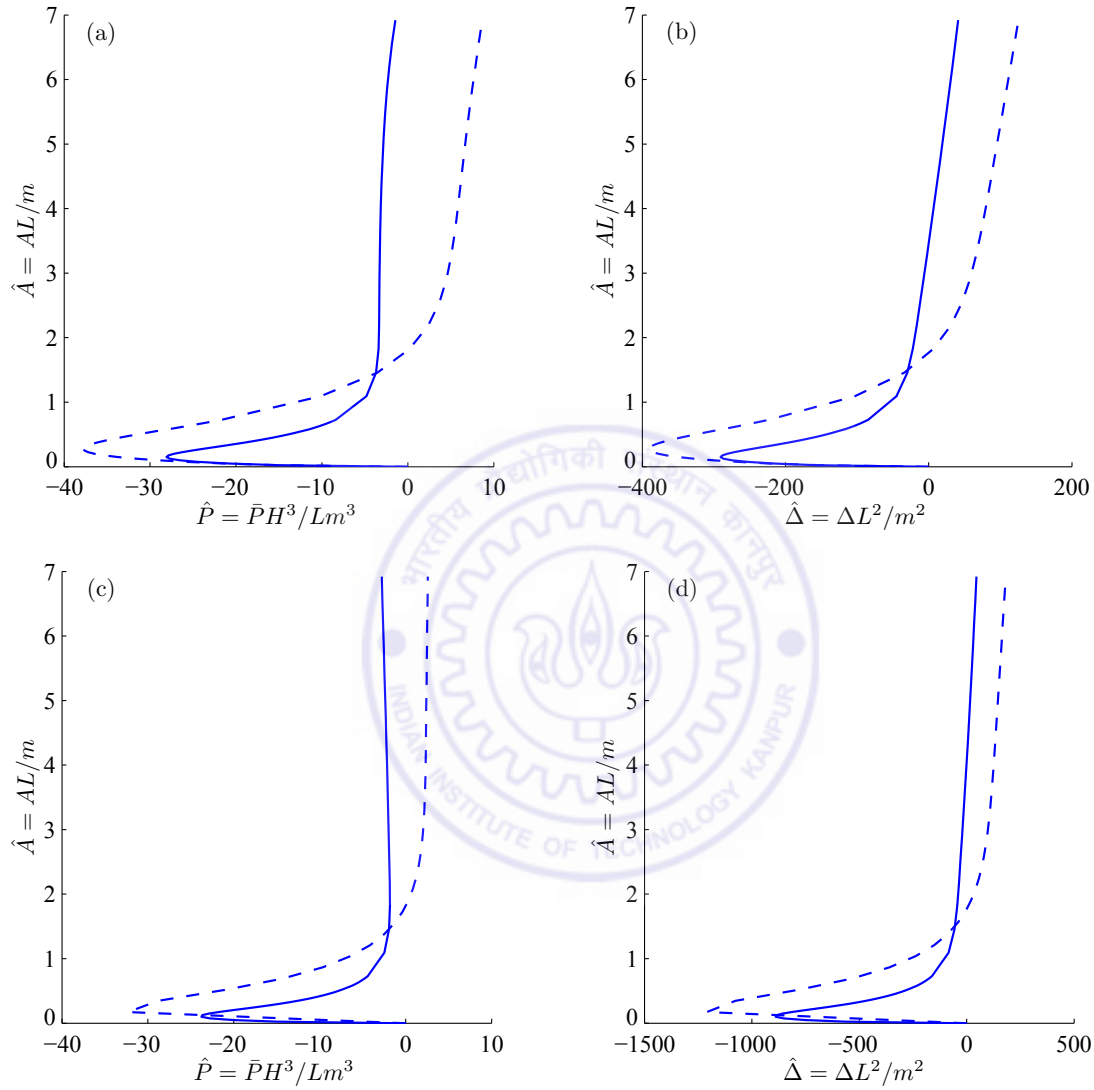

Figure 3.9: Adhesive contact of clamped (top row) and simply supported (bottom row) beams with the JKR approximation. Variation of contact area $\hat{A}$ with the total load $\hat{P}$ are shown in (a) and (c), and the punch's displacement $\hat{\Delta}$ are shown in (b) and (d). The beam's slenderness ratio $l/h = 10$. Solid lines correspond to $l = 40$ mm and $h = 4$ mm, while the dashed line is for a beam with $l = 80$ mm and $h = 8$ mm.

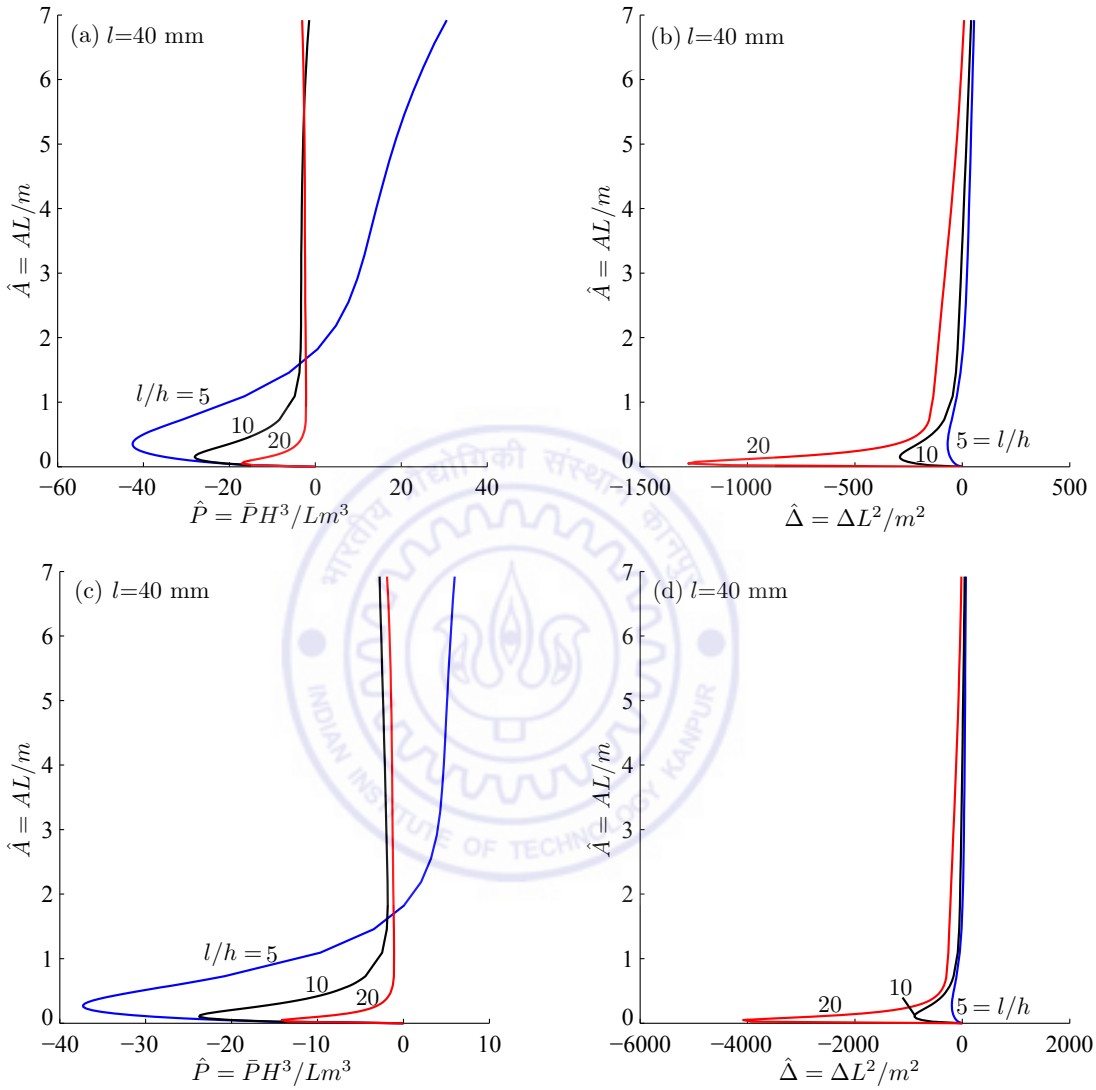

Figure 3.10: Adhesive contact of clamped (top row) and simply supported (bottom row) beams with the JKR approximation. Left column, i.e. (a) and (c), reports the variation of contact area $\hat{A}$ with total load $\hat{P}$, while the right column, i.e. (b) and (d), plots the change of $\hat{A}$ with the punch's displacement $\hat{\Delta}$. Results are obtained by setting $l = 40$ mm and varying h as shown.

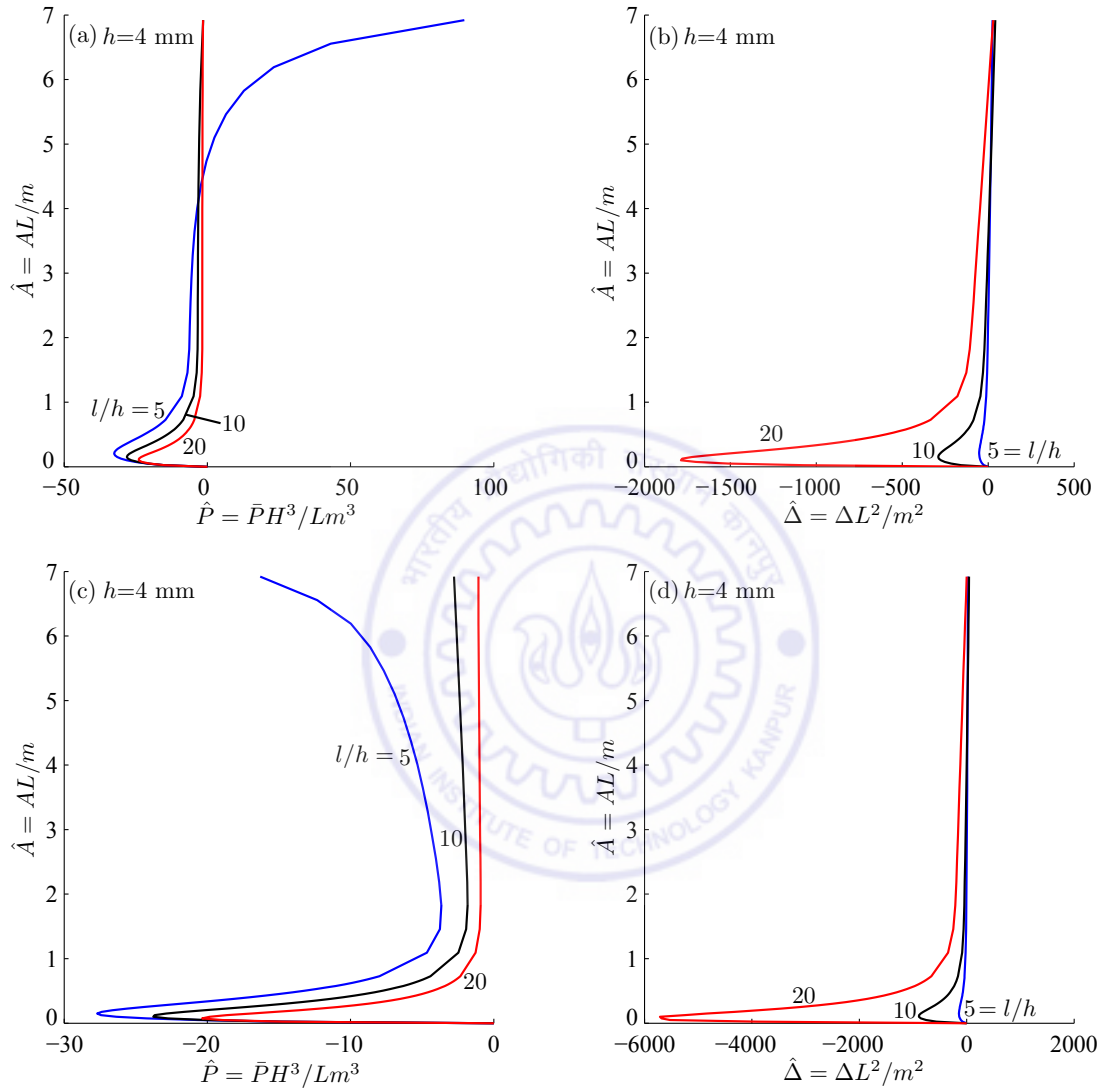

Figure 3.11: Adhesive contact of clamped (top row) and simply supported beams (bottom row) with the JKR approximation. Left column, i.e. (a) and (c), reports the variation of contact area $\hat{A}$ with total load $\hat{P}$, while the right column, i.e. (a) and (c), plots the change of $\hat{A}$ with the punch's displacement $\hat{\Delta}$. Results are obtained by setting $h = 4$ mm and varying l as shown.

and the displacement $\hat{\Delta}$ for several slenderness ratios l/h. We change l and set $h = 4$ mm. The results for both clamped and simply supported beams are shown in Fig. 3.11. Qualitatively Fig. 3.11 is similar in many respects to Fig. 3.10. From Fig. 3.11(c), we observe that, for $\hat{A} \gtrsim 1.5$ in a simply supported beam of $l/h = 5$, the load $\hat{P}$ decreases with the increase in contact area $\hat{A}$. At the same time, the punch's displacement $\hat{\Delta}$ increases; see Fig. 3.11(d). This is explained by the presence of negative (tensile) stresses at the center of the contact area in addition to the very large negative stresses allowed in the contact pressure distribution at the contact edges. The contact area over which these tensile stresses act also increases with the increase in contact area. Hence, the load $\hat{P}$ decreases with the increase in contact area $\hat{A}$.

3.9 Results: Adhesive contact with an adhesive zone model

Finally, we study the behaviour of adhesive beams indented by a rigid cylindrical punch with the help of adhesive-zone models. In these models an adhesive force acts over an adhesive zone of length $d = c - a$ outside the contact area. Here, we model the distribution of the adhesive forces through the Dugdale-Barenblatt model, so that the normal traction on the (extended) beam's top surface is given by (3.9). The contact problem is resolved by solving (3.36) – (3.39) following the solution procedure of Sec. 3.5.

For brevity, we report here the effect of only the adhesive strength λ at a given l and h, as the response to varying l/h is found to be the same as in Sec. 3.8.

In Fig. 3.12 we plot the variation of the contact area $\hat{A}$ with the total load $\hat{P}$ and the displacement $\hat{\Delta}$ for several adhesive strengths λ. We observe that as $\lambda \to 0$ the results approach those obtained for non-adhesive interaction as in Sec. 3.7. At the same time, increasing adhesive strength pushes our results towards those obtained for the JKR approximation in Sec. 3.8.

Next, we study the effect of adhesive strength λ on the adhesive zone size $\bar{d} = \bar{c} - 1$. For this, we plot $\bar{d}$ by varying $\hat{A}$ for several adhesive strengths in Fig. 3.13. From Fig. 3.13, we observe that with increasing λ, $\bar{d}$ goes to zero. We also find that, due to the difference in formulations, the results obtained in this article are quite different from those of Chapter 2 at low to moderate adhesive strengths. At high λ there is not much difference between

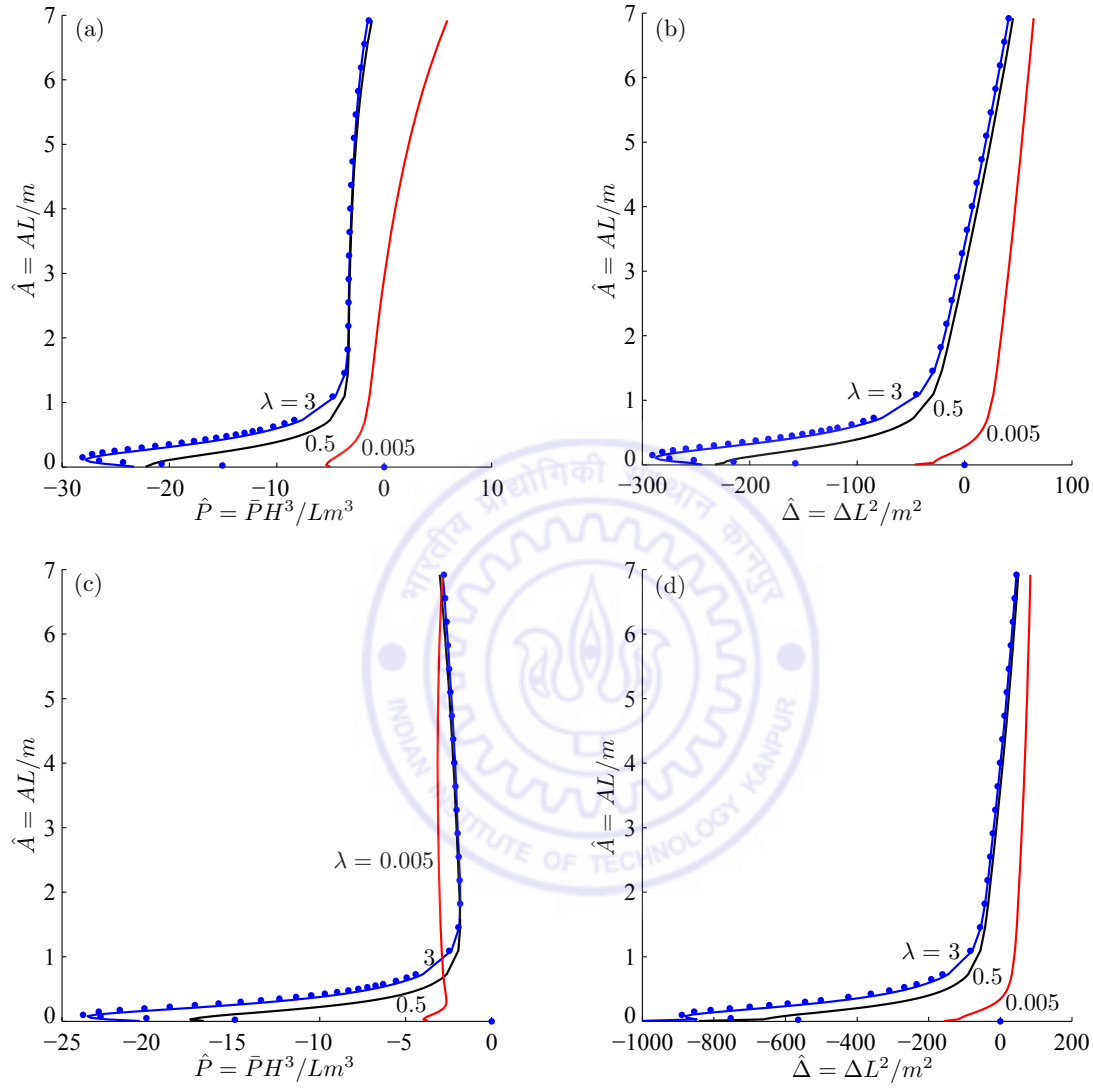

Figure 3.12: Adhesive contact of clamped (top row) and simply supported (bottom row) beams with an adhesive zone model. Variation of contact area $\hat{A}$ with the total load $\hat{P}$ are shown in (a) and (c), and the punch's displacement $\hat{\Delta}$ are shown in (b) and (d). Different adhesive strengths λ are considered and these are indicated next to their associated curves. The beam's thickness $h = 4$ mm and $l = 40$ mm. Filled circles represent the JKR solution for the corresponding beam; cf. Sec. 3.8

the two. Finally, as seen in Chapter 2, varying the slenderness ratio l/h and constraints imposed by end supports do not effect the adhesive zone size much.

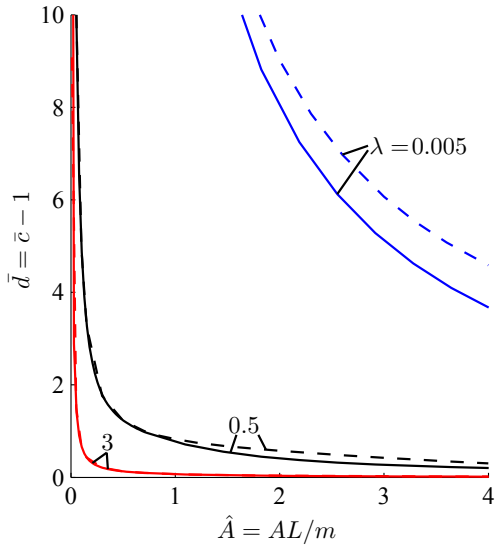

Figure 3.13: Variation of the adhesive zone size $\bar{d}$ with the the contact area $\hat{A}$ at different adhesive strengths λ for a clamped beam. We set l=40 mm and $h = 4$ mm. Solid lines indicate the predictions of the formulation mentioned in this article, while the dotted lines are those obtained from the formulation of the Chapter 2.

3.10 Comparison with Chapter 2

We now compare predictions of the formulation of this chapter with Chapter 2 for both non-adhesive and adhesive contacts. For this, we plot the variation of the contact area $\hat{A}$ with variation in the total load $\hat{P}$ acting on the punch for clamped and simply supported beams as shown in Fig. 3.14. For the non-adhesive beams, we also plot FE results to show the comparison better; see Fig. 3.14(a). From Fig. 3.14(a), we observe that both the semi-analytical formulations predicts the behavior of the beams correctly for small $\hat{A}$. However, with increasing $\hat{A}$, predictions of the current formulation are closer to the FE simulations than those of Chapter 2. Finally, from Fig. 3.14(b), we observe that both the formulations predicts the same behavior in the beams before wrapping in the JKR approximation of the contact. However, for a large portion of the contact area the results of both the formulations predicts the behaviour of the beams differently. Thus, to establish the correctness of these formulations, we need to study the behaviour of the beams experimentally. So, in the next section, we check the experimental feasibility for the indentation in adhesive beams.

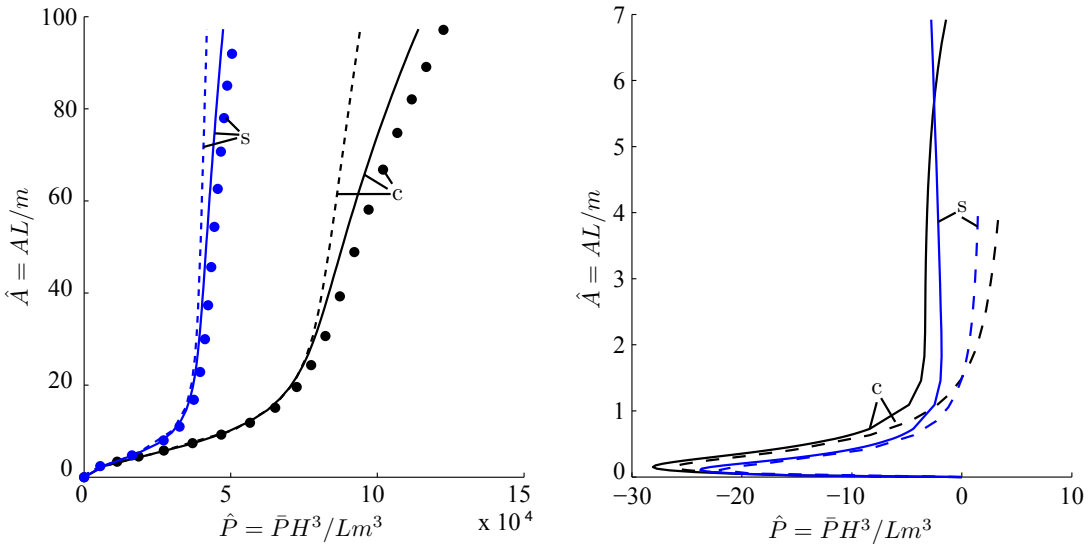

(a) (b)

Figure 3.14: The contact area A is plotted as a function of the total load $\bar{P}$ acting on the punch. (a) Non-adhesive contact of clamped ('c') and simply supported ('s') beams. The beam's slenderness ratio l/h=10. We set $E = 2000$ MPa and $\nu = 0.3$. (b) Adhesive contact of clamped ('c') and simply supported ('s') beams with JKR approximation. We set $h = 4$ mm, $l = 40$ mm, $E = 0.083$ MPa and $\nu = 0.4$. Solid lines are results obtained from the semi-analytical procedure of Sec. 3.4, while the dashed line are results from Chapter 2. Filled circles correspond to FE simulations of Sec. 3.6.

3.11 Experimental validation feasibility for the adhesive contact

In this section, we see the feasibility of conducting the JKR experiments for the beams with our experimental set-up mentioned in Chapter 2. For this purpose, we first obtain predictions for PDMS (poly-dimethyl- siloxane) samples employed in Chapter 2 utilizing the formulations of this chapter and Chapter 2. The PDMS samples were prepared using a 10:1 weight ratio mixture of Sylgard 184 silicone elastomer base and curing agent. We consider clamped beams with fixed half-span $l = 50$ mm and vary the thickness h between 1 mm and 25 mm. The results are shown in Fig. 3.15.

In our experiments, the maximum value of the load P is limited by our micro-weighing balance. From Fig. 3.15, we observe that with a 10:1 PDMS material, we can *not* clearly distinguish the results obtained by the formulation of this chapter and that of Chapter 2. The limitations of the load measuring capability of our micro-weighing balance used in the experimental set-up makes differentiating between the predictions of our current and

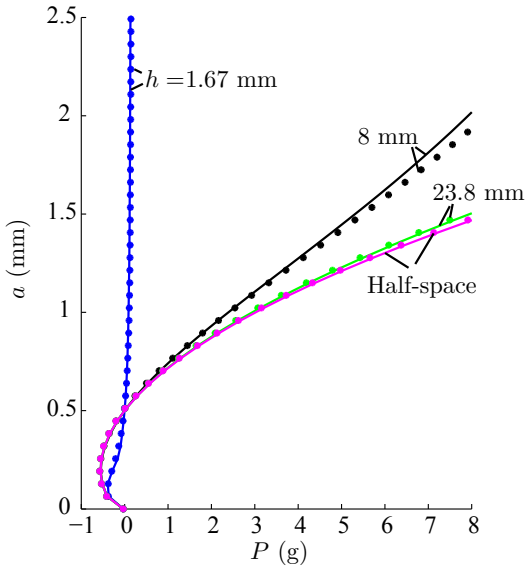

Figure 3.15: Variation of the contact area a (in mm) with the total load P (in g) for adhesive clamped beams with half-span l = 50 mm at several thicknesses h, as noted next to their curves. We set $E = 1.237$ MPa, $W = 27.941$ N/mm. The contact is modeled by the JKR approximation of the contact. Solid lines correspond to theoretical predictions of Chapter 2, while the asterisk represent those of current approach.

previous (Chapter 2) formulations hard. To achieve this with our current experimental set-up requires a softer material with strong adhesive characteristics than PDMS.

3.12 Conclusions

The assumption made in the Chapter 2 about the vertical displacement of the beam's bottom surface limits the range of the corresponding semi-analytical analysis. In this chapter we removed this constraint by solving for the vertical displacement directly, thereby extended the applicability of the formulation. The current formulation modeled the indention of adhesive beam in terms of two coupled Fredholm integral equations of first kind. These dual integral equations were solved through a collocation technique employing series approximations for the unknown contact pressure and bottom surface's vertical displacement. Care should be exercised when selecting the approximating series for the displacement. We then compared our predictions with FE simulations and previously published results for non-adhesive indentation, and found a satisfactory match for a wide range of indentation. Next, we presented the results for JKR approximation and adhesive zone model approximation of the contact. Finally, we studied the experimental feasibility to establish the veracity of the current approach. However, for this we need a softer adhesive material

than the PDMS – which we are in search of.

भारतीय प्रौद्योगिकी संस्थान कानपुर
INDIAN INSTITUTE OF TECHNOLOGY KANPUR

Chapter 4

Conclusions and future scope

4.1 Conclusions

We now briefly present the important conclusions from this study as listed below.

- Solving the boundary value problem for the two-dimensional, plane strain indentation by a rigid circular punch with an adhesive elastic layer resting on its end supports provides two coupled Fredholm integral equations of first kind. The adhesion between the beam and the punch is modeled through an adhesive zone model, that can be conveniently generalized. The coupled integral equations are solved, employing Galerkin or collocation methods, for the unknown contact pressure distribution, displacement of the punch, the adhesive zone size and vertical displacement of the elastic layer's bottom surface.
- When the contact area is not large, the displacement of the bottom surface may be conveniently approximated by that of an Euler-Bernoulli beam's, reducing the problem to one integral equation.

4.2 Future scope

Looking further forward, we envisage:

1. Investigating the possibility of scaling relationships underlying adhesive contact of beams.

2. Formulation of a contact problem which accommodates the possibility of separation under the punch.

3. Extending the contact problem to investigate material and geometric nonlinearities.

4. Modeling beam to beam contact with and without adhesion.

5. Adapting the present technique to three-dimensional axi-symmetric problems of adhesive contact of thin plates.

6. Extensive experiments of adhesive contact of beams.

Appendix A

Calculations using beam theory

In this section, we find the displacement of an Euler-Bernouli beam subjected to a point load at its center and resting on flexible supports, as shown in Fig. A.1.

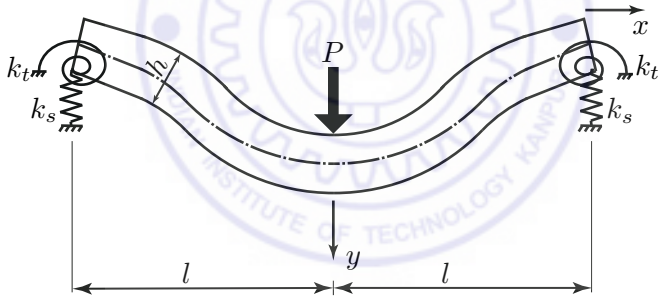

Figure A.1: An Euler-Bernoulli beam on flexible supports acted upon at its center by a concentrated force P.

From Euler-Bernoulli beam theory (Crandall et al., 2008, p. 165, 523, 543) we find

$$EI\,\frac{d^4 v_n\,(x)}{dx^4} = P\langle x\rangle^{-1}, \tag{A.1}$$

where $v_n\,(x)$ is the displacement of the neutral axis (dash-dot line in Fig. A.1) and

$$\langle x\rangle = \begin{cases} x, & x > 0 \\ 0, & x \leq 0. \end{cases}$$

The appropriate boundary conditions are:

$$v_n|_{x=-l} = \frac{P}{2k_s}, \qquad v_n|_{x=l} = \frac{P}{2k_s}, \tag{A.2a}$$

$$k_t \frac{dv_n}{dx}\bigg|_{x=-l} = EI\frac{d^2v_n}{dx^2}\bigg|_{x=-l} \quad \text{and} \quad -k_t\frac{dv_b}{dx}\bigg|_{x=l} = EI\frac{d^2v_n}{dx^2}\bigg|_{x=l}. \tag{A.2b}$$

Identifying the displacement v_b of the beam's bottom surface with v_n, as is done in beam theory, and solving (A.1) and (A.2), provides

$$\begin{aligned} v_b(x) =& \frac{P}{EI}\left\{\frac{1}{6}\langle x\rangle^3 - \frac{1}{12}x^3 - \frac{x^2 l}{8}\left(1+\frac{EI}{k_t l + EI}\right)\right. \\ &\left. + \frac{1}{24}\left(l^3 + 3l^3\frac{EI}{k_t l + EI} + 12\frac{EI}{k_s}\right)\right\}. \end{aligned} \tag{A.3}$$

As the displacement is symmetric in x, we henceforth employ $v_b(x)$ for $x \geq 0$ in our calculations.

Non-dimensionalizing (A.3) following Sec. 2.3, we obtain

$$\vartheta_b(\hat{\tau}) = \frac{4\bar{P}}{3\bar{I}(1-\nu^2)}\left\{\frac{\langle\hat{\tau}\rangle^3}{6} - \frac{\hat{\tau}^3}{12} - \frac{\hat{\tau}^2}{8}\left(1+K_t^{-1}\right) + \frac{1}{24}\left(1+3K_t^{-1}+12K_s^{-1}\right)\right\}, \tag{A.4}$$

where $K_t^{-1} = EI/(k_t l + EI) = (1+k_t^f)^{-1}$ and $K_s^{-1} = EI/k_s l^3 = k_s^{f\,-1}$.

When we extended the beam to infinity – cf. Fig. 2.2(b) – the displacement of the overhang, i.e. $\hat{\tau} > 1$, is given by

$$\vartheta_b(\hat{\tau}) = \vartheta_b(\hat{\tau})|_{\hat{\tau}=1} + \frac{d\vartheta_b(\hat{\tau})}{d\hat{\tau}}\bigg|_{\hat{\tau}=1}(\hat{\tau}-1). \tag{A.5}$$

Calculating the displacement and slope at $\hat{\tau} = 1$ from (A.4) and substituting in (A.5) yields

$$\vartheta_b(\hat{\tau}) = \frac{4\bar{P}}{3\bar{I}(1-\nu^2)}\left[\frac{1}{2K_s} - \frac{1}{4K_t}(\hat{\tau}-1)\right], \quad \hat{\tau} > 1. \tag{A.6}$$

Finally, the displacement of the extended beam's bottom surface over its entire length may be written as

$$\vartheta_b(\hat{\tau}) = \frac{4\bar{P}}{3\bar{I}(1-\nu^2)}\,\vartheta_p(\hat{\tau}), \tag{A.7}$$

where

$$\vartheta_p(\hat{\tau}) = \begin{cases} \left\{\hat{\tau}^3/12 - \hat{\tau}^2\left(1 + K_t^{-1}\right)/8 + \left(1 + 3K_t^{-1} + 12K_s^{-1}\right)/24\right\}, & 0 \le \hat{\tau} \le 1 \\ \left\{K_s^{-1}/2 - K_t^{-1}(\hat{\tau} - 1)/4\right\}, & \hat{\tau} > 1. \end{cases} \tag{A.8}$$

Finally, we evaluate the Fourier transform

$$\hat{\vartheta}_b(\hat{\omega}) = \int_{-\infty}^{\infty} \vartheta_b(\hat{\tau}) \cos(\hat{\omega}\hat{\tau})\, d\hat{\tau} = 2\int_{0}^{\infty} \vartheta_b(\hat{\tau}) \cos(\hat{\omega}\hat{\tau})\, d\hat{\tau}, \tag{A.9}$$

which is required in (2.23). The above integrals are typically undefined, as $\vartheta(\hat{\tau})$ is unbounded once the beam is extended to infinity, unless the beam is clamped. To overcome this, we invoke St. Venant's principle by which, displacement of the overhang, sufficiently far away from the supports, may be modified without exerting any significant influence on the displacement and stresses in the portion of the beam lying within the supports. To this end, we modify the displacement of the beam's bottom surface by introducing

$$\vartheta_b^M(\hat{\tau}) = \vartheta_b(\hat{\tau}) \cdot W(\hat{\tau}), \tag{A.10}$$

with

$$W(\hat{\tau}) = \begin{cases} 1, & \text{for } \hat{\tau} \le \hat{l}_1, \\ w_2(\hat{\tau}), & \text{for } \hat{l}_1 < \hat{\tau} < \hat{l}_2 \\ 0, & \text{for } \hat{\tau} \ge \hat{l}_2, \end{cases}, \tag{A.11}$$

where

$$w_2(\hat{\tau}) = \frac{\exp\left\{-1/\left(\hat{l}_2 - \hat{\tau}\right)^2\right\}}{\exp\left\{-1/\left(\hat{l}_2 - \hat{\tau}\right)^2\right\} + \exp\left\{-1/\left(\hat{\tau} - \hat{l}_1\right)^2\right\}}, \tag{A.12}$$

and $\hat{l}_1$ and $\hat{l}_2$ locate points on the beam that are far away from its supports, i.e. $\hat{l}_2 > \hat{l}_1 \gg 1$ (see B). The function $W(\hat{\tau})$ is a *mollifier*, see Muthukumar (2016), and is infinitely differentiable everywhere.

The mollified displacement $\vartheta_b^M(\hat{\tau})$ in (A.10) is now utilized in (A.9) to compute the Fourier transforms. Thus,

$$\hat{\vartheta}_b(\hat{\omega}) \approx 2\int_{0}^{\infty} \vartheta_b^M(\hat{\tau}) \cos(\hat{\omega}\hat{\tau})\, d\hat{\tau} = 2\int_{0}^{\infty} \vartheta_b(\hat{\tau})\, W(\hat{\tau}) \cos(\hat{\omega}\hat{\tau})\, d\hat{\tau}. \tag{A.13}$$

Evaluating the above integral and replacing the total load $\bar{P}$ from (2.28) in the resulting

equation provides

$$\hat{\vartheta}_b(\hat{\omega}) = \left\{ \frac{4\pi b_0}{3\bar{I}(1-\nu^2)} - \frac{4\lambda A m \bar{c}}{3\hat{\gamma}^3 \bar{I} L (1-\nu^2)} \right\} \hat{\vartheta}_p(\hat{\omega}), \tag{A.14}$$

where

$$\hat{\vartheta}_p(\hat{\omega}) = 2 \int_0^\infty \vartheta_p(\hat{\tau}) W(\hat{\tau}) \cos(\hat{\omega}\hat{\tau}) \, d\hat{\tau}. \tag{A.15}$$

Setting $k_t^f \to \infty$ and $k_s^f \to \infty$, we obtain results for a clamped beam, while those for a simply supported beam are found by taking $k_t^f \to 0$ and $k_s^f \to \infty$.

Finally, we write

$$\frac{1}{\pi\hat{\gamma}} \hat{\vartheta}_b(\hat{\omega}) = \left\{ \frac{4b_0}{3\bar{I}(1-\nu^2)\hat{\gamma}} - \frac{4\lambda A m \bar{c}}{3\pi\hat{\gamma}^4 \bar{I} L (1-\nu^2)} \right\} \hat{\vartheta}_p(\hat{\omega}). \tag{A.16}$$

Appendix B

Selection of $\hat{l}_1$ and $\hat{l}_2$

Here, we demonstrate convergence of our contact pressures, employing our theoretical model of Chapter 2, for an indentation in a simply supported beam by varying $\hat{l}_1$ and $\hat{l}_2$. In Fig. B.1, we plot contact pressure profiles for three different combinations of $\hat{l}_1$ and $\hat{l}_2$. We observe that the variation in contact pressure profiles is negligible at our choices of $\hat{l}_1$ and $\hat{l}_2$. So, in all our theoretical models we employ $\hat{l}_1 = 2$ and $\hat{l}_2 = 3$.

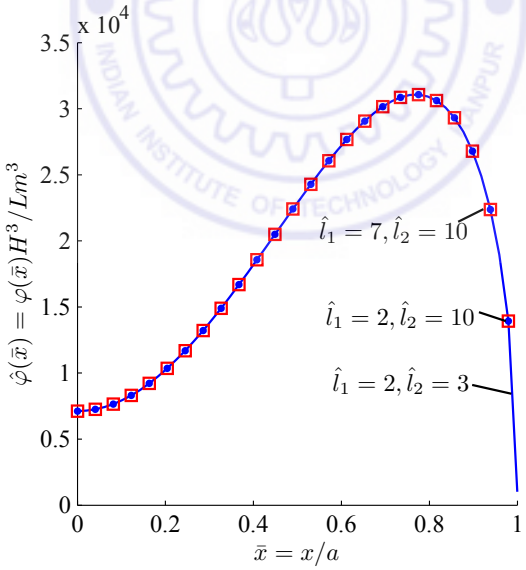

Figure B.1: The contact pressure profiles are plotted for a simply supported beam indentation at $a/h = 1.25$. Three different combination of $\hat{l}_1$ and $\hat{l}_2$, as noted next to their curves, are employed. The beam's thickness $h = 4$ mm and half-span $l = 40$ mm. We set $E = 2000$ MPa and $\nu = 0.3$.

Appendix C

Vertical displacement of the beam's top surface ($V(\xi, 0)$) and normal traction at its bottom surface ($S_{yy}(\xi, h)$) in Fourier space

We begin with finding solutions to the Navier equations in Fourier space. The Navier equations describing the plane strain indention are

$$\frac{2(1-\nu)}{1-2\nu}\frac{\partial^2 u}{\partial x^2} + \frac{\partial^2 u}{\partial y^2} + \frac{1}{1-2\nu}\frac{\partial^2 v}{\partial x \partial y} = 0 \tag{C.1a}$$

and

$$\frac{\partial^2 v}{\partial x^2} + \frac{2(1-\nu)}{1-2\nu}\frac{\partial^2 v}{\partial y^2} + \frac{1}{1-2\nu}\frac{\partial^2 u}{\partial x \partial y} = 0, \tag{C.1b}$$

where u and v represent the displacements in horizontal and vertical directions. Taking the Fourier transform of the above with respect to x we obtain

$$\frac{d^2 U}{dy^2} - \frac{i\,\xi}{1-2\nu}\frac{dV}{dy} - \frac{2(1-\nu)}{1-2\nu}\xi^2 U = 0 \tag{C.2a}$$

and

$$\frac{2(1-\nu)}{1-2\nu}\frac{d^2 V}{dy^2} - \frac{i\,\xi}{1-2\nu}\frac{dU}{dy} - \xi^2 V = 0, \tag{C.2b}$$

where with

$$U(\xi, y) = \int_{-\infty}^{\infty} u(x, y)\, e^{i\xi x} dx, \quad V(\xi, y) = \int_{-\infty}^{\infty} v(x, y)\, e^{i\xi x} dx,$$

We now guess the solutions to the above ordinary differential equations (ODE) as

$$U = A\, e^{sy} \quad \text{and} \quad V = B\, e^{sy}, \tag{C.3}$$

where A and B are unknown constants. These may be obtained by satisfying the boundary conditions. Substituting the above into the (C.2) yeilds

$$\left[s^2 - \frac{2(1-\nu)}{1-2\nu}\xi^2\right] A - \frac{i\,\xi s}{1-2\nu} B = 0 \tag{C.4a}$$

and

$$-\frac{i\,\xi s}{1-2\nu} A + \left[\frac{2(1-\nu)}{1-2\nu} s^2 - \xi^2\right] B = 0, \tag{C.4b}$$

From the above, for the non-trivial solutions to exist, we should have

$$\begin{vmatrix} s^2 - \frac{2(1-\nu)}{1-2\nu}\xi^2 & -\frac{i\,\xi s}{1-2\nu} \\ -\frac{i\,\xi s}{1-2\nu} & \frac{2(1-\nu)}{1-2\nu} s^2 - \xi^2 \end{vmatrix} = 0. \tag{C.5}$$

Now solving the above for s provides

$$s = \pm\, \xi \tag{C.6}$$

Here $s = \xi$ and $s = -\xi$ are repeated roots, and at these roots we obtain, respectively,

$$B^+ = i\, A^+ \quad \text{and} \quad B^- = -i\, A^-. \tag{C.7}$$

As we obtained the repeated roots for s, we now guess

$$U = C\, e^{sy} + D\, y\, e^{sy} \quad \text{and} \quad V = E\, e^{sy} + F\, y\, e^{sy}, \tag{C.8}$$

where C, D, E and F are unknown constants, to be solutions for (C.2). Again substituting these guess solutions into (C.2) and solving the resulting set of equations for E and F in

terms of C and D at $s = \xi$ and $s = -\xi$ yields, respectively,

$$E^+ = iC^+ - \frac{i\kappa}{\xi} D^+, \qquad F^+ = iD^+ \tag{C.9a}$$

and

$$E^- = -iC^- - \frac{i\kappa}{\xi} D^-, \qquad F^- = -iD^-, \tag{C.9b}$$

where $\kappa = 3 - 4\nu$. Employing (C.3) and (C.8), the ode solutions may be written as

$$U = \left(A^+ + C^+ + D^+ y\right) e^{\xi y} + \left(A^- + C^- + D^- y\right) e^{-\xi y} \tag{C.10a}$$

and

$$V = \left(B^+ + E^+ + F^+ y\right) e^{\xi y} + \left(B^- + E^- + F^- y\right) e^{-\xi y} \tag{C.10b}$$

Employing (C.7) and (C.9) we modify (C.10) to

$$U = \left(a_1 + a_2 y\right) e^{\xi y} + \left(b_1 + b_2 y\right) e^{-\xi y} \tag{C.11a}$$

and

$$V = \left(a_3 + i a_2 y\right) e^{\xi y} + \left(b_3 - i b_2 y\right) e^{-\xi y} \tag{C.11b}$$

where

$$\begin{gathered} a_1 = A^+ + C^+, \quad a_2 = D^+, \quad b_1 = A^- + C^-, \quad b_2 = D^-, \\ a_3 = iA^+ + iC^+ - \frac{i\kappa}{\xi} D^+ \quad \text{and} \quad b_3 = -iA^- - iC^- - \frac{i\kappa}{\xi} D^-. \end{gathered} \tag{C.12}$$

Writing a_2 and b_2 in terms of a_1, a_3 and b_1, b_3 give

$$a_2 = \left(a_1 + i a_3\right) \frac{\xi}{\kappa} \quad \text{and} \quad b_2 = -\left(b_1 - i b_3\right) \frac{\xi}{\kappa}. \tag{C.13}$$

Employing the above, we may write (C.11) as

$$U\left(\xi, y\right) = \left(a_1 + \left(a_1 + i a_3\right) \frac{\xi y}{\kappa}\right) e^{\xi y} + \left(b_1 - \left(b_1 - i b_3\right) \frac{\xi y}{\kappa}\right) e^{-\xi y} \tag{C.14a}$$

and

$$V\left(\xi, y\right) = \left(a_3 + i\left(a_1 + i a_3\right) \frac{\xi y}{\kappa}\right) e^{\xi y} + \left(b_3 + i\left(b_1 - i b_3\right) \frac{\xi y}{\kappa}\right) e^{-\xi y}. \tag{C.14b}$$

Rearranging the above we obtain the solutions for the horizontal and vertical displacement in the Fourier space as

$$U(\xi, y) = (\kappa a_1 + \xi y (a_1 + i a_3)) e^{\xi y} + (\kappa b_1 - \xi y (b_1 - i b_3)) e^{-\xi y} \tag{C.15}$$

and $$V(\xi, y) = (\kappa a_3 + i\xi y (a_1 + i a_3)) e^{\xi y} + (\kappa b_3 + i\xi y (b_1 - i b_3)) e^{-\xi y} \tag{C.16}$$

with unknown constants a_1, a_3, b_1, and b_3. These constants are obtained by applying the boundary conditions, which in Fourier space are

$$\text{at } y = 0: \quad S_{\xi y} = 0, \quad S_{yy} = \bar{P}_c(\xi), \tag{C.17a}$$

$$\text{at } y = h: \quad S_{\xi y} = 0, \quad V = \bar{v}_b(\xi), \tag{C.17b}$$

with

$$\begin{aligned} S_{\xi y} &= \frac{E}{2(1+\nu)} \left(\frac{d}{dy} U - i\xi V \right), \\ S_{yy} &= \frac{E}{(1+\nu)} \left(\frac{d}{dy} V + \frac{\nu}{1-2\nu} \left(-i\xi U + \frac{d}{dy} V \right) \right), \\ \bar{P}_c(\xi) &= \int_{-\infty}^{\infty} -P_c(x) e^{i\xi x} dx \quad \text{and} \quad \bar{v}_b(\xi) = \int_{-\infty}^{\infty} v_b(x) e^{i\xi x} dx. \end{aligned}$$

With this, we find the vertical displacement of the top surface in Fourier space to be

$$V(\xi, 0) = -\frac{2\bar{P}_c(\xi)}{E^*} \frac{\sinh^2 \xi h}{\xi (\xi h + \sinh \xi h \cosh \xi h)} + \bar{v}_b(\xi) \frac{\sinh \xi h + \xi h \cosh \xi h}{\xi h + \sinh \xi h \cosh \xi h},$$

and the normal traction at the bottom layer in Fourier space to be

$$S_{yy}(\xi, h) = \bar{P}_c(\xi) \frac{\sinh \xi h + \xi h \cosh \xi h}{\xi h + \sinh \xi h \cosh \xi h} + E^* \bar{v}_b(\xi) \frac{\xi}{2} \frac{\sinh^2 \xi h - \xi^2 h^2}{\xi h + \sinh \xi h \cosh \xi h},$$

where $E^* = E/(1-\nu^2)$.

Appendix D

Evaluation of the integrals $\alpha_n(\bar{\omega})$

We recall from (2.27) in Sec. 2.4 that

$$\alpha_n(\bar{\omega}) = \int_{-1}^{1} \frac{1}{\sqrt{(1-\bar{\tau}^2)}} T_n(\bar{\tau}) \cos(\bar{\omega}\tau) \; d\bar{\tau}. \tag{D.1}$$

We now compute these integrals explicitly. First, consider odd n. For this, the integrand is an odd function so that

$$\alpha_{2n-1}(\bar{\omega}) = 0. \tag{D.2}$$

Next, evaluating (D.1) for even n we obtain the first few α_n as

$$\begin{aligned}
\alpha_0(\bar{\omega}) =& \pi \, \mathrm{J}(0, \bar{\omega}), \\
\alpha_2(\bar{\omega}) =& \pi \, \mathrm{J}(0, \bar{\omega}) - \frac{2\,\pi \, \mathrm{J}(1, \bar{\omega})}{\bar{\omega}}, \\
\alpha_4(\bar{\omega}) =& \pi \, \mathrm{J}(0, \bar{\omega}) - \frac{8\,\pi \, \mathrm{J}(1, \bar{\omega})}{\bar{\omega}} - \frac{24\,\pi \, \mathrm{J}(0, \bar{\omega})}{\bar{\omega}^2} + \frac{48\,\pi \, \mathrm{J}(1, \bar{\omega})}{\bar{\omega}^3} \\
\text{and} \qquad \alpha_6(\bar{\omega}) =& \pi \, \mathrm{J}(0, \bar{\omega}) - \frac{18\,\pi \, \mathrm{J}(1, \bar{\omega})}{\bar{\omega}} - \frac{144\,\pi \, \mathrm{J}(0, \bar{\omega})}{\bar{\omega}^2} + \frac{768\,\pi \, \mathrm{J}(1, \bar{\omega})}{\bar{\omega}^3} \\
& + \frac{1920\,\pi \, \mathrm{J}(0, \bar{\omega})}{\bar{\omega}^4} - \frac{3840\,\pi \, \mathrm{J}(1, \bar{\omega})}{\bar{\omega}^5},
\end{aligned} \tag{D.3}$$

where $\mathrm{J}(n, \bar{\omega})$ are the Bessel's functions of the first kind of order n. Employing the recurrence relation (Polyanin and Manzhirov, 2008, p. 1016),

$$\mathrm{J}(n+1, \bar{\omega}) = \frac{2n}{\bar{\omega}} \mathrm{J}(n, \bar{\omega}) - \mathrm{J}(n-1, \bar{\omega}),$$

we rewrite (D.3) as

$$\alpha_2(\bar{\omega}) = -\pi\, \mathrm{J}(2, \bar{\omega}), \quad \alpha_4(\bar{\omega}) = \pi\, \mathrm{J}(4, \bar{\omega}) \quad \text{and} \quad \alpha_6(\bar{\omega}) = -\pi\, \mathrm{J}(6, \bar{\omega}).$$

In general, it is possible to show that

$$\alpha_{2n}(\bar{\omega}) = (-1)^n\, \pi\, \mathrm{J}(2n, \bar{\omega}). \tag{D.4}$$

Appendix E

Finite element model

In this work, we compared our theoretical predictions for *non*-adhesive indentation with finite element (FE) computations. For this we employed the representative model shown in Fig. E.1. As the indentation is symmetric about $x = 0$, we consider only the left half of the beam with symmetric boundary conditions at $x = 0$. Thus, the load acting on the punch is $P/2$. We have already discussed the FE model of the beam and the punch in Secs. 2.5 and 3.6. The contact interaction between the punch and the beam is modeled using the frictionless, hard-contact model in ABAQUS; see ABAQUS (2011).

We now discuss the FE modeling of the end supports. The end supports are modeled as elastic layers, represented as B_1 (bottom) and B_2 (top) in Fig. E.1, with Young's modulus $E_b = 200 \times 10^6$ MPa and Poisson's ration $\nu_b = 0.3$. The length and thickness of the support layer are considered as $b = l/8$ and $h/16$. One end of these layers interacts with the beam, while the other end is rigidly fixed, i.e. horizontal and vertical displacements are zero, and rotation is completely restricted. The interaction of these layers' surfaces with the beam's top and bottom surfaces are modeled using frictionless, hard-contact model in ABAQUS. Thus, these end supports act as smooth bearings for the beam at its ends. While performing computations for clamped beam, we keep the top and bottom bearings, and while modeling the simply supported beam, we remove the top bearing.

Finally, we discuss the details of the mesh that is employed in our FE computations. Meshing is done using the in-built algorithms of ABAQUS. For this we have to specify the details for seeding, mesh controls and element types.

For the beam seeding on the top and bottom edges are done using 600 *elements* with a

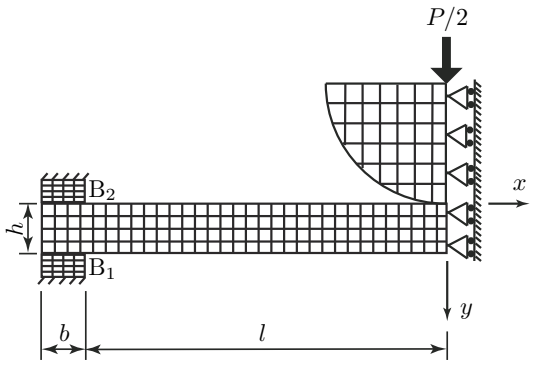

Figure E.1: Finite element model of a non-adhesive beam indention by a cylindrical punch.

single bias ratio of 50, with the smaller elements being near the contact. The vertical edges of the beam are seeded with 20 number of *elements* and *single bias ratio*, where the smaller elements are nearer to the top surface of the beam, of five. *Quadratic* and *structured* mesh is generated employing the *Minimize the mesh control transition algorithm*. For the punch we start with seeding the *part* with an *approximate global size* of 5, *curvature control* of 0.1 and the *minimum size control* is done by keeping the *fraction of global size* at 0.1. *Quadratic* and *free* mesh is generated using the *advancing front algorithm*. The end supports are seeded with an *approximate global size* of 1 and the *curvature control* of 0.1. The *minimum size control* is done by setting the *fraction of global size* to 0.1. The mesh controls are kept the same as that of the punch. We used standard, quadratic plane strain elements with reduced integration for beam, punch and end supports.

Appendix F

Additional results: 1

Here, we present our theoretical predictions of Chapter 2 and Chapter 3 for differently thick non-adhesive clamped beams using the following non-dimensional parameters:

$$\hat{A} = \frac{AL}{m} = a\left(\frac{K}{\pi w R^2}\right)^{1/3}; \quad \hat{P} = \frac{\bar{P}H^3}{Lm^3} = \frac{P}{\pi w}; \quad \hat{\Delta} = \frac{\Delta L^2}{m^2} = \delta\left(\frac{K^2}{\pi^2 w^2 R}\right)^{1/3};$$
$$\hat{\varphi}\left(\bar{\tau}\right) = \varphi\left(\bar{\tau}\right)\frac{H^3}{Lm^3} = \frac{a\,p\left(\bar{\tau}\right)}{\pi w}; \quad H = \frac{h}{R}.$$

The Young's modulus and Poisson's ratio of the beam are taken as $E = 0.083$ MPa and $\nu = 0.4$, respectively. The beam's length is fixed at $l = 40$ mm, and the radius of the punch is considered as $R = 225$ mm.

The pressure profiles for various thicknesses H are shown in Fig. F.1. With increasing thickness h, the beam's bending stiffness (EI) increases. Thus, the pressure profiles shift upwards with increasing H and, finally, approach the half-space solution. We note that the difference in the pressure profiles for $H = 1$ and $H = 10$ is very small, and the corresponding curves fall almost on top of the Hertzian solution found for an elastic half-space.

Next the total load acting on the punch $\hat{P}$ and the displacement $\hat{\Delta}$ of the punch are plotted against the contact area $\hat{A}$ in Fig. F.2 for clamped beams with different thicknesses H. Increasing the thickness makes the beam more resistant to bending. Thus, thicker beams require more load compared to thinner beams to achieve the same contact area. Hence, the curves in Fig. F.2(a) bend rightwards until they coincide with the half-space solution. Here again, the difference in the curves for $H = 1$, $H = 10$ and the half-space is very small.

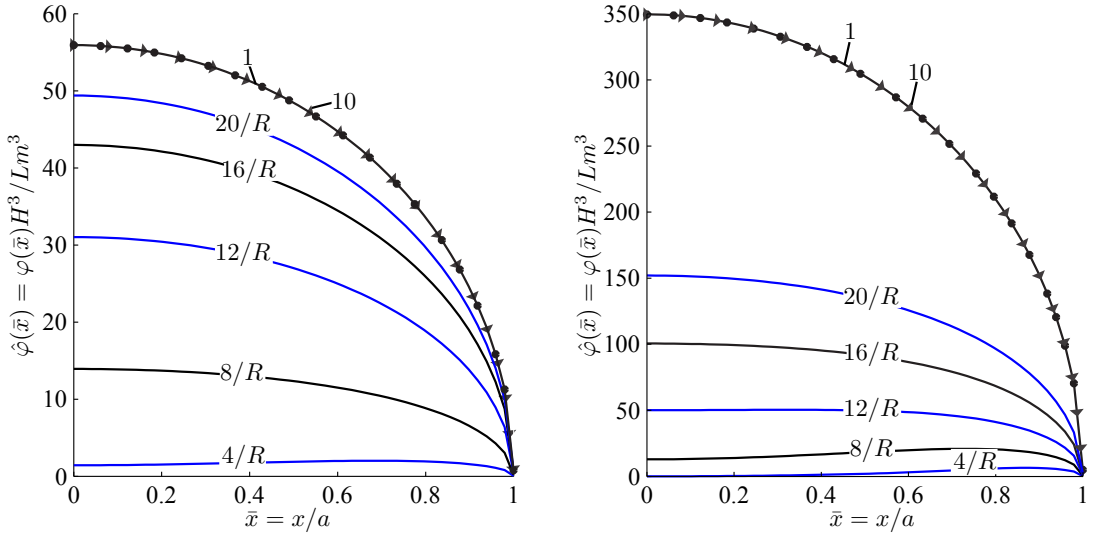

(a) (b)

Figure F.1: Contact pressures in a clamped beam for different H (a) at $\hat{A} = 1.384$ ($a = 4$ mm) employing the procedure outlined in Chapter. 2 and (b) at $\hat{A} = 3.46$ ($a = 10$ mm) following the theoretical model of Chapter. 3. Black dots are the Hertzian solution obtained for an elastic half-space.

Similarly, the punch's displacement $\hat{\Delta}$ is less for thick beams, as they have more bending stiffness. Therefore, the curves in Fig. F.2(b) shift leftwards with increasing thickness. For small H, the contribution of the beam's bending to $\hat{\Delta}$ is significant. However, this contribution reduces as H increases. For $H = 1$ and $H = 10$ the curves are close to the half-space solution–in which $\hat{\Delta}$ is estimated with respect to a point at a distance $d = 2H$ below the punch; see Dalmeya et al. (2012, Eq. 39c). The displacement due to bending in $H = 1$ and $H = 10$ beams is negligible ($v_b \approx 0$). Hence, these beams respond in a manner similar to a smooth, elastic, thick layer resting on a frictionless rigid surface (unbonded elastic layer). This is confirmed by the close match in Fig. F.2(b) of the results for $H = 1$ and $H = 10$ with those of an unbonded elastic layer–these are obtained by taking $v_b = 0$ in the integral equation.

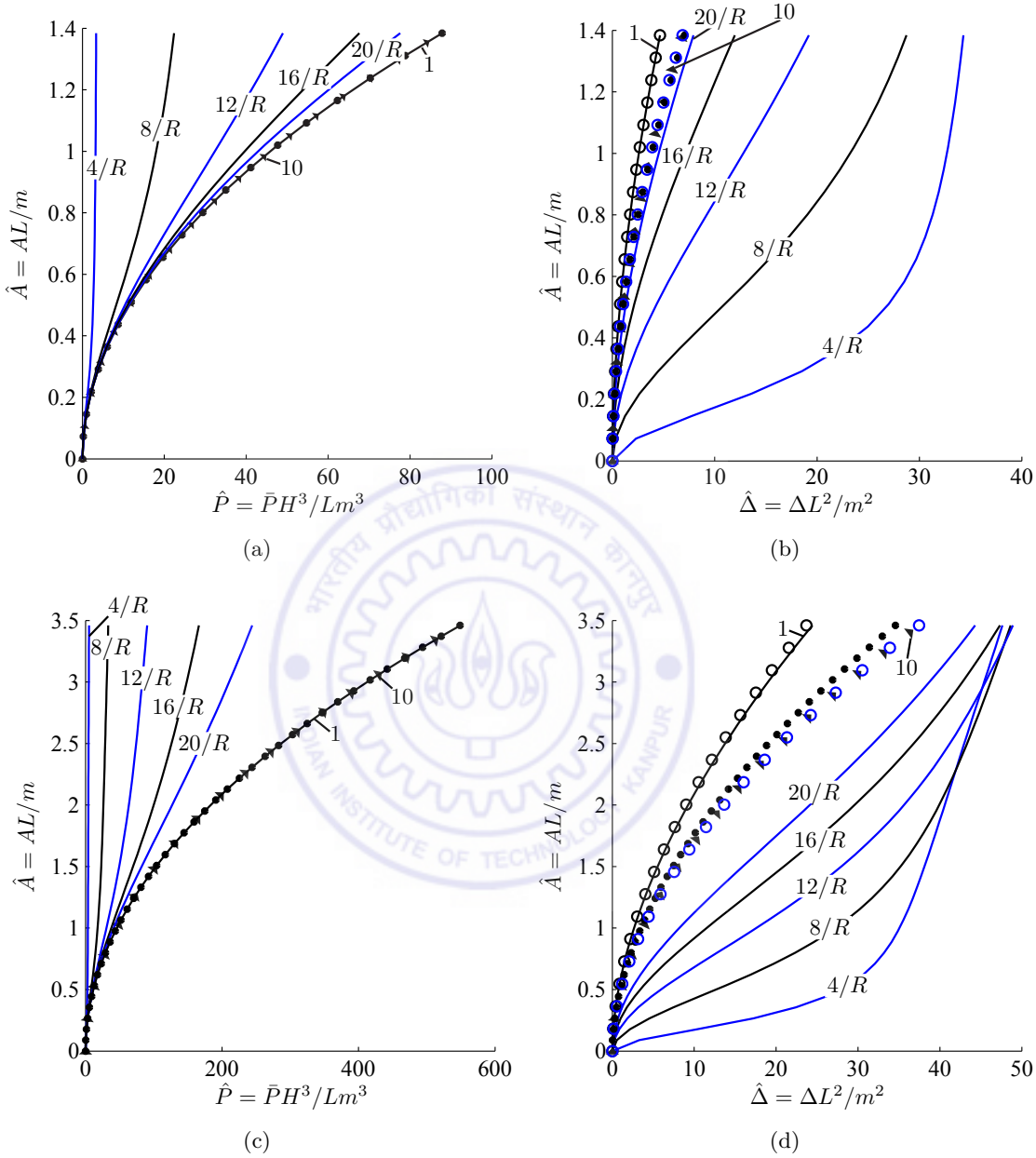

Figure F.2: Non-adhesive contact of clamped beams. The variation of contact area $\hat{A}$ is plotted, following the procedure of Chapter 2 (top row) and Chapter 3 (bottom row), by varying the total load $\hat{P}$ and punch displacement $\hat{\Delta}$ for different H as noted on their curves. Black dots represent Hertzian solution for an elastic half-space. The open circles on $H = 1$ and $H = 10$ lines in $\hat{A}$ versus $\hat{\Delta}$ plot represent the corresponding unbonded layer results.

Appendix G

Additional results 2

Here we present our theoretical predictions for non-adhesive clamped beams with different slenderness ratios using the following non-dimensional parameters:

$$\hat{A} = \frac{AL}{m} = a\left(\frac{K}{\pi w R^2}\right)^{1/3}; \quad \hat{P} = \frac{\bar{P}H^3}{Lm^3} = \frac{P}{\pi w}; \quad \hat{\Delta} = \frac{\Delta L^2}{m^2} = \delta\left(\frac{K^2}{\pi^2 w^2 R}\right)^{1/3}.$$

We plot in Fig. G.1 the variation of contact area $\hat{A}$ with the variation in total load $\hat{P}$ and punch's displacement $\hat{\Delta}$. From Fig. G.1 we clearly observe that beams with higher l/h

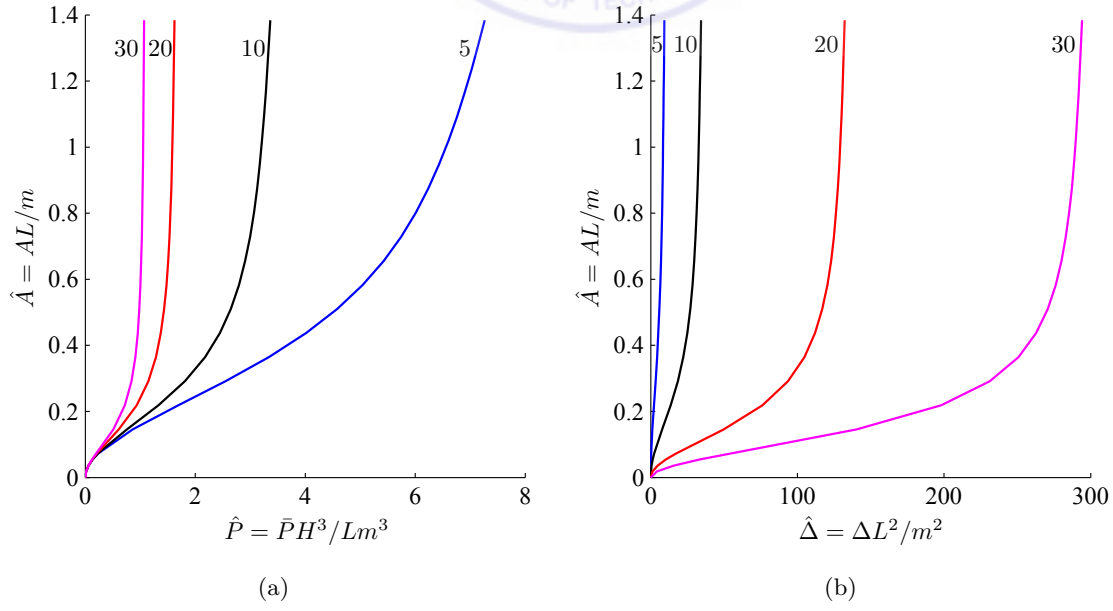

Figure G.1: Non-adhesive contact of clamped beams. Variation of contact area $\hat{A}$ with (a) total load $\hat{P}$ and (b) punch's displacement $\hat{\Delta}$ is shown. Several slenderness ratios l/h are considered and these are noted next to their associated curves.

require less load P compared to lower l/h to achieve the same contact area a. We also find that the punch's displacement $\hat{\Delta}$ is high for more slender beams.

Appendix H

Adhesive elastic half-space indentation by a rigid cylinder

We indent a thick PDMS sample with a cylindrical glass punch of radius R. During the indentation, at load P, a rectangular contact patch of length $2a$ and width $2l_s$ is observed. In our experiments, we measure P from weighing balance, $2a$ is equal to the length of the contact patch observed under the micro-scope and $2l_s$ equals the width of PDMS sample. The main aim of this experiment is to find Young's modulus E of the PDMS, and the work of adhesion w for the PDMS-glass surfaces. For adhesive interaction between the PDMS half-space with a cylindrical punch, the relationship between P and a is given by

$$\frac{3\pi}{8}\frac{a^{3/2}}{R} = \frac{1}{K}\left(\frac{P}{l_s a^{1/2}}\right) + \left(\frac{6\pi w}{K}\right)^{1/2}, \tag{H.1}$$

where $K = 4E/3(1-\nu^2)$ and Poisson's ratio $\nu = 0.5$; see Chaudhury et al. (1996). The above equation represents a straight line when we plot $3\pi a^{3/2}/8R$ versus $P/l_s a^{1/2}$. From the slope and intercept of this straight line we obtain K and w, respectively.

We note that by measuring P in 'N', and a, R and l_s in 'mm'; and employing (H.1) we get K and w in 'N/mm^2' and 'N/mm', respectively.

Appendix I

Displacement calculations for dual integral equation formulation

I.1 Approximations for vertical displacement at the bottom surface

We begin by approximating the vertical displacement at the beam's bottom surface depending on the type of end supports. In this section, we discuss suitable approximations for clamped and simply supported beams' bottom surface vertical displacement.

I.1.1 Clamped beam

We approximate the vertical displacement of the bottom surface in a beam that is clamped at the ends as

$$\vartheta_b^c(\hat{\tau}) = d_0^c + \sum_{n=1}^{M} d_n^c \cos(n\pi\hat{\tau}). \tag{I.1}$$

The above displacement filed is symmetric in $\hat{\tau}$, i.e., $\vartheta_b^c(\hat{\tau}) = \vartheta_b^c(-\hat{\tau})$. The slope conditions at the ends, i.e., $d\vartheta_b^c/d\hat{\tau} = 0$ at $\hat{\tau} = \pm 1$, are automatically satisfied. We find the unknown coefficient d_0^c in the displacement employing $\vartheta_b^c(\pm 1) = 0$, to obtain

$$d_0^c = \sum_{n=1}^{M} d_n^c (-1)^{n+1}. \tag{I.2}$$

Combining (I.1) and (I.2) yields

$$\vartheta_b^c(\hat{\tau}) = \sum_{n=1}^{M} d_n^c \left[(-1)^{n+1} + \cos(n\pi\hat{\tau})\right]. \tag{I.3}$$

Differentiating the above twice with respect to $\hat{\tau}$ provides

$$\kappa_b^c(\hat{\tau}) = -\pi^2 \sum_{n=1}^{M} d_n^c n^2 \cos(n\pi\hat{\tau}). \tag{I.4}$$

I.1.2 Simply supported beam

For a simply supported beam, we approximate the vertical displacement of the elastic layer's bottom surface in $-1 \leq \hat{\tau} \leq 1$, which should be symmetric in $\hat{\tau}$, as

$$\vartheta_b^s(\hat{\tau}) = d_0^s + \sum_{n=1}^{M} d_{2n-1}^s \sin\left\{\frac{(2n-1)\pi(\hat{\tau}+1)}{2}\right\}. \tag{I.5}$$

The above displacement field also satisfies $d^2\vartheta^s/d\hat{\tau}^2 = 0$ at $\hat{\tau} = \pm 1$, as appropriate for a simply supported beam. Satisfying $\vartheta^s(\pm 1) = 0$, makes the unknown constant $d_0^s = 0$. Hence, $\vartheta_b^s(\hat{\tau})$ becomes

$$\vartheta_b^s(\hat{\tau}) = \sum_{n=1}^{M} d_{2n-1}^s (-1)^{n-1} \cos\left\{\frac{(2n-1)\pi\hat{\tau}}{2}\right\}. \tag{I.6}$$

Differentiating the above twice we obtain the curvature $\kappa_b^s(\hat{\tau})$ in $-1 \leq \hat{\tau} \leq 1$ as

$$\kappa_b^s(\hat{\tau}) = -\sum_{n=1}^{M} d_{2n-1}^s (-1)^{n-1} \left(\frac{(2n-1)\pi}{2}\right)^2 \cos\left(\frac{(2n-1)\pi\hat{\tau}}{2}\right). \tag{I.7}$$

Calculating the slope at the ends of the beam yields

$$\left.\frac{d\vartheta_b^s(\hat{\tau})}{d\hat{\tau}}\right|_{\hat{\tau}=1} = -\sum_{n=1}^{M} d_{2n-1}^s \frac{(2n-1)\pi}{2}. \tag{I.8}$$

Finally, finding the displacement in $1 < \hat{\tau} < \infty$, by extending the beam along its slope at the end supports, we obtain

$$\vartheta_b^s(\hat{\tau}) = \left.\frac{d\vartheta^s(\hat{\tau})}{d\hat{\tau}}\right|_{\hat{\tau}=1} (\hat{\tau} - 1). \tag{I.9}$$

I.2 Calculating $\hat{\vartheta}_b(\hat{\omega})$ and $\hat{\kappa}_b(\hat{\omega})$

In this work, we consider the beams as linear elastic layers of infinite length. Thus, we employ mollifiers to find $\hat{\vartheta}_b(\hat{\omega})$ and $\hat{\kappa}_b(\hat{\omega})$. Therefore, we write

$$\hat{\vartheta}_b(\hat{\omega}) = \int_{-\infty}^{\infty} \vartheta_b(\hat{\tau})\, W(\hat{\tau}) \cos\hat{\omega}\hat{\tau}\, d\hat{\tau} \tag{I.10}$$

and

$$\hat{\kappa}_b(\hat{\omega}) = \int_{-\infty}^{\infty} \frac{d^2}{d\hat{\tau}^2}\left[\vartheta_b(\hat{\tau})\, W(\hat{\tau})\right] \cos\hat{\omega}\hat{\tau}\, d\hat{\tau}, \tag{I.11}$$

where the mollifier (Muthukumar, 2016)

$$W(\hat{\tau}) = \begin{cases} 1 & \text{for } |\hat{\tau}| \le \left|\hat{l}_1\right|, \\ w_2(\hat{\tau}) & \text{for } \left|\hat{l}_1\right| < |\hat{\tau}| < \left|\hat{l}_2\right| \\ 0 & \text{for } |\hat{\tau}| \ge \left|\hat{l}_2\right|, \end{cases} \tag{I.12a}$$

and

$$w_2(\hat{\tau}) = \frac{\exp\left\{-1/\left(\hat{l}_2 - \hat{\tau}\right)^2\right\}}{\exp\left\{-1/\left(\hat{l}_2 - \hat{\tau}\right)^2\right\} + \exp\left\{-1/\left(\hat{\tau} - \hat{l}_1\right)^2\right\}}, \tag{I.12b}$$

with $\hat{l}_1$ and $\hat{l}_2$ locating portions of the beam that are far away from the ends with $\hat{l}_2 > \hat{l}_1 \gg> 1$. The mollifier $W(\hat{\tau})$ is infinitely differentiable, and alters the displacement far from the beam's ends and makes it integrable.

I.2.1 Clamped beam

For a clamped beam, finding $\hat{\vartheta}_b^c(\hat{\omega})$ and $\hat{\kappa}_b^c(\hat{\omega})$, we obtain

$$\hat{\vartheta}_b^c(\hat{\omega}) = \sum_{n=1}^{M} d_n^c \hat{\beta}_n^c(\hat{\omega}) \quad \text{and} \quad \hat{\kappa}_b^c(\hat{\omega}) = \sum_{n=1}^{M} d_n^c \hat{\kappa}_n^c(\hat{\omega}), \tag{I.13}$$

where

$$\hat{\beta}_n^c(\hat{\omega}) = \frac{2(-1)^{n+1}\sin\hat{\omega}}{\hat{\omega}} + \frac{2\hat{\omega}(-1)^{n+1}\sin\hat{\omega}}{n^2\pi^2 - \hat{\omega}^2} \quad \text{and} \quad \hat{\kappa}_n^c(\hat{\omega}) = -n^2\pi^2 \frac{2\hat{\omega}(-1)^{n+1}\sin\hat{\omega}}{n^2\pi^2 - \hat{\omega}^2}.$$

I.2.2 Simply supported beam

Evaluating $\hat{\vartheta}_b^s(\hat{\omega})$ and $\hat{\kappa}_b^s(\hat{\omega})$ for a simply supported beam yields

$$\hat{\vartheta}_b^s(\hat{\omega}) = \sum_{n=1}^{M} \tilde{d}_n^s \, \hat{\beta}_n^s(\hat{\omega}) \quad \text{and} \quad \hat{\kappa}_b^s(\hat{\omega}) = \sum_{n=1}^{M} \tilde{d}_n^s \hat{\kappa}_n^s(\hat{\omega}), \tag{I.14}$$

where $\tilde{d}_n^s = d_{2n-1}^s$,

$$\hat{\beta}_n^s(\hat{\omega}) = \int_{-1}^{1} (-1)^{n-1} \cos\left(\frac{(2n-1)\pi\hat{\tau}}{2}\right) \cos\hat{\omega}\hat{\tau}\, d\hat{\tau} - (2n-1)\pi \int_{1}^{\hat{l}_2} (\hat{\tau}-1)\, W(\hat{\tau}) \cos\hat{\omega}\hat{\tau}\, d\hat{\tau}$$

and $$\hat{\kappa}_n^s(\hat{\omega}) = -\left(\frac{(2n-1)\pi}{2}\right)^2 \int_{-1}^{1} (-1)^{n-1} \cos\left(\frac{(2n-1)\pi\hat{\tau}}{2}\right) \cos\hat{\omega}\hat{\tau}\, d\hat{\tau}$$

$$- 2(2n-1)\pi \int_{\hat{l}_1}^{\hat{l}_2} \frac{dw_2(\hat{\tau})}{d\hat{\tau}} \cos\hat{\omega}\hat{\tau}\, d\hat{\tau} - (2n-1)\pi \int_{\hat{l}_1}^{\hat{l}_2} (\hat{\tau}-1) \frac{d^2 w_2(\hat{\tau})}{d\hat{\tau}^2} \cos\hat{\omega}\hat{\tau}\, d\hat{\tau}.$$

Finally, employing (I.13) and (I.14), we may write $\hat{\vartheta}_b(\hat{\omega})$ and $\hat{\kappa}_b(\hat{\omega})$, respectively, as

$$\hat{\vartheta}_b(\hat{\omega}) = \sum_{n=1}^{M} d_n \hat{\beta}_n(\hat{\omega}) \quad \text{and} \quad \bar{\kappa}_b(\hat{\omega}) = \sum_{n=1}^{M} d_n \hat{\kappa}_n(\hat{\omega}). \tag{I.15}$$

Bibliography

ABAQUS, 2011. *ABAQUS Documentation: version 6.11.*, Dassault Systèmes, Providence, RI, USA.

Alexandrov, A. M. and Pozharskii, D. A., 2001. *Three-dimensional contact problems*, Kluwer Academic Publishers, Dordrecht, The Netherlands.

Arul, E. P. and Ghatak, A., 2008. 'Bioinspired design of a hierarchically structured adhesive', *Langmuir* **25**(1), 611–617.

Atkinson, E. K., 1997. *The Numeical solution of Integral equations of the Second Kind*, Cambridge U. Press, Cambridge, UK.

Baney, J. M. and Hui, C. Y., 1997. 'A cohesive zone model for the adhesion of cylinders', *J. Adhesion Sci. Technol.* **11**(3), 393–406.

Barthel, E. and Perriot, A., 2007. 'Adhesive contact to a coated elastic substrate', *J. Phys. D: Appl. Phys.* **40**(4), 1059–1067.

Chatterjee, A., 2002. 'Lecture notes: An elementary continuation technique', `http://home.iitk.ac.in/~anindya/continuation.pdf`.

Chaudhury, M. K., Weaver, T., Hui, C. Y. and Kramer, E. J., 1996. 'Adhesive contact of cylindrical lens and a flat sheet', *J. Appl. Phys.* **80**(1), 30–37.

Crandall, S. H., Dahl, N. C. and Lardne, T. J., 2008. *Mechanics of Solids*, Tata McGraw-Hill Education Pvt. Ltd., New Delhi, India.

Dalmeya, R., Sharma, I., Upadhyay, C. and Anand, A., 2012. 'Contact of a rigid cylindrical punch with an adhesive elastic layer', *J. Adhes.* **88**(1), 1–31.

Derjaguin, B. V., 1934. 'Untersuchungen über die reibung und adhäsion, iv', *Koll. Z.* **69**(N2), 155–164.

Derjaguin, B. V., Muller, V. M. and Toporov, Y. P., 1975. 'Effect of contact deformations on the adhesion of particles', *J. Colloid Interface Sci.* **53**(2), 314–326.

Galin, L. A. and Gladwell, G. M. L., 2008. *Contact Problems: The legacy of L.A. Galin*, Springer, Netherlands.

Gladwell, G. M. L., 1980. *Contact Problems in the Classical Theory of Elasticity*, Sijthoff & Noordhoff Publishers, Alphen aan den Rijn, The Netherlands.

Goryacheva, I. G., 1998. *Contact Mechanics in Tribology*, Springer, Netherlands.

Hertz, H., 1881. 'On the contact of elastic solids', *J. Reine Angew. Math.* **92**, 156–171.

Hiller, U. J., 1976. 'Comparative studies on the functional morphology of two gekkonid lizards', *Bombay Nat. Hist. Soc.* **73**, 278 – 282.

Hills, D. A., Nowell, D. and Sackfield, A., 1993. *Mechanics of Elastic Contacts*, Butterworth-Heinemann, Oxford, UK.

Hu, D. and Adams, G. G., 2016. 'Adhesion of a micro-/nano-beam/plate to a sinusoidal/grooved surface', *Int. J. Solids Struct.* **99**, 40–47.

Johnson, K. L., 1958. 'A note on the adhesion of elastic solids', *Br. J. Appl. Phys.* **9**(5), 199.

Johnson, K. L., 1985. *Contact Mechanics*, Cambridge U. Press, Cambridge, UK.

Johnson, K. L., Kendall, K. and Roberts, A. D., 1971. 'Surface energy and the contact of elastic solids', *Proc. R. Soc. Lond. A* **324**(1558), 301–313.

Johnston, I. D., McCluskey, D. K., Tan, C. K. L. and Tracey, M. C., 2014. 'Mechanical characterization of bulk Sylgard 184 for microfluidics and microengineering', *J. Micromech. Microeng.* **24**(3), 035017.

Kanninen, M. F. and Popelar, C. L., 1985. *Advanced Fracture Mechanics*, Oxford U. Press, New York, USA.

Keer, L. M. and Miller, G. R., 1983. 'Smooth indentation of finite layer', *J. Eng. Mech.* **109**(3), 706–717.

Keer, L. M. and Schonberg, W. P., 1986. 'Smooth indentation of an isotropic cantilever beam', *Int. J. Solids Struct.* **22**(1), 87–106.

Keer, L. M. and Silva, M. A. G., 1970. 'Bending of a cantilever brought gradually into contact with a cylindrical supporting surface', *Int. J. Mech. Sci.* **12**(9), 751–760.

Kendall, K., 1971. 'The adhesion and surface energy of elastic solids', *J. Phys. D: Appl. Phys.* **4**(8), 1186.

Kim, J. H., Ahn, Y. J., Jang, Y. H. and Barber, J. R., 2014. 'Contact problems involving beams', *Int. J. Solids Struct.* **51**(25–26), 4435 – 4439.

Laprade, E. J., Long, R., Pham, J. T., Lawrence, J., Emrick, T., Crosby, A. J., Hui, C.-Y. and Shull, K. R., 2013. 'Large deformation and adhesive contact studies of axisymmetric membranes', *Langmuir* **29**(5), 1407–1419.

Long, R., Shull, K. R. and Hui, C.-Y., 2010. 'Large deformation adhesive contact mechanics of circular membranes with a flat rigid substrate', *J. Mech. Phys. Solids.* **58**(9), 1225–1242.

Lowengrub, M. and Sneddon, I. N., 1965. 'The distribution of stress in the vicinity of an external crack in an infinite elastic solid', *Int. J. Eng. Sci.* **3**(4), 451–460.

Mason, J. C. and Handscomb, D. C., 2003. *Chebyshev Polynomials*, Chapman & Hall/CRC, Boca Raton, Florida, USA.

Maugis, D., 1992. 'Adhesion of spheres: the JKR-DMT transition using a Dugdale model', *J. Colloid Interface Sci.* **150**(1), 243–269.

Maugis, D., 2000. *Contact, Adhesion and Rupture of Elastic Solids*, Springer-Verlag, Berlin, Germany.

Muller, V. M., Derjaguin, B. V. and Toporov, Y. P., 1983. 'On two methods of calculation of the force of sticking of an elastic sphere to a rigid plane', *Colloids Surf.* **7**(3), 251–259.

Muthukumar, T., 2016. 'Lecture notes: Sobolev spaces and applications', `http://home.iitk.ac.in/~tmk/courses/mth656/main.pdf`.

Pashley, M. D., 1984. 'Further consideration of the dmt model for elastic contact', *Colloids Surf.* **12**, 69–77.

Polyanin, A. D. and Manzhirov, A. V., 2008. *Handbook of Integral Equations: Second Edition*, Chapman & Hall/CRC, Boca Raton, Florida, USA.

Press, W. H., Teukolsky, S. A., Vetterling, W. T. and Flannery, B. P., 1992. *Numerical Recipes in C: The Art of Scientific Computing*, Cambridge U. Press India Pvt. Ltd., New Delhi, India.

Rice, J. R., 1968. 'A path independent integral and the approximate analysis of strain concentration by notches and cracks', *J. Appl. Mech.* **35**(2), 379–386.

Sadd, M. H., 2005. *Elasticity: Theory, Applications, and Numerics*, Elsevier India, New Delhi, India.

Sankar, B. V. and Sun, C. T., 1983. 'Indentation of a beam by a rigid cylinder', *Int. J. Solids Struct.* **19**(4), 293 – 303.

Sekiguchi, Y., Hemthavy, P., Saito, S. and Takahashi, K., 2012. 'Adhesion between side surface of an elastic beam and flat surface of a rigid body', *J. Adhesion Sci. Technol.* **26**(23), 2615–2626.

Sneddon, I. N., 1965. 'The relation between load and penetration in the axisymmetric Boussinesq problem for a punch of arbitrary profile', *Int. J. Eng. Sci.* **3**(1), 47–57.

Sneddon, I. N., 1995. *Fourier Transforms*, Dover Publications, New York, USA.

Srivastava, A. and Hui, C.-Y., 2013. 'Large deformation contact mechanics of a pressurized long rectangular membrane. ii. adhesive contact', **469**(2160), 20130425.

Sun, C. T. and Sankar, B. V., 1985. 'Smooth indentation of an initially stressed orthotropic beam', *Int. J. Solids Struct.* **21**(2), 161–176.

Tabor, D., 1977. 'Surface forces and surface interactions', *J. Colloid Interface Sci.* **58**(1), 2–13.

Timoshenko, S. P. and Goodier, J. N., 1970. *Theory of Elasticity*, McGraw-Hill, Singapore.

Todhunter, I. and Pearson, K., 1893. *A History of the Theory of Elasticity and of the Strength of Materials*, Vol. 2, Cambridge U. Press, Cambridge, UK.

Wagner, T. J. and Vella, D., 2012. 'The sensitivity of graphene "snap-through" to substrate geometry', *Appl. Phys. Lett.* **100**(23), 233111.

Zhang, Z. and Li, T., 2011. 'Determining graphene adhesion via substrate-regulated morphology of graphene', *J. Appl. Phys.* **110**(8), 083526.